REACTION MECHANISMS TO ENHANCE CHEMICAL COMPLEXITY IN COLD, DARK INTERSTELLAR CLOUDS

Jessica Dawn Tennis

Fort Mill, South Carolina

Bachelor of Arts, Physics, Brown University, 2017

Bachelor of Arts, Chemistry, Brown University, 2017

A Dissertation submitted to the Graduate Faculty

of the University of Virginia in Candidacy for the Degree of

Doctor of Philosophy

Department of Chemistry

University of Virginia

June 2023

Eric Herbst, Advisor

Rob T. Garrod, Chair

L. Ilse Cleeves

Kateri DuBay

Zhi-Yun Li

Reaction Mechanisms to Enhance Chemical Complexity in Cold, Dark Interstellar Clouds

Jessica Dawn Tennis

(ABSTRACT)

The cold, dark, interstellar cloud TMC-1 is home to more than 148 known molecules, and possibly many more. To understand the formation and destruction of these molecules, we present detailed theoretical work combined with a vast chemical kinetic model, `Nautilus`. Along with laboratory experimental work and observational data, these methods form the toolkit for understanding the chemistry of interstellar environments. Here, three different theoretical frameworks are used to understand the chemical reaction rates of first, cosmic rays hitting interstellar dust grains; second, neutral radicals in the gas-phase; and finally, cyanides and isocyanides also in the gas-phase. Cosmic ray radiolysis chemistry is shown to significantly enhance the abundances of HC_2O and $HCOOCH_3$ by energizing their grain-surface precursors. Radiative association between the neutral radicals CH_3 and CH_3O is shown to be rapid but unable to account for the observed abundance of CH_3OCH_3 by phase-space rate calculations conserving energy and angular momentum. On the other hand, radiative association is shown to overproduce the molecules that lead to CH_3CN, CH_3NC, H_2CNC, and, to a lesser extent, H_2CCN, perhaps because its efficiency is overestimated. Together, these investigations represent our effort to understand the ways complex organic molecules may be formed and destroyed in the cold, dark interstellar medium. We discuss possible reasons for these differences in observed and modeled abundances, and provide ideas for future directions.

Acknowledgments

In a graduate career that has spanned six years, there are many people to whom thanks are due. I will specify some here, but I am grateful to everyone who has supported and influenced me, and space is too short to do justice to the depth and variety of these.

Thank you to my parents, Paul and Glenda Tennis, who have supported me through the whole of my scientific career. They dressed me in stars from three months old, and in doctoral regalia from age four, and never doubted that I could have both the regalia and the stars if I wanted them.

Thank you to my brothers, Jon and Levi Tennis, who are the cookies to the Oreo. I'm grateful for your friendship throughout childhood, illness, and every kind of good and bad time.

Thank you to the Anderson and Ohana Community Groups, the Yellow House Girls, Rachael and Fitz Green, and especially Emily and Joe Maximus: my church family in Charlottesville, who received me warmly and without question. Your example of a life outside of graduate school kept me sane, often well-fed, and focused on community life. Your counsel, friendship, and willingness to do life together make me sure I have a home to come back to, which is a blessing I do not take lightly.

Thank you to Diana Burden, Emily Kirk, Abby Cornwell, Bret Heddleston, Trish and John Owen, Jessica and Lawrence Barker, and Carly Vaness for spending their time with me, helping me move, sharing food, films, and literature, letting me ramble about *The West Wing*, and making Charlottesville as fun a place as one could hope to be.

Thank you to the brilliant and wonderful Andrew Merk, Ricky Oliver, Christine Baltazar, Matthew Pearson, and Thang Nguyen for their love and support from afar. You keep me laughing and stretched to consider new realms. Thanks also to the nearer-by Madi Memovich, Mark Bernard, Anthony Ciancone, and Xander Wang for camaraderie and whimsy as we lost at trivia and succeeded in chemistry.

Thank you to my group mates Andrew Burkhart, Ilse Cooke, Haley Scolati, Weikai Cui, and Romane Le Gal for great discussions. Some Herbst Group members deserve special thanks, first among them Chris Shingledecker, who demonstrated the power of personality and excellence for making the group a welcoming and productive environment. Thank you to Ceci Xue for her exceptional scientific talent and for sharing Swiftie excitement. Thank you to Josh Carder for deep analysis of JRR Tolkien, joviality, and being a great officemate. And of course, thank you to my office ride-or-die, Alec Paulive, for outstanding kindness, good friendship, inspiring curiosity and thoroughness, and endless crosswording.

Thank you, last and most especially, to Eric Herbst, for insight, clarity, precision in language and in understanding, astounding intuition, leadership, mirth, and unfailing generosity of spirit. “A mentor communicates an approach,” says Elise Hancock in *Ideas into Words*, a book I’m reading as I write this, ”a consistent way of Being that in turn gives rise to appropriate Doing.” The things you think and do with and without thought will remain a model for me, and I am very lucky and grateful to have witnessed them.

Contents

List of Figures

List of Tables

Chapter 1

Introduction

The stellar life cycle is responsible for the creation of everything recognizable. The Big Bang created almost entirely H and He, which make up only a small portion of matter we interact with on a daily basis. These atoms, being randomly distributed, had some areas of higher density than others, which collapsed to become galaxies and stars within those galaxies. The fusion inside stars created carbon, oxygen, and everything else necessary for human life and experience, excepting those larger atoms produced by the violent, energetic death of the stars.

Figure 1.1 shows two views of the "Pillars of Creation," from Hubble in visible light on the left and from JWST in infrared on the right. The background of the image shows evolved stars, while the foreground shows the clouds formed by previous stellar deaths and stellar outflows. That the righthand infrared image is clearer is not just a sign of technical progress, but is instead an indicator that the longer wavelength infrared light penetrates the clouds to reveal the structure of the star-forming regions in exquisite detail. By contrast, the lefthand image shows the extent of the dust in shorter-wavelength optical light and demonstrates that even what looks "empty" is in fact a unique chemical laboratory, which will in time continue the tradition of stellar collapse, evolution, and death to form new clouds.

This introduction will examine the conditions for, and some instances of, chemistry in those clouds, and our approaches to modeling that chemistry.

Figure 1.1: Left: Hubble Space Telescope image of the "Pillars of Creation" in visible light. Right: JWST's view of this star-forming region, in infrared light. Credits: SCIENCE: NASA, ESA, CSA, STScI, Hubble Heritage Project (STScI, AURA). IMAGE PROCESSING: Joseph DePasquale (STScI), Anton M. Koekemoer (STScI), Alyssa Pagan (STScI).

1.1 Cold, Dark Clouds

Just as terrestrial clouds are composed of solid and gaseous water, so clouds in the interstellar medium (ISM) are made up of gaseous atoms and molecules as well as ices, though cold and low density do not allow for clouds in the ISM to contain liquid. The ices in cold clouds are formed when water molecules begin to accumulate on bare grain mantles about one tenth of a micron in diameter, forming a new surface. As more molecules land on the grain, these first begin to be covered; we term ices below the first layer "bulk mantle" species. Though any chemical species could in principle land on the grain, the prevalence of water, CO_2, and CO and their cohesion mean that most of the surface will be composed of these, with just a few of any other given molecule at a time. Chen et al. (2022) explains the variation of the dominant ice species in the Taurus Molecular Cloud by comparison to the visual extinction, A_v,

and the ratio of the abundances of C and O.

"Cold" here refers to the kinetic temperature of the cloud, which is usually estimated to be around 10 K, though the sparsity of the gas does not allow for a sufficient collisional rate to achieve a true thermodynamic equilibrium. Therefore, every molecule has instead an excitation temperature related to the amount of energy it is itself carrying, which is determined by the particular wavelength of light emitted by the molecules in the cloud. Infrared radiation, as seen in the righthand of Figure 1.1, penetrates a cold, dark cloud and becomes both the primary source of cooling as molecules in the cloud radiate away energy, and an indicator of just how cold "cold" really is.

"Dark" refers not just to the fact that no star has yet developed from the ice and gas matter in the cloud, but to the fact that the visual extinction, A_v, is high. Visual extinction is a measurement of how much light (in magnitudes) is attenuated when the light in visual wavelengths passes through the region of interest. Even light produced outside of the cloud by some other star or galaxy may only penetrate into the first few layers of gas and dust. Figure 1.1 demonstrates that dust blocks much of the visual light, lending Hubble's lefthand image a "blurrier" foreground, whereas the infrared light is able to penetrate the dust and reach JWST to reveal the many stars and galaxies in the background of the righthand image.

1.1.1 TMC-1

This work focuses on one cold, dark cloud in particular: the Taurus Molecular Cloud (TMC-1), shown in Figure 1.2.

Figure 1.2: A four-color infrared image of TMC-1. From ESA/Herschel/NASA/JPL-Caltech CC BY-SA 3.0 IGO; Acknowledgement: R. Hurt (JPL-Caltech).

TMC-1 gets its name from its location in the patch of terrestrial sky known as Taurus, though it also stretches into neighboring Auriga. "Molecular" is a well-earned title, too, as at least 148 molecules have been detected there, beginning with the detections of HC_nN chains (Morris et al., 1976; Churchwell et al., 1978), and now even including aromatic molecules benzonitrile and indene (McGuire et al., 2018; Burkhardt et al., 2021). "1" indicates that Taurus contains multiple structures developing into stars and even more than one molecular cloud. Working at the National Radio Astronomical Observatory in 1966, Carl Heiles identified three distinct clouds in this region (Heiles, 1967). Another of these, TMC-2, was first examined in detail by Little et al.

(1978) and is about 9^m west and 1°18' south of TMC-1.

Within TMC-1, there are four velocity components, at 5.6, 5.8, 5.9, and 6.0 km/s from the local standard of rest (Dobashi et al., 2018; Loomis et al., 2021). The velocity components appear to overlap along the line of sight. Each of these is of a different size, and could be of a different temperature and chemical complexity, but all four are added together to give the total of the number and abundance of observed species in TMC-1.

Some of the characteristics of TMC-1 are best determined by observations combined with chemical modeling. Following Hincelin et al. (2011) and Loomis et al. (2021) the age of TMC-1 is taken to be $\sim 5 \times 10^5$ years.

1.2 `Nautilus`

The timescales of stellar birth and evolution do not lend themselves to observation directly, except for some specific stochastic processes (Cleeves et al., 2017). To study the chemistry happening over millions of years during these processes, therefore, we need a time efficient and computationally efficient mechanism, and we turn to the rate-equation based model.

Our model, `Nautilus`, was introduced by Ruaud et al. (2016) and has been updated collaboratively since then at the online database KIDA (Wakelam et al. (2012); https://kida.astrochem-tools.org). It is a three-phase rate equation model, which includes the rates of 7981 gas-phase reactions and 8034 grain reactions involving 549 gas-phase and 1017 grain-surface and bulk mantle species to compute abundances of species over time, beginning with the elemental abundances in Table 1.1.

Table 1.1: Initial elemental abundances with respect to the total number of hydrogen atoms for the models of TMC-1 (Hincelin et al., 2011).

Species	**Fractional Abundance**
H_2	0.499
H	$5.00\text{x}10^{-5}$
He	$9.00\text{x}10^{-2}$
C	$1.70\text{x}10^{-4}$
N	$6.20\text{x}10^{-5}$
O	$1.55\text{x}10^{-4}$
S	$8.00\text{x}10^{-8}$
Na	$2.00\text{x}10^{-9}$
Mg	$7.00\text{x}10^{-9}$
Si	$8.00\text{x}10^{-9}$
P	$2.00\text{x}10^{-10}$
Cl	$1.00\text{x}10^{-9}$
Fe	$3.00\text{x}10^{-9}$

The abundances in Table 1.1 refer to the abundances at an arbitrary zero mark of time for the cold, dark cloud, when every gas-phase species is assumed to be atomic except for hydrogen, which is assumed to be mostly in H_2. `Nautilus` then uses a series of rate equations and parameters such as those in Table 1.2 to determine the abundances of chemical species both atomic and molecular moving forward in time stepwise from the zero mark to 10^8 years, an age beyond which most cold, dark clouds have evolved stars.

The system of rate equations is set up as follows. A species, w, will be produced by

Table 1.2: Parameters for models of TMC-1.

Parameter	**Value**
Temperature, T	10 K
Visual Extinction, A_v	10
Cosmic Ray Ionization Rate, ζ	$1.3\text{x}10^{-17}$ s^{-1}
Gas Density, n_H	10^4 particles per cm^3
Dust Density, n_d	10^{-8} particles per cm^3
Site Density, N_{site}	10^{15} sites per cm^2

some chemical reactions and destroyed by others, and therefore the change over time in the abundance of w is given by the sum of all of these reactions, which can be written:

$$\frac{dn(w)}{dt} = \sum_x \sum_y k_{xy} n(x) n(y) - n(w) \sum_z k_{wz} n(z), \tag{1.1}$$

where each $n(x)$, $n(y)$, and $n(z)$ are the number densities of x, y, and z, respectively. Species w is produced by the reaction of x and y, which occurs with rate coefficient k_{xy}. Species w is destroyed by its reaction with z, which occurs with rate coefficient k_{wz}.

As indicated by Eq. 1.1, the number densities and rate coefficients of reaction are both essential to understanding the chemical diversity of the ISM at any given moment. As such, much of this work will focus on these rate coefficients.

Every chemical species in the rate-equation based model gets one differential equation such as Eq. 1.1, such that the total number of differential equations is the same as the number of species in the network. Gas-phase species, grain-surface species and bulk-mantle species are all considered separately. Although CH_3OH is the same in some sense whether it is in the gas or on the surface of a grain, it will react differently in these distinct phases and therefore it requires a separate rate equation.[1] All the rate equations are coupled by the fact that the rate of change of one species (dw/dt in Eq. 1.1) depends on the abundances of other species (x, y, and z in Eq. 1.1).

With the initial abundances in Table 1.1 and the rate equations of every species as in Eq. 1.1, `Nautilus` takes one step forward in time by calculating the abundances of all species after the first timestep. The resulting abundances after timestep one are used

[1] Other methods to handle this complexity have also also been developed, as in Garrod et al. (2008).

as inputs for timestep two, and so on until the model run is complete. Our models progress such that each step forward is spaced evenly throughout the log timescale. Consider a typical model, with 3000 timesteps ending at 10^7 years. In this case, while step one moves forward about 44 hours, the last step moves 5400 years because of the logarithmic spacing.

A major advantage of rate-equation models is their speed. The modern computer solves this coupled system of equations quickly with linear algebra. Our models can be changed slightly and rerun on the order of one minute, allowing for many models and comparison of the effects of one change on the resulting abundances of chemical species over time.

A major drawback of rate-equation models is their reliance on time averages. As explained above, the model relies on rate coefficients, under the assumption that all processes which affect the abundance of any given chemical species are essentially continuous processes moving at particular speeds. In reality, almost all important processes are stochastic: these processes happen discretely, but may be approximated as happening continuously slowly (as in a stochastic process only likely to happen once in a long time) or continuously quickly (as in a stochastic process likely to happen repeatedly in a short time). The appropriateness of this approximation depends on the type of process under consideration.

1.2.1 Monte Carlo Models

Cosmic rays are highly energetic, positively charged particles which dramatically change the chemistry and physics of a dust grain when the cosmic ray and grain collide. A cosmic ray hitting a dust grain is a perfect example of a process that is

best understood as stochastic. We use Monte Carlo models as a tool to determine the best approximation of a rate coefficient for chemical reactions based on stochastic processes, in order to include them in `Nautilus`. This example is covered in detail in Chapter 2.

Monte Carlo models use random numbers to determine the progress of some phenomenon, often in astrochemistry tracking individual molecules or atoms across a grain surface (e.g., Chang & Herbst, 2014; Willis & Garrod, 2017). One atom or molecule moves at a time, which can result in computational difficulties as some species move much faster than others. Light hydrogen atoms are such a species that challenge astrochemical Monte Carlo models. As species diffuse across grains, they may come to inhabit the same site as other species, allowing the possibility of reaction. Since each molecule or atom is tracked individually and exact results are dependent on each other species, parallelization is not often possible. As a result, Monte Carlo models give very good pictures of exact chemistry very slowly.

1.3 Relevant Chemistry

There are two phases of matter involved in chemical reactions in the ISM: gas-phase species and solid-phase species, the latter of which may be further divided into those in the mantle and those on the surface of the dust grains. Atoms and molecules from the gas land on the surfaces of the grains in clouds. As a general principle, complex organic molecules (COMs; carbon-based molecules with six or more atoms in the interstellar medium) are formed when atoms land on the surfaces of grains and react with one another (Garrod et al., 2008). A variety of nonthermal desorption mechanisms can then lift these species off of the grain, and when the cloud begins to

condense and warm up, thermal desorption becomes important.

1.3.1 Radiative Association

One essential gas-phase reaction type is radiative association,

$$A + B \rightleftharpoons \{AB^*\} \rightarrow AB + h\nu \tag{1.2}$$

whereby two species, A and B, often one neutral and one ionic molecule, collide and the excess energy of this collision is radiated away from the collision complex AB^* by the emission of a photon.

Radiative association is an effective way to build larger molecular species up from atoms and smaller molecules, making it a crucial process in the ISM. The examples of C^+ and CH_3^+ reacting with H_2 illustrate why. In both cases, the bimolecular exit channels are endothermic and therefore do not play a role in cold, interstellar environments, but larger ions can be built with radiative association reactions (Herbst et al., 1977; Gerlich & Horning, 1992).

To calculate the rate coefficient $k_{\rm ra}$ for a radiative association reaction as in Eq. 1.2, we use the steady state approximation. The resulting formulation is:

$$k_{\rm ra} = \frac{k_1 k_{\rm r}}{k_{\rm r} + k_2 + k_{-1} + k_{\rm c}[M]} \tag{1.3}$$

where k_1 is the rate of formation for the collision complex AB^*, $k_{\rm r}$ is the rate of stabilizing emission from the collision complex, k_2 is the rate of reaction to form some products C and D distinct from the reactants, k_{-1} is the rate of redissociation into the reactants A and B, and $k_{\rm c}$ is the rate of collisional stabilization of the collision

complex by some other chemical species M. In the sparse ISM, k_c is assumed to be vanishingly small, and k_2 is only nonzero if the reaction is exothermic. Each of these rate coefficients is examined in more detail in Chapter 3.

1.3.2 Dissociative Recombination

Often a partner to radiative association, dissociative recombination proceeds as an electron colliding with a cation to form at least two neutral fragments:

$$AB^+ + e^- \rightarrow A + B. \tag{1.4}$$

Dissociative recombination is often an important precursor to the formation of neutral molecules, such as CH_3CN and CH_3NC explored in Chapter 4. It is also an important destruction route for ions, and for molecules with large proton affinities which can be protonated by other species like NH_4^+ and then destroyed by reaction with an electron (Garrod & Herbst, 2023).

The rate coefficients for dissociative recombination reactions have often been studied in laboratory experiments. For those reactions which do not yet have measured experimental results, estimates can be made based on similar precursor cations, as the range of dissociative recombination reaction rate coefficients tends only to cover the range of $\sim 10^{-7}$ - 10^{-6} cm^3s^{-1}. Less predictable, however, is the temperature dependence of these rate coefficients. While theoretical treatments predict a dependence of $T^{-0.5}$, experimental work has shown that the temperature dependence may in fact be much stronger, such that reactions at colder temperatures proceed much more quickly than theoretical estimates predict. For example, Paul et al. (2022) find dissociative recombination of CH^+ proceeds at a rate that is a factor of six faster than

prior theoretical estimates because electronic transitions, rather than rovibrational, characterize the reaction.

A challenge associated with dissociative recombination is to determine the branching ratios of the product channels. Predicting these with quantum chemistry is exceptionally difficult because of the highly excited states and the complicated potential energy surfaces, and laboratory data on branching fractions do not yet exist for all the ions one might wish to study in the ISM.

1.3.3 Radiolysis

Unlike radiative association and dissociative recombination, radiolysis chemistry explores the effects of an external energy source: cosmic rays.

Cosmic rays, as mentioned above (§1.2.1), are highly energetic cations - that is, particles, and not true "rays." The concept of this somewhat misleading term first came from the German "*kosmiche Strahlung*," introduced by Gockel & Wulf (1908), whose electrometer (Figure 1.3a) measurements found for the first time that the effects of cosmic rays were not changed by measurement at different altitudes. That particles rather than photons comprise cosmic rays followed measurements of the latitude variation of their intensity and the realization that the Earth's magnetic field was deflecting away the lower energy particles in the equatorial regions (Compton & Turner, 1937, see Figure 1.3b). However, the die was cast, and the term "cosmic rays" persists. An intriguing and more complete history may be found in Walter & Wolfendale (2012).

The cations that make up cosmic rays are ∼90% protons, ∼9% Helium nuclei, and ∼1% heavier nuclei (Cummings et al., 2016). They are thought to be produced in

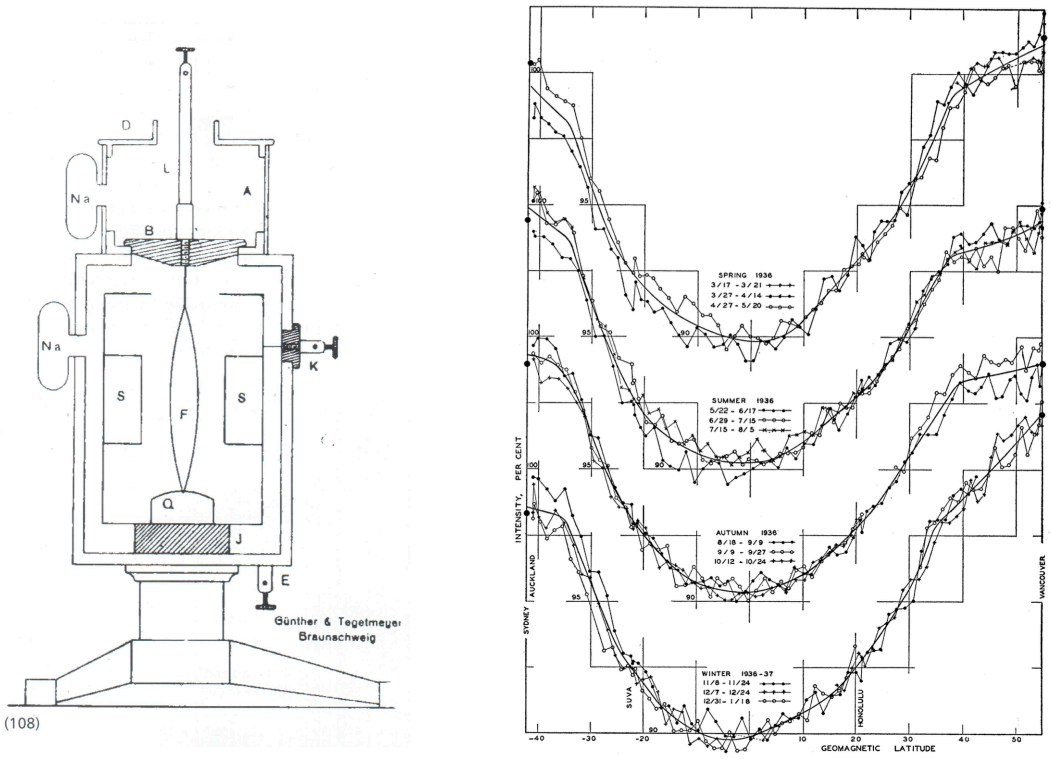

(a) (b)

Figure 1.3: (a) Schematic of the electrometer invented by Wulf in 1908 and brought to the Alps and then, in 1909, on a series of balloon trips to measure radiation. This image was produced by Günther & Tegetmeyer in Braunschweig around 1908 and taken from Walter & Wolfendale (2012). (b) The magnetic latitude effect measured by Compton and Turner on a series of sea voyages (Compton & Turner, 1937). Abscissa, latitude from -40°to 50°; ordinate, intensity of ionization in percentages shifted to separate seasons.

supernovae, which provide each nucleus with energy in the range $\sim$1 – 10^{11} GeV. Less energetic cosmic rays (<30 GeV) are unable to reach detectors in the inner solar system because of solar wind, and this part of the energy distribution is not understood as well as the rest. Estimates of the lower limit of cosmic ray energies range as low as 1 MeV (Ip & Axford, 1985).

The chemical impacts of such an energetic particle colliding with a gas-phase atom or a dust grain are varied and immense, as will be explored in more detail in Chapter 2.

The incident ion itself, the "primary," transfers energy nucleus-to-nucleus, which can heat up or break the "target" it hits. Charge interactions between the primary and the target can excite the target electrons, or ionize the target entirely. Ionizing the target creates "secondary electrons," which are also energetic and cause chain reactions with other species, often several layers deep into a solid dust mantle (see, e.g., Shingledecker et al., 2017).

One essential effect of cosmic rays in the gas phase of the ISM is their impact on hydrogen. The cosmic ray ionization rate, ζ, is defined as the rate of the reaction

$$\mathrm{H_2} + CR \rightsquigarrow \mathrm{H_2^+} + \mathrm{He^-} \tag{1.5a}$$

$$\rightsquigarrow \mathrm{H} + 2\mathrm{H^+} + \mathrm{e^-}. \tag{1.5b}$$

This reaction has been shown to have physical and chemical effects such as heating (Spitzer & Tomasko, 1968), and production of CO (Herbst & Klemperer, 1973). Estimates of the value of ζ vary, but the rate in TMC-1 is estimated to be $1.3\mathrm{x}10^{-17}$ $\mathrm{s^{-1}}$ (e.g., Caselli et al., 1998) which is also taken to be standard for interstellar environments.

1.4 Scope of Thesis

This thesis explores the effects of a variety of chemical processes to examine whether they can enhance chemical complexity in the cold, dark ISM as typified by TMC-1.

Most complex organic molecules are formed on the surfaces of dust grains, and then lifted into the gas when the condensing cloud begins to heat up. However, many COMs, like $\mathrm{CH_3OCH_3}$ explored in Chapter 3, are observed at higher abundances in

the gas phase than thermal desorption the cold temperatures can explain. These molecules must either be lifted off of the grain surface in nonthermal ways like radiolysis (e.g., Paulive et al., 2021) and sputtering (e.g., Paulive et al., 2022), or produced in the gas phase initially. Other molecules, however, are overproduced in the chemical kinetic models of the ISM, as is the case for CH_3CN and CH_3NC discussed in Chapter 4.

Using a variety of theories and `Nautilus` models, we attempt to capture the observed abundances of several molecules including HC_2O, $HCOOCH_3$, CH_3OCH_3, CH_3CN, CH_3NC, and H_2CCN.

The first of these approaches is to examine how the energy of a cosmic ray can increase the rates of reaction on surfaces of dust grains, which we undertake in Chapter 2. We find that the energy supplied to the grain-surface molecules is very effective in increasing the gas-phase abundances of HC_2O and $HCOOCH_3$ in line with observed abundances.

Next, we examine in Chapter 3 the possibility of neutral radicals in the gas combining through radiative association to build larger, more complex molecules. We find that the reaction between CH_3 and CH_3O is rapid, but these reactant radicals are not sufficiently abundant to enhance the population of the predicted product CH_3OCH_3.

In Chapter 4 we discuss the modeling of CH_3CN and CH_3NC and detail our efforts to correct their overproduction through examination of their production and destruction routes. The modeling of H_2CCN captures its observed abundance. We also present the observation of CH_3CN, H_2CCN, and CH_3NC and set an upper limit on the abundance of H_2CNC.

Finally, we come to our conclusions and discuss ideas for future research in Chapter 5.

Chapter 2

On Cosmic-Ray-driven Grain Chemistry in Cold Core Models

In this paper, we present preliminary results illustrating the effect of cosmic rays on solid-phase chemistry in models of both TMC-1 and several sources with physical conditions identical to TMC-1 except for hypothetically enhanced ionization rates. Using a recent theory for the addition of cosmic-ray-induced reactions to astrochemical models, we calculated the radiochemical yields, called G values, for the primary dust grain ice-mantle constituents. We show that the inclusion of this nonthermal chemistry can lead to the formation of complex organic molecules from simpler ice-mantle constituents, even under cold core conditions. In addition to enriching ice mantles, we find that these new radiation-chemical processes can lead to increased gas-phase abundances as well, particularly for HOCO, NO_2, HC_2O, methyl formate ($HCOOCH_3$), and ethanol (CH_3CH_2OH). These model results imply that HOCO—and perhaps NO_2—might be observable in TMC-1. Future detections of either of these two species in cold interstellar environments could provide strong support for the importance of cosmic-ray-driven radiation chemistry. The increased gas-phase abundance of methyl formate can be compared with abundances achieved through other formation mechanisms such as pure gas-phase chemistry and surface reactions.[1]

[1]Originally published as part of Shingledecker et al. (2018). Models by J. D. Tennis and C. N. Shingledecker. Figures by C. N. Shingledecker.

2.1 Introduction

Cosmic rays are a form of high-energy (MeV - TeV) ionizing radiation composed mostly of protons thought to form both in supernovae and galactic nuclei (Blasi, 2013; Baade & Zwicky, 1934; Lemaitre & Vallarta, 1933). It has long been speculated that these energetic particles can have significant physicochemical effects on the interstellar medium (ISM) as a result of collisional energy transfer to the matter in a region. For example, in Herbst & Klemperer (1973), cosmic rays were shown to be the drivers of cold core chemistry via

$$H_2 \rightsquigarrow H_2^+ + e^- \tag{2.1}$$

followed by

$$H_2^+ + H_2 \rightarrow H_3^+ + H \tag{2.2}$$

where the curly arrow implies bombardment by an energetic particle. The ion-molecule reactions initiated by H_3^+ are of central importance in the subsequent formation of polyatomic species. In addition, cosmic rays are thought to play an important role both in source heating (Goldsmith & Langer, 1978; Ao et al., 2013) and in generating internal UV photons in cold cores through the Lyman and Werner band excitation of H_2 (Prasad & Tarafdar, 1983).

The Galactic value of the cosmic ray ionization rate, ζ, cannot be directly measured from Earth due to the effects of the Solar wind (Parker, 1958). It is thought that the most common ionization rate in the ISM is $\zeta \approx 10^{-15}$ s^{-1} everywhere but in dense regions (Grenier et al., 2015), where interactions between the dense cloud and

the charged particles that comprise cosmic rays result in a reduced ionization rate of $\sim 10^{-17}$ s^{-1} (Rimmer et al., 2012). However, even in dense regions, local effects can result in substantially higher fluxes of ionizing radiation leading to ionization rates in the range $\zeta \approx 10^{-15} - 10^{-14}$ s^{-1}. Such rates arise in Sgr A* (Yusef-Zadeh et al., 2013a,b; Ao et al., 2013), and in sources like W51C, which are near supernova remnants (Ceccarelli et al., 2011; Shingledecker et al., 2016).

Collisions between cosmic rays and dust grains are also important in the ISM. For instance, Ivlev et al. (2015b) note that cosmic rays affect the net charge on dust particles, which has an influence on grain growth. Cosmic ray collisions have also been implicated in impulsive grain heating (Hasegawa & Herbst, 1993; Ivlev et al., 2015a), which can stimulate both diffusive chemistry and desorption. Despite this, the direct chemical effects resulting from cosmic ray bombardment of dust grain ice mantles are not currently considered in astrochemical models. Previous experimental work has shown that the bombardment of low-temperature ices by ionizing radiation can trigger a rich chemistry (Hudson & Moore, 2001; Rothard et al., 2017; Abplanalp et al., 2016) - including the formation of complex organic molecules such as amino acids (Hudson et al., 2008; Lafosse et al., 2006; Holtom et al., 2005).

Following Bohr (1913), the energy lost by an energetic particle per distance travelled - called the stopping power - can be approximated by the sum of two types of energy loss, as seen in the following equation:

$$\frac{dE}{dx} = n(S_\mathrm{n} + S_\mathrm{e}) \tag{2.3}$$

where n is the density of the target material, while S_n and S_e are so-called stopping cross sections (Johnson, 1990; Ziegler & Biersack, 1985) - also known as energy loss

functions, in units of area × energy (Peterson & Green, 1968). Here, S_n characterizes the elastic energy collisionally transferred to nuclei in a material, while S_e characterizes the energy transferred to electrons in inelastic collisions (Bohr, 1913; Johnson, 1990; Spinks & Woods, 1990). Inelastic events, in turn, are typically approximated as consisting of collisions that cause either the ionization or electronic excitation of target species. The ionization of species in a material results in the formation of so-called "secondary electrons" (Spinks & Woods, 1990). Around 10^4 secondary electrons can be produced per MeV transferred to a material, and they play a critical role in propagating physicochemical changes initiated by primary ions (Gerakines et al., 2001; Mason et al., 2014; Spinks & Woods, 1990).

In Abplanalp et al. (2016), we made the first attempt - to the best of our knowledge - to incorporate experimentally determined chemical reactions resulting from radiation processes into an astrochemical model. Based on insights gained both from that work, and from radiation chemistry based on a subsequent detailed microscopic Monte Carlo model (Shingledecker et al., 2017), we developed a general method described in detail in Shingledecker & Herbst (2018) targeted at the great majority of astrochemically relevant radiolysis processes which have not been studied in detail in the laboratory. The basis of this method is that a microscopic collision between a target species, A, and either a primary ion or secondary electron is assumed to have one of the following outcomes:

$$A \rightsquigarrow A^+ + e^- \tag{R1}$$

$$A \rightsquigarrow A^+ + e^- \rightarrow A^* \rightarrow bB^* + cC^* \tag{R2}$$

$$A \rightsquigarrow A^* \rightarrow bB + cC \tag{R3}$$

or

$$A \rightsquigarrow A^*. \tag{R4}$$

Here, the asterisk indicates an electronically excited species, which can be referred to as "suprathermal" (Abplanalp et al., 2016); B and C are the dissociation products; and the lowercase letters are the stoichiometric coefficients (Spinks & Woods, 1990). In this work, we will refer to molecular dissociation due to bombardment by ionizing radiation as *radiolysis* (Spinks & Woods, 1990; Johnson, 2011).

In processes (R1) and (R2), A is ionized upon collision with an energetic particle, resulting in the ion-pair $A^+ + e^-$, which can quickly undergo dissociative recombination, as shown in (R2). The relative importance of (R1) and (R2) is characterized by the electron escape probability, P_e, which we will here assume to be zero for solid-phase processes, so that (R1) is negligible. In processes (R3) and (R4), A is electronically excited after collision with an energetic particle. As with the ionizing processes, (R1) and (R2), the relative importance of (R3) and (R4) is given by P_dis, the dissociation probability, which we will here assume to be 0.5 in the absence of relevant experimental or theoretical values. Based on results from previous, more detailed Monte Carlo modeling of radiation chemistry (Shingledecker et al., 2017), we have assumed that the intermediate species A^* produced via (R2) dissociates immediately with unit probability, unlike in process (R3), due to the greater exothermicity of dissociative recombination.

The suprathermal species produced in processes (R2) and (R4) are critical when considering the effects of radiation exposure on a material, particularly in cold regions, because their energies are often sufficient to overcome reaction barriers that are inaccessible to the reactants in their ground electronic states (Spinks & Woods, 1990). Previous experimental work suggests that these electronically excited species can drive the formation of complex organic molecules, even in solids at 5 K (Abplanalp et al., 2016), where they likely either rapidly react with a neighbor or are quenched by the material (Spinks & Woods, 1990).

The overall efficiency of processes (R1)-(R4), called the radiochemical yield, is characterized by the G value (Dewhurst et al., 1952), defined as the number of molecules created or destroyed per 100 eV deposited by an incident energetic particle into some system. As described in detail in Shingledecker & Herbst (2018), the G values for processes (R1)-(R4) can be calculated using the following expressions:

$$G_{\mathrm{R1}} = P_{\mathrm{e}} \left(\frac{100\,\mathrm{eV}}{W} \right) \tag{2.4}$$

$$G_{\mathrm{R2}} = (1 - P_{\mathrm{e}}) \left(\frac{100\,\mathrm{eV}}{W} \right) \tag{2.5}$$

$$G_{\mathrm{R3}} = P_{\mathrm{dis}} \left(\frac{100\,\mathrm{eV}}{W} \right) \left(\frac{W - (E_{\mathrm{ion}} + W_{\mathrm{s}})}{W_{\mathrm{exc}}} \right) \tag{2.6}$$

and

$$G_{\mathrm{R4}} = (1 - P_{\mathrm{dis}}) \left(\frac{100\,\mathrm{eV}}{W} \right) \left(\frac{W - (E_{\mathrm{ion}} + W_{\mathrm{s}})}{W_{\mathrm{exc}}} \right) \tag{2.7}$$

where W is the mean energy per ion-pair (usually $\sim$ 30 eV) (Dalgarno & Griffing, 1958; Edgar et al., 1973), E_{ion} is the ionization energy of A, W_{exc} is the average excitation energy of A, and W_{s} is the average sub-excitation energy of the secondary electrons formed via the ionization of A (typically $\sim$ 3 eV) (Fueki & Magee, 1963; Elkomoss & Magee, 1962).

By definition, there is one ionization per ion-pair; however, the number of excitations per ionization is a function of the average excitation energy. The average number of excitations per ionization, ξ, is given by

$$\xi = \frac{W - (E_{\mathrm{ion}} + W_{\mathrm{s}})}{W_{\mathrm{exc}}} \tag{2.8}$$

and is the extra factor included in Eqs. (2.6) and (2.7). Physically, for every W eV lost per ion-pair, an amount equal to E_{ion} of that energy is used to generate the ion-pair, and some small amount W_{s} accounts for the fact that secondary electrons (a) lose energy through inelastic collisions or (b) have insufficient energy upon formation to either ionize or excite species in the material. Thus, the remaining energy per ion-pair available to cause electronic excitations is $W - (E_{\mathrm{ion}} + W_{\mathrm{s}})$, and ξ, the average number of excitations that can result from this amount of energy, is a function of the average excitation energy, W_{exc}.

These G values can, in turn, be used to estimate the first-order rate coefficients (s^{-1})

of processes R1-R4 via

$$k_{\rm R1} = G_{\rm R1}\left(\frac{S_{\rm e}}{100\ {\rm eV}}\right)\left(\phi_{\rm ST}\left[\frac{\zeta}{10^{-17}}\right]\right) \tag{2.9}$$

$$k_{\rm R2} = G_{\rm R2}\left(\frac{S_{\rm e}}{100\ {\rm eV}}\right)\left(\phi_{\rm ST}\left[\frac{\zeta}{10^{-17}}\right]\right) \tag{2.10}$$

$$k_{\rm R3} = G_{\rm R3}\left(\frac{S_{\rm e}}{100\ {\rm eV}}\right)\left(\phi_{\rm ST}\left[\frac{\zeta}{10^{-17}}\right]\right) \tag{2.11}$$

and

$$k_{\rm R4} = G_{\rm R4}\left(\frac{S_{\rm e}}{100\ {\rm eV}}\right)\left(\phi_{\rm ST}\left[\frac{\zeta}{10^{-17}}\right]\right). \tag{2.12}$$

Here, $\phi_{\rm ST}$ is the integrated Spitzer-Tomasko cosmic ray flux (8.6 particles cm^{-2} s^{-1}) (Spitzer & Tomasko, 1968), ζ is the H_2 ionization rate, and $S_{\rm e}$ is the electronic stopping cross section (Bethe, 1932; Johnson, 1990; Ziegler & Biersack, 1985). Amorphous H_2O is typically the dominant ice-mantle constituent; thus, we approximate the stopping cross section for protons in amorphous water ice with the more readily available values for liquid water, which were calculated using the `PSTAR` program[2]. An average value of $S_{\rm e} = 1.287 \times 10^{-15}$ cm^2 eV was obtained using the Spitzer-Tomasko cosmic ray flux (Spitzer & Tomasko, 1968). One can estimate the effect of going from a water ice to, for example, one comprised mainly of CO using the ratio of stopping cross

[2]https://physics.nist.gov/PhysRefData/Star/Text/PSTAR.html

sections for the two species. Using the Bethe equation for the electronic stopping cross section (Bethe, 1932) - and all else being equal - $S_e^{CO} \approx 1.4 \times S_e^{H2O}$ - which may not have a significant effect in most astrochemical models. As discussed further in §2.3, when multiplied by the density of the reactant species, Eqs. (2.9)-(2.12) refer to the time dependence of the concentration of products produced by radiolysis - driven mainly by inelastic collisions involving secondary electrons.

We here examine how radiolysis of the primary dust grain ice mantle constituents influences the chemistry of cold cores like TMC-1. The organization of the rest of this paper is as follows: in §2.2 we give details concerning the code and physical conditions used here, while §2.3 contains a description of the reactions and processes added to the network for this work. §2.4 concerns the description and discussion of our major findings, while in §2.5, we summarize our results and point to areas of future development.

2.2 Models

In this work, we focus on the chemistry of cold cores, such as TMC-1. Despite the low temperatures of these regions, their chemical complexity has been highlighted by recent detections of species such as HC_5O (McGuire et al., 2017a), HC_7O (McGuire et al., 2017a; Cordiner et al., 2017), and the aromatic molecule benzonitrile (McGuire et al., 2018). The effects of radiation chemistry should be more pronounced in these cold interstellar environments since thermal diffusion is inhibited, thus increasing the relative importance of fast solid-phase reactions involving suprathermal species.

We utilized the `NAUTILUS`-1.1 astrochemical model (Ruaud et al., 2016), in which three phases are simulated, specifically, (a) the gas-phase, (b) the ice/grain-surface,

and (c) the ice-mantle bulk. This distinction between the surface and bulk of the ice is helpful here, since it highlights an important aspect of solid-phase radiation chemistry, namely, that bombardment by ionizing radiation can greatly increase the chemical importance of the bulk ice, since this is the phase in which the majority of the physicochemical changes likely occur (Johnson, 1990; Spinks & Woods, 1990; Shingledecker et al., 2017). The degree of penetration into the ice constitutes a major difference between photochemistry and radiation chemistry (Gerakines et al., 2001; Gerakines et al., 2004). In the absence of bombardment by energetic particles, the surface is significantly more important in astrochemical models, due both to the lower diffusion barriers and direct contact with the surrounding gas. The non-thermal desorption mechanisms for surface species are (1) chemical desorption with a standard 1% efficiency (Garrod et al., 2007) (2) cosmic ray-induced desorption (Hasegawa & Herbst, 1993), and (3) photodesorption (Bertin et al., 2013).

We ran simulations of two different types of sources, the cold core TMC-1 and a group of hypothetical sources physically identical to TMC-1, other than having higher ionization rates. The latter set of simulations were run in order to identify any trends in our models arising from the included radiation chemistry. The physical conditions used here for both sets of simulations are given in Table 2.1, and all models utilized the same initial elemental abundances, listed in Table 2.2 [3].

Table 2.1: Model parameters and physical conditions used.

Parameter	**TMC-1**	**Hypothetical Sources**
$n_{\rm H}$ (cm^{-3})	10^4	10^4
$n_{\rm dust}$ (cm^{-3})	1.8×10^{-8}	1.8×10^{-8}
$T_{\rm gas}$ (K)	10	10
$T_{\rm grain}$ (K)	10	10
$A_{\rm v}$ (mag)	10	10
$N_{\rm site}$ (cm^{-2})	1.5×10^{15}	1.5×10^{15}
ζ (s^{-1})	10^{-17}	$10^{-17} - 10^{-14}$

Table 2.2: Elemental abundances used in this work.

Element	**Value**
$X(\rm H_2)$	5.00×10^{-1}
$X(\rm He)^a$	9.00×10^{-2}
$X(\rm N)^a$	2.14×10^{-5}
$X(\rm O)^b$	1.70×10^{-4}
$X(\rm C^+)^c$	1.70×10^{-4}
$X(\rm S^+)^d$	8.00×10^{-8}
$X(\rm Si^+)^d$	8.00×10^{-9}
$X(\rm Fe^+)^d$	3.00×10^{-9}
$X(\rm Na^+)^d$	2.00×10^{-9}
$X(\rm Mg^+)^d$	7.00×10^{-9}
$X(\rm P^+)^d$	2.00×10^{-10}
$X(\rm Cl^+)^d$	1.00×10^{-9}
$X(\rm F)^e$	6.68×10^{-9}

[a] Wakelam & Herbst (2008a)
[b] McGuire et al. (2018)
[c] Jenkins (2009)
[d] Graedel et al. (1982)
[e] Neufeld et al. (2005)

Table 2.3: Parameters used in calculating G values and rate coefficients.

Species	$E_{\rm ion}$[a] **[eV]**	$W_{\rm exc}$[b] **[eV]**	$W_{\rm s}$ **[eV]**
H_2O	12.621	11.190	3.824
O_2	12.070	8.500	3.886
O_3	12.530	4.860	3.815
CO	14.014	13.190	3.947
CO_2	13.777	13.776	3.927
NO	9.264	13.776	3.422
NO_2	9.586	21.377	3.478
O_2H	11.350	5.961	3.694
H_2O_2	10.580	10.332	3.606
CH_3OH	10.840	14.760	3.636
NH_3	10.070	9.110	3.542
H_2CO	10.880	7.940	3.641
CH_4	12.610	13.000	3.823
CH_3COCH_3	9.703	6.358	3.494

[(a)] Lias (2018)
[(b)] Keller-Rudek et al. (2013)

2.3 Network

Our three-phase chemical network is based on the one described in Ruaud et al. (2016) to which we have added the gas-phase reactions of Balucani et al. (2015). In addition to this network, we have included both (a) dissociation pathways for the major ice mantle constituents due to collisions with cosmic rays or secondary electrons and (b) reactions involving the suprathermal products. Radiochemical yields (G values) and rate coefficients were calculated using the Shingledecker-Herbst method, and are a function of $E_{\rm ion}$, $W_{\rm exc}$, and $W_{\rm s}$. Values for the ionization energy, $E_{\rm ion}$, were taken from the NIST Chemistry Webbook (Lias, 2018). The average electronic excitation energies, $W_{\rm exc}$, were estimated from the strongest UV-Vis absorption for each species

[3] The close reader will note that, while the physical parameters of TMC-1 are the same across the entire thesis, this chapter alone uses the initial elemental abundances of Graedel et al. (1982) rather than those of Hincelin et al. (2011). This chapter compares models beginning with the listed values and including radiolysis chemistry to models beginning with these same listed values and without radiolyis chemistry, however, and therefore the findings of the chapter remain intact.

(Fueki & Magee, 1963; Shingledecker & Herbst, 2018) based on spectra in the MPI-Mainz UV-Vis Spectral Atlas (Keller-Rudek et al., 2013). Finally, the average sub-excitation electron energies were calculated using the method of Elkomoss & Magee (1962). A list of both the species that undergo radiolysis as well as the associated parameters used in calculating rate coefficients are given in Table 2.3, while Table A.1.1 in Appendix A lists the new solid-phase radiolysis pathways for each species.

In our models, we assume the processes in Table A.1.1 occur both on the surface and in the ice mantle and have labeled them Types I, II, and III. Type I radiolysis corresponds to the process given in equation (R2) where species A is ionized and recombines with the newly formed electron to produce suprathermal dissociation products. Type II processes correspond to the sequence of events given in equation (R3), where A dissociates into thermal products after being collisionally excited by an energetic particle. Finally, Type III processes are characterized by equation (R4), where A is collisionally excited, but does not immediately dissociate.

As supported by previous experimental work (Bennett & Kaiser, 2005; Abplanalp et al., 2016; Bergantini et al., 2018), we assume that for a suprathermal species B^*, the lifetime in solids is much shorter ($\ll$ 1 s) than the average surface or bulk thermal hopping time, $t_{\rm hop}^{B}$ ($\gg$ 1 s at 10 K) (Hasegawa et al., 1992). As noted by Bennett & Kaiser (2005), the short lifetimes of these suprathermal species, relative to their hopping times at low temperatures, means that their solid-phase chemistry is likely dominated by reactions with neighbors. Therefore, we assume that once formed, suprathermal species only either react or relax back to the ground state. For reactions of the form:

$$A + B^* \rightarrow \text{products.} \tag{2.13}$$

we use the following formula for calculating the rate coefficients, $k_{\rm ST}(\rm cm^3 s^{-1})$:

$$k_{\rm ST} = f_{\rm br}\left[\frac{\nu_0^B + \nu_0^A}{N_{\rm site} n_{\rm dust}}\right] \tag{2.14}$$

where $f_{\rm br}$ is the product branching fraction, $n_{\rm dust}$ is the dust density - here equal to 1.8×10^{-8} cm^{-3}, $N_{\rm site}$ is the number of physisorption sites on the grain - here equal to 1.5×10^{15} cm^{-2}, and ν_0^X is the characteristic vibrational frequency for some physisorbed species, X, which is typically in the range of $1 - 3 \times 10^{-12}$ s^{-1} (Herbst & Millar, 2008). This frequency can be estimated (Landau & Lifshitz, 1976) using the formula

$$\nu_0^X = \sqrt{\frac{2 N_{\rm site} E_{\rm b}^X}{\pi^2 m_X}} \tag{2.15}$$

where m_X is the mass of X and $E_{\rm b}^X$ is the diffusion barrier, which we here set equal to 40% and 80% - for surface and bulk species, respectively - of the desorption energies used in Ruaud et al. (2016). Since the dominant mechanism for reactions involving suprathermal species in solids is likely not diffusive (Bennett & Kaiser, 2005), Eq. (2.14) is similar to the typical solid-phase bimolecular rate coefficients, but differs from them in that it does not contain either (a) a term characterizing thermal

hopping or (b) a factor accounting for tunneling through reaction barriers, since we assume that suprathermal species are sufficiently energetic to react without a barrier (Hasegawa et al., 1992).

In addition to destruction through chemical reactions, we also assume that suprathermal species can be quenched by the ice-mantle (Spinks & Woods, 1990; Bennett & Kaiser, 2005), i.e.

$$B^* + M \rightarrow B + M. \tag{2.16}$$

We use the characteristic frequency, ν_0^B, as a pseudo first-order approximation for the rate coefficient of the above process. Here, we have assumed that quenching by the solid is very fast ($\sim 10^{-14}$ s) compared to spontaneous emission ($\sim 10^{-9}$ s) and thus have neglected it as a de-excitation channel in this work.

To illustrate how this radiation chemistry is incorporated into our chemical network, consider the formation and destruction of the suprathermal species, B^*, which is produced solely via process (R2) and only reacts with A, as in Eq. (2.13). In this example then, the rate of change of $n(B^*)$ is given by the equation

$$\frac{d\,n(B^*)}{d\,t} = k_{\rm R2} n(A) - \nu_0^B n(B^*) - k_{\rm ST} n(A) n(B^*) \tag{2.17}$$

where the first term on the right gives the production of B^* via the radiolysis of A, the second term gives the quenching rate for B^*, and the third term gives the rate

of destruction via reaction with A - with k_{ST} being the rate coefficient for suprathermal reactions given in Eq. (2.14). We emphasize that in our actual network, most suprathermal species are produced from the radiolysis of more than one species, and all have more than one destructive reaction.

The suprathermal reactions we have added to our network can be grouped into two classes. Class 1 refers to those that are similar to reactions involving ground state species already included in the network, while Class 2 refers to novel reactions unlike those currently included for thermal species. To illustrate Class 1 reactions, consider the following example:

$$\mathrm{H}(s) + \mathrm{CO}(s) \rightarrow \mathrm{HCO}(s) \tag{2.18}$$

which has an activation energy of 2300 K in the Ruaud et al. (2016) network, in addition to a diffusion barrier. Here, (s) indicates either a surface or bulk species. We will later use (g) to denote gaseous species, and in cases where reactants labeled with (s) lead to products in the gas-phase, the reactants are assumed to be surface species only. Here we include the following Class 1 suprathermal reactions based on (2.18):

$$\mathrm{H}^{*}(s) + \mathrm{CO}(s) \rightarrow \mathrm{HCO}(s) \tag{2.19}$$

and

$$\mathrm{H}(s) + \mathrm{CO}^{*}(s) \rightarrow \mathrm{HCO}(s). \tag{2.20}$$

We assume no barrier for both reaction (2.19) and (2.20), as implied by results from ice irradiation experiments (Abplanalp et al., 2016). Rate coefficients for reactions (2.19) and (2.20), as well as for all similar Class 1 suprathermal reactions, are calculated in our model using Eq. (2.14). Another group of Class 1 reactions included in our network are based on work by Hudson (2017), who found ketene (H_2CCO) among the products of acetone irradiation, which could form via:

$$\mathrm{CH_3} + \mathrm{CH_3CO} \rightarrow \mathrm{H_2CCO} + \mathrm{CH_4} \tag{2.21}$$

where the CH_3 and CH_3CO radicals result from either Type I or II radiolysis of acetone. We have included both the reaction between ground state radicals as well as reactions involving a single suprathermal reactant, similar to reactions (2.19) and (2.20). A full list of these new reactions is available from the authors.

Class 2 is used to categorize novel reactions that are unlike the kinds of thermal reactions typically considered in gas/grain models. To illustrate why this type of chemistry is astrochemically interesting, consider the following Class 2 reaction:

$$\mathrm{O}(s) + \mathrm{CH_4}(s) \rightarrow \mathrm{CH_3OH}(s). \tag{2.22}$$

This type of reaction is known as an "insertion" since the oxygen atom is inserted into one of the C-H bonds to form methanol. Reaction (2.22) is highly endothermic, having an activation energy of $\sim$ 4300 K (Baulch et al., 1992); however, Bergner et al. (2017) recently found that O(^{1}D) and methane could efficiently react to form methanol in low temperature ices via this mechanism. Further evidence for the importance of solid-phase irradiation-driven insertion reactions comes from recent work by Bergantini et al. (2018), who found that such processes could lead to ethanol and dimethyl ether formation at low-temperatures. Thus, Class 2 reactions may contribute to the formation of COMs, even in cold interstellar environments.

In this study, we added Class 2 reactions for both C* and O*, as listed in Table A.1.2 of Appendix A. Many of these new reactions were drawn from combustion chemistry. Since cosmic rays, like other forms of ionizing radiation, produce highly non-thermal species, some of the endothermic reactions previously considered in the context of high-temperature systems become relevant when considering irradiated low-temperature ices.

We have also included gas-phase destruction reactions for HOCO. In addition to photodissociation by internal and external UV photons, the reactions listed in Table A.1.3 of Appendix A.1.3 were added to the Ruaud et al. (2016) network, with neutral-neutral rate coefficient parameters given in terms of α, β, and γ using the Arrhenius-Kooij formula:

$$k_{\rm AK} = \alpha \left(\frac{T_{\rm gas}}{300\,{\rm K}} \right)^{\beta} \exp\left(-\frac{\gamma}{T_{\rm gas}} \right) \tag{2.23}$$

where $T_{\rm gas}$ is the kinetic temperature of the gas.

For reactions between the polar neutral HOCO and ions, we use the Su-Chesnavich capture theory (see Woon & Herbst (2009a) and references therein). For HOCO, values of $\mu_{\rm D} = 3.179$ D and $\alpha_{\rm p} = 2.739$ Å^3 were utilized for the dipole and dipole polarizability, respectively (Johnson, 2016).

2.4 Results and Discussion

2.4.1 HC_2O

The ketenyl radical, HC_2O, was first observed in the cold ($T_{\rm kin} \approx 15$ K) starless cores Lupus-1A and L483 by Agúndez et al. (2015), who derived a column density of $\sim 5 \times 10^{11}$ cm^{-2} for both sources. Chemical simulations were run assuming HC_2O formation via the reaction of OH and C_2H. It was noted that such simulations underproduce the ketenyl radical by about six orders of magnitude, leading the authors to posit the existence of "a powerful formation mechanism" to counterbalance HC_2O destruction pathways.

As shown in Fig. 2.1, the inclusion of radiation chemistry in our TMC-1 simulations results in significant enhancements of HC_2O - roughly four orders of magnitude for the gas, ice surface, and ice bulk. At early simulation times ($< 10^3$ yr), the dominant formation route for gas-phase ketenyl radical is

$$\mathrm{OH}^*(s) + \mathrm{CCH}(s) \rightarrow \mathrm{HC_2O}(g) + \mathrm{H}(g). \tag{2.24}$$

At all later simulation times ($> 10^3$ yr), HC_2O is mainly formed via

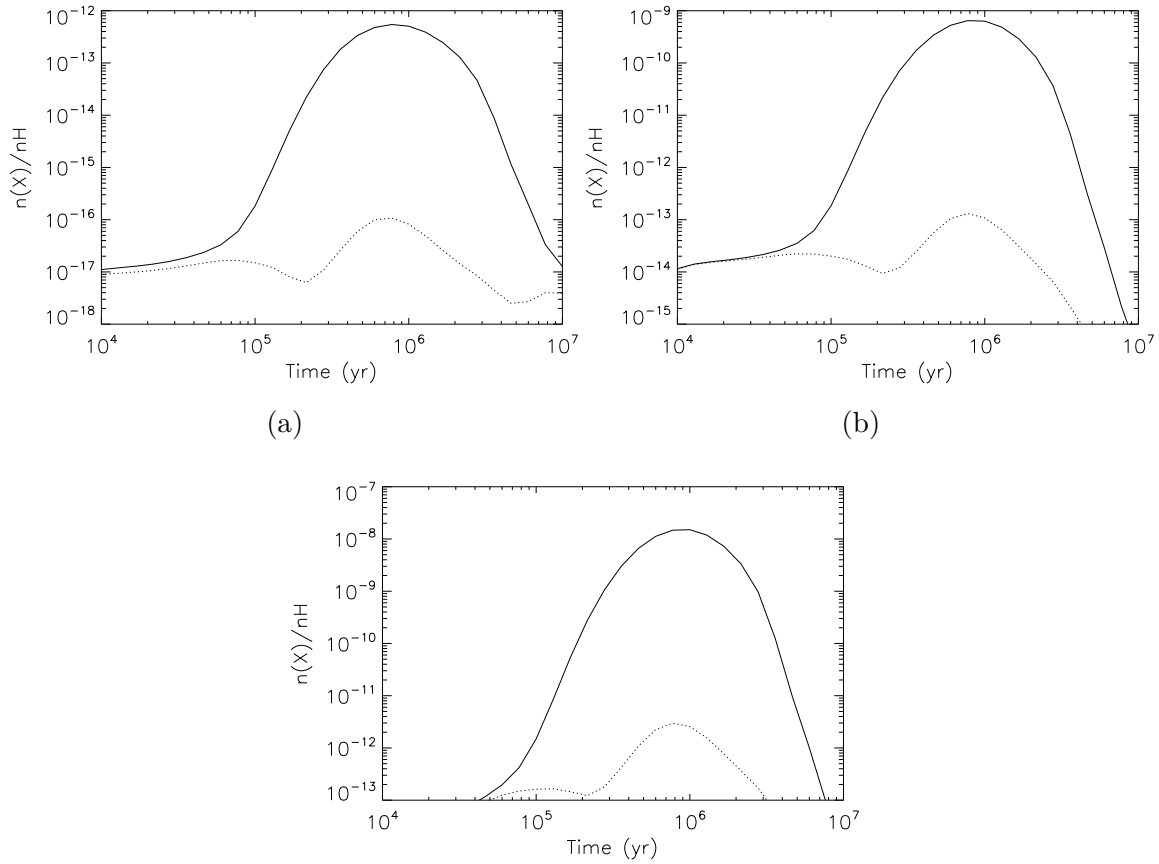

Figure 2.1: Simulated TMC-1 abundances of HC_2O in the gas (a), on the grain/ice surface (b), and in the ice bulk (c), calculated both with (solid line) and without (dotted line) radiation chemistry.

$$\mathrm{H}(s) + \mathrm{CCO}(s) \rightarrow \mathrm{HC_2O}(g). \tag{2.25}$$

In both TMC-1 simulations with and without radiation chemistry, there is little difference in the CCH abundance at all times and for all phases of the model; however, the ice surface and bulk abundances of CCO are enhanced via the reaction

$$C^*(s) + CO(s) \rightarrow CCO(s) \tag{2.26}$$

where the suprathermal carbon atoms are formed mainly via the radiolysis of CO.

Though our simulations still underproduce gas-phase HC_2O compared with observed values of Agúndez et al. (2015), the significant enhancements seen in models run with radiation chemistry suggest that perhaps radiation chemistry is their speculated powerful formation mechanism. Since we have not included any non-thermal desorption mechanisms caused by the direct cosmic ray bombardment of dust grains, such as sputtering, it may be that the impact of radiation chemistry on gas-phase abundances is greater than what is implied by our results here.

2.4.2 $HCOOCH_3$

As with HC_2O, the abundance of methyl formate ($HCOOCH_3$) is enhanced in all three phases of the model. In simulations including radiation chemistry, the main production pathways for gas-phase methyl formate are

$$HCO^*(s) + CH_3O(s) \rightarrow HCOOCH_3(g) \tag{2.27}$$

and

$$HCO(s) + CH_3O^*(s) \rightarrow HCOOCH_3(g). \tag{2.28}$$

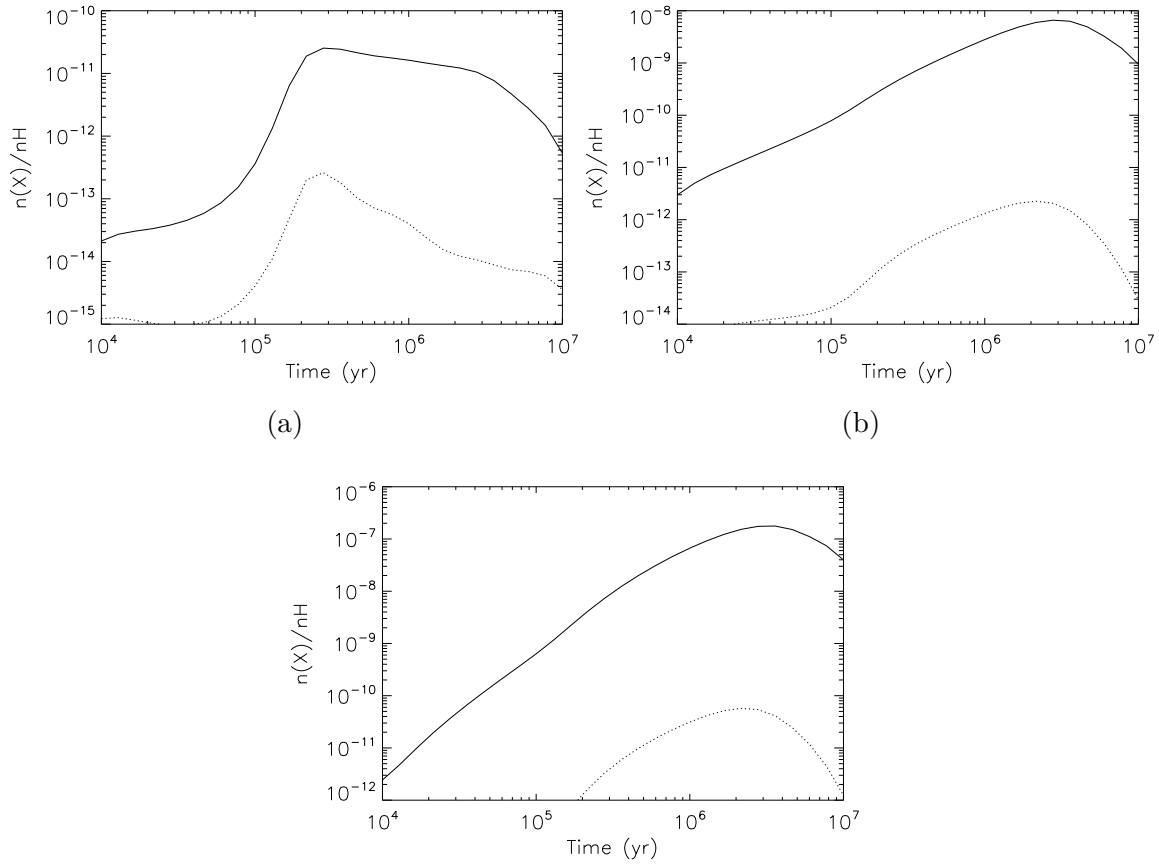

Figure 2.2: Simulated TMC-1 abundances of $HCOOCH_3$ in the gas (a), on the grain/ice surface (b), and in the ice bulk (c), calculated both with (solid line) and without (dotted line) radiation chemistry.

Here, the suprathermal HCO is produced mainly via the Type I radiolysis of formaldehyde:

$$H_2CO(s) \rightsquigarrow H^*(s) + HCO^*(s) \tag{2.29}$$

and the methoxy radical is produced from the Type I decomposition of methanol:

$$CH_3OH(s) \rightsquigarrow H^*(s) + CH_3O^*(s). \tag{2.30}$$

Methyl formate has been a focus of several recent studies which likewise examined its formation in cold cores (Balucani et al., 2015; Chang & Herbst, 2016; Vasyunin & Herbst, 2013a). In Balucani et al. (2015) gas-phase production via

$$O + CH_3OCH_2 \rightarrow HCOOCH_3 + H \tag{2.31}$$

was considered. As shown in Fig. 2.2, our models predict a peak gas-phase relative abundance of $\sim 3 \times 10^{-11}$ for methyl formate. Our peak value here is $\sim 500\%$ larger than than the $\sim 5 \times 10^{-12}$ obtained by Balucani and coworkers in models where they used the standard chemical desorption fraction of 1%, the efficiency we assume throughout this work. Similarly, Chang & Herbst (2016) achieved somewhat higher gas-phase abundances of methyl formate in a number of their cold core simulations; however, they found that such results required both an enhanced chemical desorption fraction of 10% and the addition of a novel "chain reaction mechanism" that is not easily implemented in the macroscopic model we have utilized.

Though the number of grain-surface formation routes for COMs like methyl formate are limited in our network - compared with those used in hot core simulations (Garrod et al., 2017) - these results suggest radiation-chemical reactions may be able to drive the formation of COMs even under cold core conditions. As shown, the production of these complex species is possible because of the suprathermal reactants which form

as a result of the radiolytic dissociation of molecules in dust grain ice-mantles.

2.4.3 Results Using Enhanced Ionization Rates

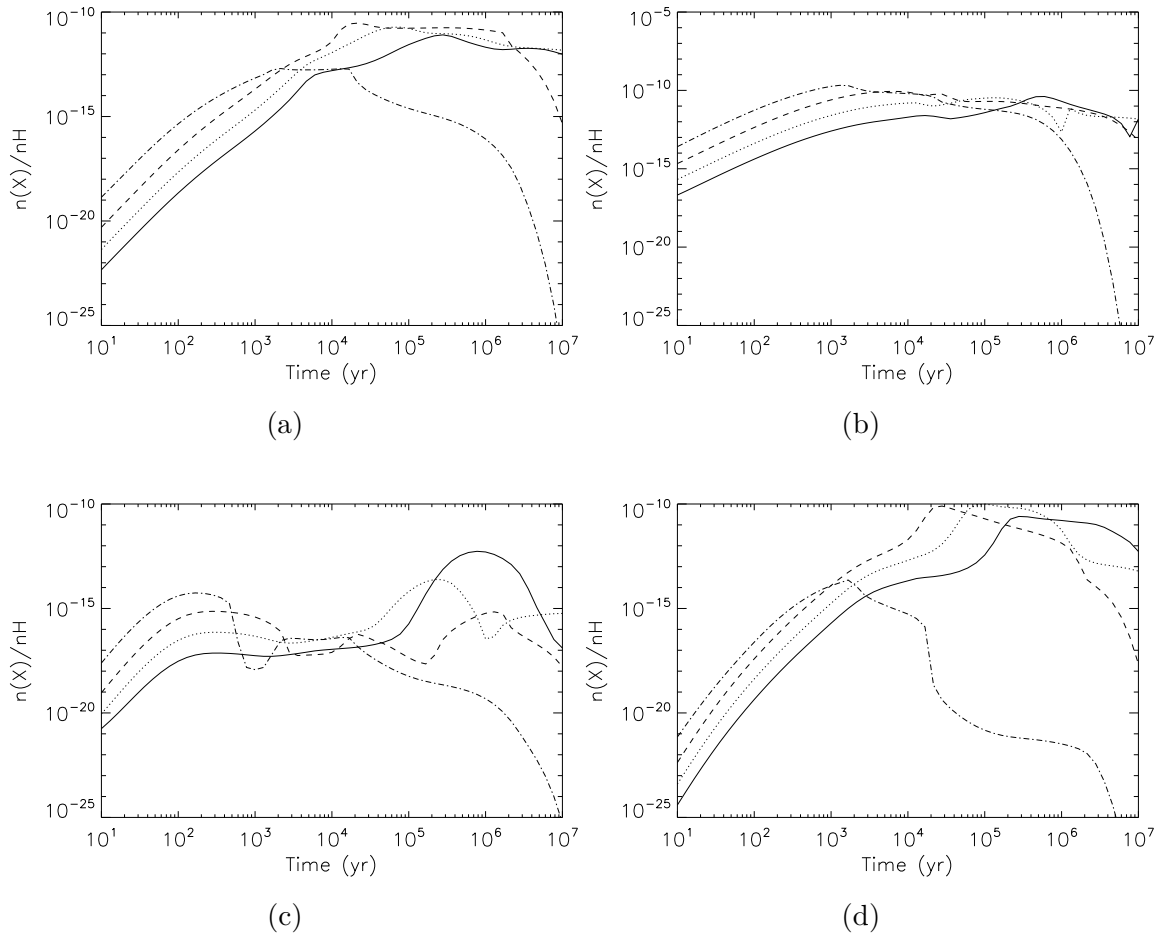

Figure 2.3: Calculated gas-phase abundances of HOCO (a) NO_2 (b) HC_2O (c), and $HCOOCH_3$ (d) calculated at ionization rates of 10^{-17} s^{-1} (solid line), 10^{-16} s^{-1} (dotted line), 10^{-15} s^{-1} (dashed line), and 10^{-14} s^{-1} (dot-dashed line).

Additional simulations were run in order to examine the effect of the new radiation chemistry at high ζ. As mentioned in §2.2 - and shown in Table 2.1 - we assume that the simulated hypothetical sources are physically identical to TMC-1 except for having higher ionization rates. The results from these model runs for HOCO, NO_2,

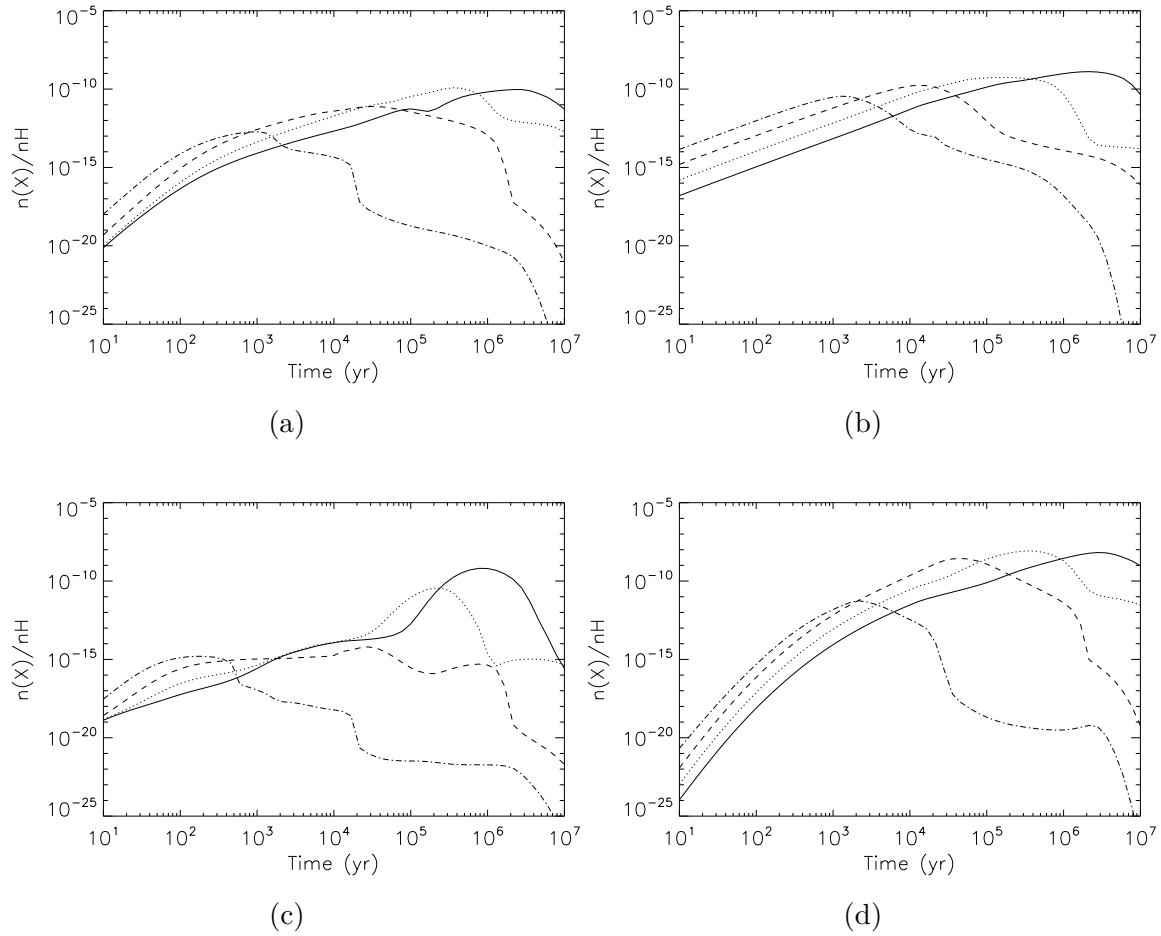

Figure 2.4: Calculated grain-surface abundances of HOCO (a) NO_2 (b) HC_2O (c), and $HCOOCH_3$ (d) calculated at ionization rates of 10^{-17} s^{-1} (solid line), 10^{-16} s^{-1} (dotted line), 10^{-15} s^{-1} (dashed line), and 10^{-14} s^{-1} (dot-dashed line).

HC_2O, and $HCOOCH_3$ are depicted in Figs. 2.3-2.5, which show the gas, surface, and bulk abundances, respectively.

As one can see from a comparison of Figs. 2.3 - 2.5, several trends emerge as the ionization rate changes. First, since, as previously demonstrated, the abundances of HOCO, NO_2, HC_2O, and $HCOOCH_3$ are enhanced due to radiochemical processes, it is reasonable that their abundances should tend to increase with increasing ζ. This effect is most obvious at very early times before $\sim 10^3$ yr, with the correlation

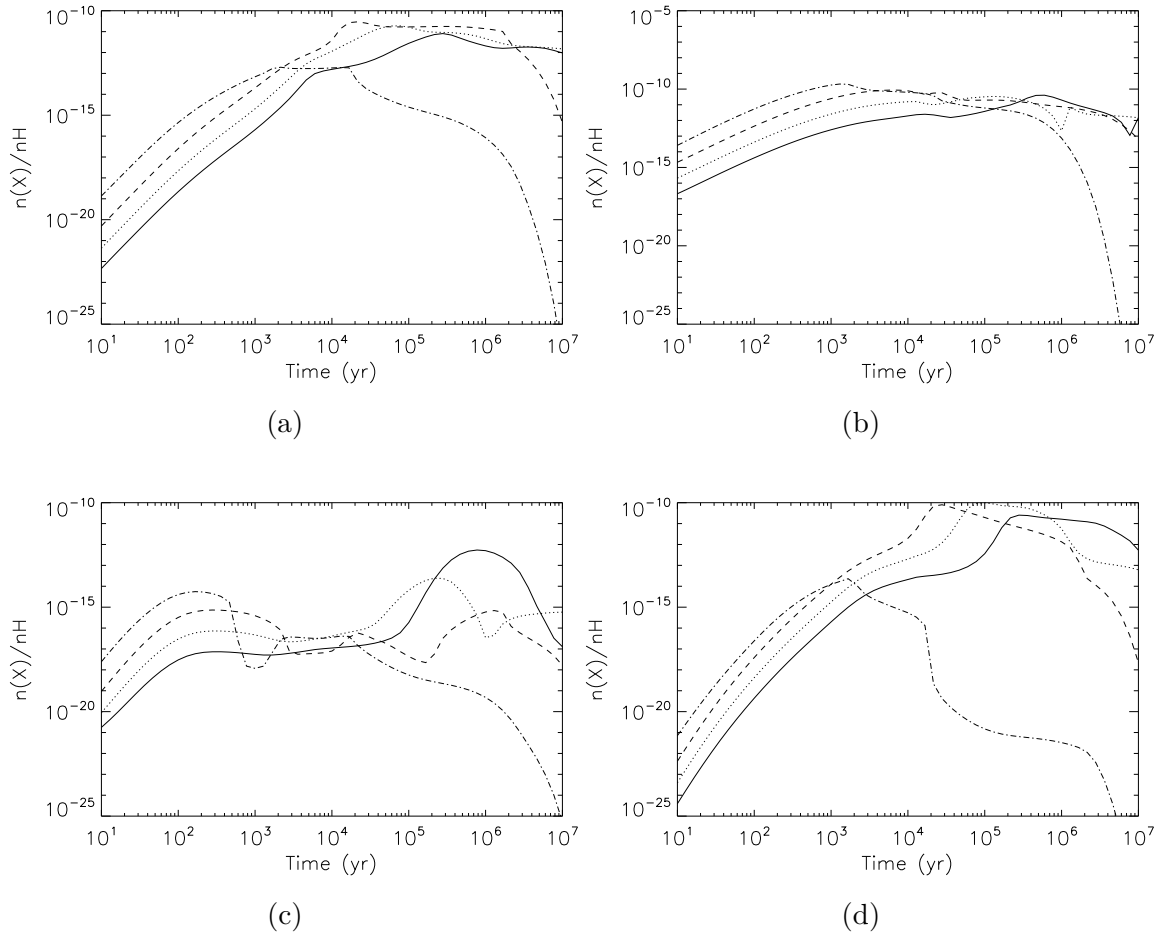

Figure 2.5: Calculated bulk-ice abundances of HOCO (a) NO_2 (b) HC_2O (c), and $HCOOCH_3$ (d) calculated at ionization rates of 10^{-17} s^{-1} (solid line), 10^{-16} s^{-1} (dotted line), 10^{-15} s^{-1} (dashed line), and 10^{-14} s^{-1} (dot-dashed line).

between the two clearly observable in Figs. 2.3 - 2.5. At intermediate times however, between $\sim$ 10^3-10^6 yr, the relationship between abundance and ζ begins to break down, particularly in the gas phase. Generally, we find that the higher the ionization rate, the faster the peak abundance is reached, and the lower the peak value - a trend that can most easily be seen in Figs. 2.4 and 2.5, which show the surface and bulk abundances, respectively. After $\sim$ 10^6 yr, an anti-correlation between ζ and abundance emerges for most of the species shown. The reasons for this behavior are

complex, but are driven in part by (a) the increased radiolytic destruction of surface and bulk species into more weakly bound fragments, and (b) the greatly increased gas-phase abundances of ions such as H^+ and C^+, reactions with which further reduce the abundance of the neutral species considered here.

2.5 Conclusions

We have utilized the theory described in Shingledecker & Herbst (2018) in an initial attempt to incorporate radiation chemistry into an existing chemical network. Simulations of the cold core TMC-1 were run, both with and without the new cosmic ray-induced reactions. We also modeled several hypothetical sources which were physically identical to TMC-1 other than having enhanced ionization rates. The major results of the simulations described in this work are the following:

- Radiation chemistry can result in substantially enhanced abundances in all three model phases for a variety of species, including COMs.
- These enhancements in abundance occur mainly as a result of reactions involving suprathermal species formed from the radiolytic dissociation of simple ice mantle constituents.
- Even under cold core conditions, these suprathermal species can react quickly by a variety of mechanisms, including insertion, which we found to be particularly important in increasing the abundance of COMs.
- We predict that HOCO, and perhaps NO_2, could be observable in TMC-1, given a sufficiently deep search.

- The addition of radiation chemistry substantially improves agreement between calculated and observed abundances of HC_2O.
- For the neutral species considered here, ionization rates of 10^{-16} s^{-1} or higher generally resulted in reduced abundances in all model phases at times greater than $\sim 10^3$ yr.

It should be emphasized that these results, while promising, are necessarily preliminary in nature, given the novelty of incorporating radiation chemistry into astrochemical models. More work is needed to better characterize both (a) cosmic ray-induced radiolysis and chemistry and (b) secondary effects such as the non-thermal desorption of grain species triggered by cosmic ray bombardment. These non-thermal desorption mechanisms, such as sputtering, desorption induced by electronic transitions (DIET), electron stimulated ion desorption (ESID), and Auger stimulated ion desorption (ASID) (Ribeiro et al., 2015) are particularly promising since they could provide a means of enriching gas-phase abundances at low temperatures, and are therefore a natural complement to the non-thermal chemistry described here.

As we have demonstrated in this work, the addition of cosmic ray-driven solid-phase reactions can improve existing astrochemical models in a number of significant ways. First, the addition of this non-thermal chemistry increases the realism of models, since cosmic ray bombardment of ice mantles certainly occurs in the ISM. Moreover, a consideration of solid-phase radiation chemistry both helps to explain how COMs like methyl formate could efficiently form in cold cores (Balucani et al., 2015; Chang & Herbst, 2016; Vasyunin & Herbst, 2013a), and improves the agreement between calculated and observational abundances for HC_2O. Cosmic ray-driven ice chemistry is thus attractive as a component of future astrochemical modeling studies.

Chapter 3

Radiative Association between Neutral Radicals in the Interstellar Medium: $CH_3 + CH_3O$

Uncertainties in the production mechanisms of interstellar complex organic molecules call for a precise investigation of gas-phase synthesis routes for these molecules, especially at low temperatures. Here, we report a study of the gas-phase formation of dimethyl ether from the neutral radicals methyl and methoxy via the process of radiative association. This process may be important to synthesize dimethyl ether and species such as methyl formate, for which dimethyl ether is a precursor. The reaction is found to be rapid by the standards of radiative association, especially at 10 K, where its rate coefficient is calculated by two different methods to be 3×10^{-11} *or* 2×10^{-10} *cm^3 s^{-1}; the lower rate is calculated with a more precise theory and is likely more accurate. Insertion of this reaction into the Nautilus network is found not to explain fully the abundance of dimethyl ether in cold and pre-stellar cores, especially in those cores with the highest dimethyl ether abundances.*[1]

[1]Originally published as Tennis et al. (2021). Quantum chemical calculations by J.-C. Loison, except for those in §3.5 by J. D. Tennis. Rate calculations and modeling by J. D. Tennis.

3.1 Introduction

The interstellar medium (ISM) owes much of its chemical complexity to grain-surface processes. As the known diversity of larger gas-phase species in the ISM continues to increase, however, new production mechanisms for complex organic molecules (COMs) must be investigated. Garrod et al. (2008) have shown that complex organic molecules can be formed efficiently on the surfaces of cold grains at temperatures as low as 20 to 30 K in star-forming regions, and that as these systems continue to develop and warm up, thermal desorption increases the gas-phase abundance of COMs. Thus, molecules formed on the grain become detectable in the gas phase. Recently, COMs have been observed in cold and prestellar cores at temperatures as low as 10 K despite the difficulty of diffusive formation on grains at this temperature as well as the need for non-thermal desorption mechanisms to detect the species (Vastel et al., 2014; Öberg et al., 2010; Jaber et al., 2014; Cernicharo et al., 2012a; Bacmann et al., 2012). Balucani et al. (2015) and Vasyunin & Herbst (2013b) have shown that neutral-neutral gas-phase reactions can play an important role in the formation of COMs. The radiative association of neutral radical species is a particularly good candidate for increasing chemical complexity because of the inverse temperature dependence of its rate coefficient and the high relative abundance of neutral species compared with ions in the interstellar medium (ISM).

Radiative association occurs via the stabilization of a collision complex, or unstable intermediate species, by the emission of a photon. The collision complex, a species that sits above a local potential minimum, is formed by the exothermic association of two gas-phase species, and the process benefits from the inverse temperature dependence of its rate coefficient and the much smaller timescales of radiative stabilization as compared with collisional stabilization in the low densities of cold, dark clouds.

Competitive dissociation and reaction mechanisms must still be considered in the calculation of a radiative association rate coefficient.

One of the COMs detected in several cold and prestellar cores is dimethyl ether (CH_3OCH_3). It has been seen at a relative abundance of 2×10^{-11} toward the cold, dense core B1-b (Cernicharo et al., 2012a), 2.5×10^{-10} towards the cyanopolyyne peak in TMC-1 (Agúndez et al., 2021) and 1.5×10^{-10} at its main peak (Calcutt et al., 2018), 1.3×10^{-10} around the dense core L483 (Agúndez et al., 2019), 2×10^{-11} in the prestellar core L1689B, (Bacmann et al., 2012), and 7×10^{-10} toward the Barnard 5 molecular cloud (Taquet et al., 2017). Although a number of different formation routes have been reported in the literature, it is unclear that the abundance of dimethyl ether is fully understood. One possibility reported but not treated in detail is radiative association.

The radiative association to form dimethyl ether is thought to occur via the association of the radicals methyl (CH_3) and methoxy (CH_3O) (Balucani et al., 2015; Vasyunin & Herbst, 2013b). Both dimethyl ether and the methoxy radical have been observed in cold, dark clouds while the nonpolar methyl radical has been detected towards the galactic center in the infrared, but not in a cold dark cloud (Öberg et al., 2010; Bacmann et al., 2012; Cernicharo et al., 2012a; Jaber et al., 2014; Feuchtgruber et al., 2000). The dimethyl ether collision complex formed by association of the neutral methyl and methoxy radicals has several output channels all located above the input channel except for the roaming, as previously calculated by Sivaramakrishnan et al. (2011). This roaming pathway describes the bimolecular pathway leading from CH_3 + CH_3O to CH_4 + H_2CO well with a high rate at room temperature (around 2×10^{-11} cm^3 s^{-1} (Tsang & Hampson, 1986; Sivaramakrishnan et al., 2011) even if there is also a direct pathway leading to CH_4 + H_2CO. This direct pathway does

not involve the formation of CH_3OCH_3 and is not considered in this work. Note that in addition to the paths computed by Sivaramakrishnan et al. (2011), there is a very high barrier on the competitive exit path toward dissociation into methane and formaldehyde (around 1.4 eV above the CH_3 + CH_3O energy), making association much more likely than the bimolecular exit path and making this system particularly interesting to study.

Previous estimates of the reaction rate coefficient between the methyl and methoxy radicals vary but indicate that the rate coefficient of this reaction could be sufficiently large to explain the abundance of dimethyl ether and its daughter product methyl formate (Vasyunin & Herbst, 2013b; Balucani et al., 2015). Here, the previous approaches are compared with a microcanonical as well as a less detailed canonical calculation. The microcanonical approach is likely to be more accurate for interstellar environments, which often cannot be represented well by one average temperature (Herbst, 1985). Our microcanonical approach uses the phase-space model, which conserves angular momentum and energy in the calculation of association and dissociation probabilities.

3.2 Theory

As noted earlier, the concentration of the collision complex is governed by a number of processes, which include formation, redissociation back into reactants, production of bimolecular products, and stabilization by radiative emission and, at higher densities, collisional stabilization. Each of these several steps has an associated rate coefficient. Under the steady state assumption, the overall microcanonical rate coefficient k_{ra} for

radiative association is given by the equation (Herbst, 1985):

$$k_{\mathrm{ra}}(J_{\mathrm{A}}, J_{\mathrm{B}}, J, E) = \frac{k_1(J_{\mathrm{A}}, J_{\mathrm{B}}, J, E)k_r}{k_{-1}(J, E) + k_{\mathrm{r}} + k_2(J, E)} \tag{3.1}$$

where J is the total angular momentum, k_1 is the association rate coefficient for the reactants to form a complex, k_{r} is the radiative stabilization rate, k_{-1} is the rate at which the complex redissociates into the precursors, and k_2 is the rate at which the complex dissociates into new products. The rate coefficient for complex formation is given by the equation

$$k_1 = v\sigma(J_{\mathrm{A}}, J_{\mathrm{B}}, J, E), \tag{3.2}$$

where σ is the phase space cross section (Light, 1967; Herbst, 1987) and v is the relative velocity between the two reactants. This cross section sums over all possibilities up to a maximum value of the collisional angular momentum L, for fixed values of the angular momenta J_{A} and J_{B} of the reactants A and B, as shown in the equation

$$\sigma = (\frac{\pi h^2 G}{2\mu E_{\mathrm{coll}}}) \sum_{L=0}^{L_{\mathrm{max}}} (2L + 1)P(J). \tag{3.3}$$

Here G is the ratio of the electronic degeneracy of the complex to that of the reactants assuming the reactants are in the ground electronic state, μ is the reduced mass of the reactants, E_{coll} is the collisional energy of the reactants, and $P(J)$ is the probability that the complex is formed with a particular total angular momentum J, as given by

$$P(J) = \sum_{J_r} \frac{(2J+1)}{(2J_r+1)(2L+1)} \frac{(2J_r+1)}{(2J_A+1)(2J_B+1)}. \tag{3.4}$$

where J_r is the result of the vector sum of J_A and J_B, which then combines vectorially with L to form the total angular momentum J. L_{max} is the collisional angular momentum at which the peak of the centrifugal barrier of the attractive potential equals the translational energy of the reactants, so that an excess of angular momentum does not tear the collision complex apart (Light, 1967).

The choice of a potential for our calculation is difficult to decide. Long-range isotropic capture potentials are simple but may be less accurate than anisotropic potentials especially with short-range effects. Anisotropic neutral-neutral potentials at long and short range as well as attractive and repulsive terms for such systems were tested by Liao & Herbst (1995) for the reactions CN + C_2H_2 and C + C_2H_2. These systems had been studied in the laboratory, the CN system from room temperature down to low temperatures near 25 K, and the C reaction at room temperature. Liao & Herbst (1995) found that the effect of long-range anisotropy and short-range repulsion on isothermal capture theories was minimal at low temperatures, while at higher temperatures short-range repulsive terms had more of an effect than did anisotropic potentials and are able to bring the calculated rate coefficients into agreement with experiment whereas the isotropic models yield a rate coefficient three times the measured one. Even at 300 K, the differences are not great. Here we used for simplicity an isotropic long-range $-Cr^{-6}$ attractive potential between a dipole and an induced

dipole for the studied radiative association. With this potential, $L_{\max}$ is given by

$$L_{\max}(L_{\max}+1) = 32C^{1/3}\mu\hbar^{-2}E_{\text{coll}}^{2/3} \tag{3.5}$$

with

$$C = \frac{3}{2}\frac{I_{\text{A}}I_{\text{B}}}{(I_{\text{A}}+I_{\text{B}})}\alpha_{\text{A}}\alpha_{\text{B}} + \mu_{\text{B}}^2\alpha_{\text{B}}. \tag{3.6}$$

Here E_{coll} is the initial translational energy of the reactants, μ is the reduced mass of the reactants, α is the dipole polarizability of the reactant in question, μ_{B} is the dipole of polar neutral reactant B, and I_{A} and I_{B} are the ionization potentials.

The rate coefficient for complex redissociation into reactants $k_{-1}(J,E)$, where E is the total energy, can be obtained using microscopic reversibility and the energy density (see (Light, 1967; Klots, 1971; Herbst, 1985).) The rather complex expression is given by the equation:

$$k_{-1} = \frac{1}{h(2J+1)\rho_\nu(E_{\text{vib}}/\sigma)}\sum_{J'_{\text{A}}}\sum_{J'_{\text{B}}}\sum_{vib}[(2J'_{\text{A}}+1)(2J'_{\text{B}}+1)/\sigma_{\text{A}}\sigma_{\text{B}}]\sum_{L'}\sum_{J'_{\text{r}}}1 \tag{3.7}$$

for two nonlinear reactants where ρ_ν is the complex vibrational density of states, σ_{A} and σ_{B} are the symmetry numbers for the reactants (here, the "products" of redissociation), and J'_{A}, J'_{B}, J'_{r}, and L' are the product quantum numbers analogous to those for complex formation. The product channel obeys a triangle rule with J'_{A} and J'_{B} adding vectorially to possible values of J'_{r}, and J'_{r} and L' adding vectorially to J. Any available vibrational states of A and B after redissociation of the complex are included in the summation over "vib." The complex density of vibrational states, ρ_ν,

is adapted from the ro-vibrational density used in the initial canonical equilibrium theory of radiative association (Herbst, 1979). Deletion of the rotational states as done by Marcus & Rice (1951) leads to:

$$\rho_\nu = \frac{(D_0 + V_{\rm eff} - E_{\rm rot} + E_{\rm z})^{s-1}}{s! hc\sigma \sum_{\rm i} h\nu_{\rm i}}, \tag{3.8}$$

where D_0 is the strength of the complex bond formed, $V_{\rm eff}$ is the effective maximum potential energy, combining the centrifugal barrier and the long-range potential, s is the number of vibrational degrees of freedom, σ is the complex symmetry number, and the $\nu_{\rm i}$ are the frequencies of the vibrational modes of the complex.

Once a collision complex is formed, it can re-dissociate into reactants or emit a photon and thereby stabilize the complex and complete the process of radiative association. In some cases, there is a third option, as mentioned in §3.1, and contained in the k_2 term of equation (1) of dissociation of the complex to form at least one exothermic two-body product channel. The rate of formation of new products depends on the energy barrier in excess of the product energy via the RRKM treatment (Miller, 1979):

$$k_2 = \frac{(s-1)! \prod_{\rm i}^{s} \hbar\nu_{\rm i}}{2\pi\hbar E^{s-1}} \sum_n P(E_{1,{\rm n}}) \tag{3.9}$$

where s is the number of modes in the complex and therefore s-1 is the number of modes in the transition state, $\nu_{\rm i}$ are the vibrational modes of the complex, $\nu_{\rm i}^{\#}$ are the vibrational modes of the transition state, E is the energy of the complex, and $P(E_{1,{\rm n}})$ is the probability of tunneling through a particular mode dependent on the energy in that mode, E_1, as given in Miller (1979).

Another consideration for the collision complex is that it may "roam" into other channels on other reaction pathways. Because roaming is not a standard part of a phase space theory, any information about roaming channels is best included with a roaming rate coefficient directly from the results of roaming calculations, and added to the k_2 term of equation (1). This is discussed in more detail in the §3.3.

Radiative association also depends on the rate of stabilizing emission. Stabilizing emission is most likely to come through an infrared-active channel, and larger molecules are more likely to have more of these. As shown by Herbst (1982), the rate coefficient of radiative stabilization k_r can be approximated by the harmonic formula:

$$k_\mathrm{r} = \frac{E_\mathrm{vib}}{s} \sum_{i=1}^{s} \frac{A_{1\to 0}^{(i)}}{h\nu_i} \tag{3.10}$$

where E_vib is the vibrational energy of the complex, s is the number of vibrational modes in the collision complex, the ν_i are the vibrational frequencies, and each $A^{(i)}$ is the Einstein A coefficient for emission from the first excited vibrational state of mode i to the ground vibrational state. The Einstein A coefficients are given by:

$$A_{1\to 0}^{(i)} = \frac{8\pi}{c}\nu_i^2 I, \tag{3.11}$$

where I is the intensity in units of km/mol (Herbst, 1982). This formula contains the assumption that the complex can be stabilized by the emission of a single photon; that is, that the complex lies above the dissociation limit of the stable molecule, but the emission of a single photon brings the complex below the dissociation energy.

While the harmonic approximation serves as a good estimate, the emission rate co-

efficient $k_{\rm r}$ can increase with anharmonic contributions. Since the overall radiative association rate coefficient $k_{\rm ra}$ scales with the emission rate as long as it does not become very large so as to dominate the denominator of equation (1), the results given below can be considered conservative estimates of the radiative association rate coefficient and anharmonic terms can contribute as much as a factor of five to the overall rate coefficient. The multiple and sometimes competing effects of anharmonicity are discussed in Herbst (1982).

The microcanonical phase space approach depends on the amount of energy contained in the system of nine atoms in a CH_3OCH_3 collision complex, but models of the ISM are more often described by one temperature. To achieve this change, each of the constituent rate coefficient terms in Eq. (3.1) is calculated at a particular energy and angular momentum, with the incoming rotational energies from the reactant angular momenta $J_{\rm A}$ and $J_{\rm B}$ factored out and considered separately. $k_{\rm ra}$ is found for each combination of translational energy, angular momentum, $J_{\rm A}$ and $J_{\rm B}$ and summed over each accessible value of J from 0 to $J_{\rm max}$. Then, each $k_{\rm ra}$ is integrated according to a Maxwell-Boltzmann distribution from 0 to 12 kT. These bounds allow for every value of the energy to be considered, though the higher energies are weighted more lightly since they are relatively unlikely. This gives a thermalized value of $k_{\rm ra}$, and rotational populations are the last consideration. The relative contributions for each possible value of angular momenta $J_{\rm A}$ and $J_{\rm B}$ are weighted by the probabilities of finding each reactant in the particular rotational state, so that higher rotational levels also contribute less to the total overall rate.

To get a sense of the uncertainty of our phase space results, we have also performed calculations by adapting a simpler canonical theory in which the ratio of k_1 to k_{-1} is treated by canonical partition functions. Based on prior calculations on both radiative

and three-body association on ion-neutral systems, the results of this canonical theory are likely to be upper limits (Herbst, 1980).

3.3 Results

The parameters needed to carry out the calculations for the processes described above are given in Table 3.1, where cgs-esu units are given to calculate the potential. Calculations are from Tennis et al. (2021) unless otherwise noted.

Table 3.1: Molecular Parameters Used in Radiative Association Calculations.

Species	**Parameter Value**
	Ionization Potential (eV)[a]
CH_3	9.842
CH_3O	10.72
	Polarizability (cm^3)[a]
CH_3	2.335 x 10^{-24}
CH_3O	3.089 x 10^{-24}
	Dipole Moment (Debye)[a]
CH_3O	2.7065
	Electronic Degeneracy [a,b]
CH_3	2
CH_3O	2
CH_3OCH_3*	1
	Total Energy at 0 K (kcal mol^{-1})[c]
CH_3	20.657

CH_3O	25.089
CH_3OCH_3	53.233
Well Depth (kcal mol^{-1})[c]	
Collision Complex	83.179
Rotational Constants (cm^{-1})[c,d]	
CH_3	9.45, 4.725
CH_3O	5.198, 0.987
CH_3OCH_3	0.505
Vibrational Modes (cm^{-1})[d]	
CH_3	523.7581, 1415.5889, 1415.6093, 3133.4106, 3310.4496, 3310.7025
CH_3O	754.3471, 972.9141, 1137.2748, 1384.2731, 1389.6156, 1516.7122, 2963.9264, 3033.8271, 3077.0303
CH_3OCH_3	222.1194, 270.1842, 426.4228, 983.0668, 1137.976, 1174.0569, 1204.9337, 1237.4963, 1279.2369, 1463.05, 1496.1804, 1496.8319, 1503.3653, 1507.4301, 1519.459, 3011.2543, 3019.164, 3061.9497, 3067.8806, 3142.9954, 3144.0552
$CH_3OCH_3^{\#}$	1647.9055i[e], 307.8435, 321.9863, 458.7175, 777.015, 942.1068, 1022.9967, 1152.4847, 1192.5049, 1270.5918, 1364.4524, 1403.0082, 1467.6793, 1481.8891, 1530.5725, 2265.3745, 2836.3531, 2950.971, 3061.285, 3216.8511, 3288.5714
Radiative Intensity (km/mol)[d]	
CH_3OCH_3	0.0, 5.3022, 2.9165, 35.4504, 18.4772, 0.0, 7.8391, 128.1823, 8.2952, 2.0703, 0.0, 0.0688, 11.573, 14.9355, 4.0265, 48.0799, 50.0564, 97.8169, 0.0002, 22.3102, 15.1701

[(a)] Johnson (1999)

[b]Ground electronic state assumed.

[c]Radicals are treated as symmetric tops; dimethyl ether is treated as a spherical top using the geometric mean.

[d]Tennis et al. (2021)

[e]This imaginary frequency is used only in the calculation of the tunneling rate under the transition state barrier leading from the complex to the competitive exit channel. The transition state is labelled with the # sign.

Following the processes described in §3.2 above, the radiative association rate coefficient was calculated for the temperature range of 10 K to 300 K. The radiative association rate coefficients as a function of temperature between the methyl and methoxy radicals, as calculated with the phase space approach and with the older canonical approach (Herbst, 1980) are listed in Table 3.2, and shown in Figure 3.1.

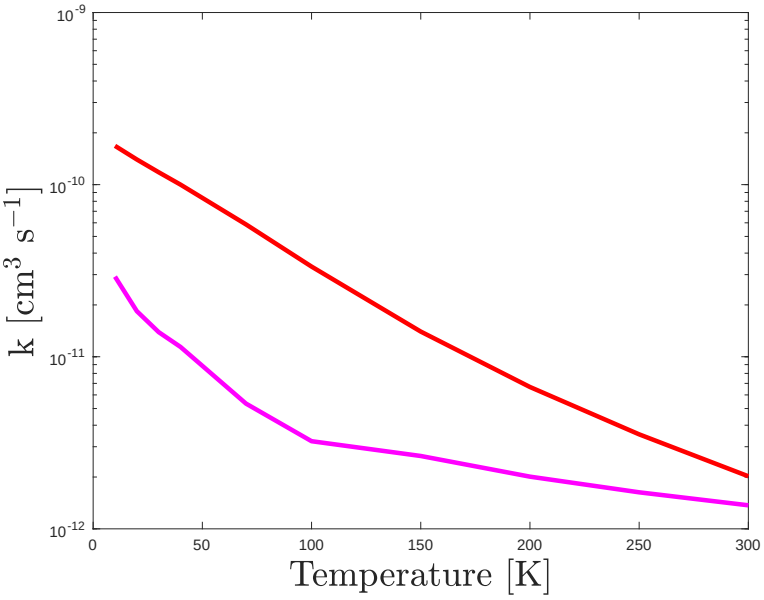

Figure 3.1: Canonical (red) and Phase-Space (magenta) results for the radiative association rate coefficient between methyl and methoxy radicals, from 10 K to 300 K.

Table 3.2: Results for Methyl-Methoxy Radiative Association Rate Coefficients as a Function of Temperature

Temperature (K)	**Canonical k_{ra} (cm^3 s^{-1})**	**Phase-space k_{ra} (cm^3 s^{-1})**
10	1.68(-10)	2.92(-11)
20	1.40(-10)	1.84(-11)
30	1.18(-10)	1.39(-11)
40	1.00(-10)	1.14(-11)
70	5.87(-11)	5.34(-12)
100	3.34(-11)	3.23(-12)
150	1.40(-11)	2.65(-12)
200	6.67(-12)	2.01(-12)
250	3.54(-12)	1.63(-12)
300	2.02(-12)	1.37(-12)

Notes. a(b) indicates a x 10^b.

As expected, there is an overall negative temperature dependence which is roughly the same for the canonical and phase-space rate coefficients (see Figure 3.1, though the canonical rate coefficient is larger by a factor of 6-10 in the range 10 K to 100 K. The radical-radical combination lends this reaction a particularly deep energy well, creating a long-lived complex, up to the order of 1 s at the lowest temperature investigated, capable of producing dimethyl ether. This reaction also benefits from a high energy barrier in the exit bimolecular exit channel, which reduces k_2 to irrelevance. The radiative association rate coefficients, especially the canonical result, even approach the collisional rate coefficient at 10 K.

The quantitative discussion up to now has ignored the phenomenon of roaming. A roaming channel does appear to exist for this reaction (Tsang & Hampson, 1986; Sivaramakrishnan et al., 2011). The roaming pathway was tested at higher energies, equivalent to 251 K to 755 K, so that the smaller temperatures considered here require some extrapolation. However, the roaming pathway appears to be entirely first-order and increasing with temperature, and the rates for this process are quite small at low

temperatures. The first-order rate coefficient (s^{-1}) is given by the equation:

$$k_{2,\text{roaming}} = 2955.79E^{0.780}. \tag{3.12}$$

where E is the energy per kcal/mol which when multiplied by the pre-exponential constant gives s^{-1}.

Since roaming is a competitive pathway with radiative association, this rate coefficient is added into the denominator of Eq. (3.1). The effect of this addition, which has already been included within the results shown in Table 3.2, is minimal, though nonzero, simply because the rate for k_{-1} also rises and rises much more quickly with energy. Thus, although roaming can happen effectively at higher energies, a collision complex is still more likely to redissociate than to roam. As with the other constituent rate coefficients in Eq. 3.1, the roaming rate coefficients are calculated at a particular energy and then included in k_{ra} which is then integrated to an equivalent temperature. Using this process, Eq. 3.12 yields a roaming rate coefficient of 139 s^{-1} at 10 K, 488 s^{-1} at 50 K, 838 s^{-1} at 100 K, and 1980 s^{-1} at 300 K. At the same time, k_{-1} is on the order of 100 s^{-1} at 10 K, but 10^6 s^{-1} at 100 K, though the precise value is dependent on the J and E values being considered, as discussed above. The roaming channel has been included for every result in Table 3.2; it exceeds the more direct approach to products CH_4 and CH_2O.

To determine whether or not methyl-methoxy radical radiative association could enhance the calculated abundance of dimethyl ether sufficiently to explain its abundance in a number of sources, the newly calculated rate coefficients and previously reported estimates (Balucani et al., 2015; Vasyunin & Herbst, 2013b) were fitted to a modified

Table 3.3: Modified Arrhenius Rate Expressions for Methyl-Methoxy Radiative Association.

α **(cm^3 s^{-1})**	β	γ	**Reference**
1.37(-12)	-0.96	0.00	This work, Phase-space
1.70(-11)	-0.70	0.00	This work, Canonical
1.00(-15)	-3.00	0.00	Vasyunin & Herbst (2013b)
1.00(-14)	-3.00	0.00	Balucani et al. (2015)

Notes. a(b) indicates a $\times$ 10^b. These fits apply to the temperature range 10 K - 100 K.

Arrhenius equation:

$$k_{\rm ra} = \alpha(\frac{T}{300\ {\rm K}})^{\beta} \exp(-\gamma/T) \tag{3.13}$$

so that they could be included in the `NAUTILUS-1.1` chemical model (Ruaud et al., 2016). The fitted values are listed in Table 3.3, and represent the calculated rate coefficients from 10 to 100 K.

Previous work by Balucani et al. (2015) using an augmented version of the OSU2009 network indicates that raising the radiative association rate coefficient from the Vasyunin & Herbst (2013b) estimate of 3 $\times$ 10^{-11} cm^3 s^{-1} at 10 K by an order of magnitude increases the net production of dimethyl ether such that the radiative association can explain the abundance of dimethyl ether in L1544, a rather complex source. The rate coefficient used by Balucani et al. (2015) is very close to our canonical value at 10 K. Nevertheless, with the use of the `Nautilus` network at this temperature, we find that inclusion of either our canonical or phase space rate coefficient does not appreciably change the predicted abundance of dimethyl ether, showing that other mechanisms are more important.

3.4 Discussion

The result of both a phase space and a canonical calculation of the radiative association rate coefficient between the neutral methyl and methoxy radicals to form dimethyl ether shows that the reaction rate coefficient for these radicals can be quite high at low temperatures, as compared with other radiative association reactions in the NAUTILUS network (Ruaud et al., 2016). Though methyl has not yet been observed in cold regions, its abundance has been predicted (McGuire et al., 2017b). The methoxy radical has been seen toward the dark cloud B1-b at a derived fractional abundance with respect to total hydrogen of 4.67×10^{-12} (Cernicharo et al., 2012b). The fractional abundances of these radicals in the Nautilus model, for standard cold core conditions, lie in the 10^{-8} to 10^{-10} range at the relevant timescale for observation of dimethyl ether. Nevertheless, using the calculated abundances of the methyl and methoxy radicals even with the largest of the above reaction rate coefficients at 10 K we were not able to account fully for the observed abundance of dimethyl ether solely with formation by radiative association. The production of dimethyl ether by radiative association appears to be too slow at 10 K to explain fully the abundance of dimethyl ether, especially in cold sources with higher abundances such as TMC-1, unless other mechanisms can add to its synthetic power.

As shown in Figure 3.2, there is only a small difference in the peak-time abundances of dimethyl ether when we compare plots using the NAUTILUS network with the radiative association completely turned off ("RAoff"), with the phase space ("PS") value used, and with the larger canonical value used. In the TMC-1 models considered here, the radiative association reaction accounts for approximately one percent of the total dimethyl ether produced at peak time. Specifically, at the peak time, use of the canonical rate leads to a peak-time fractional abundance of 2.104×10^{-10} while use

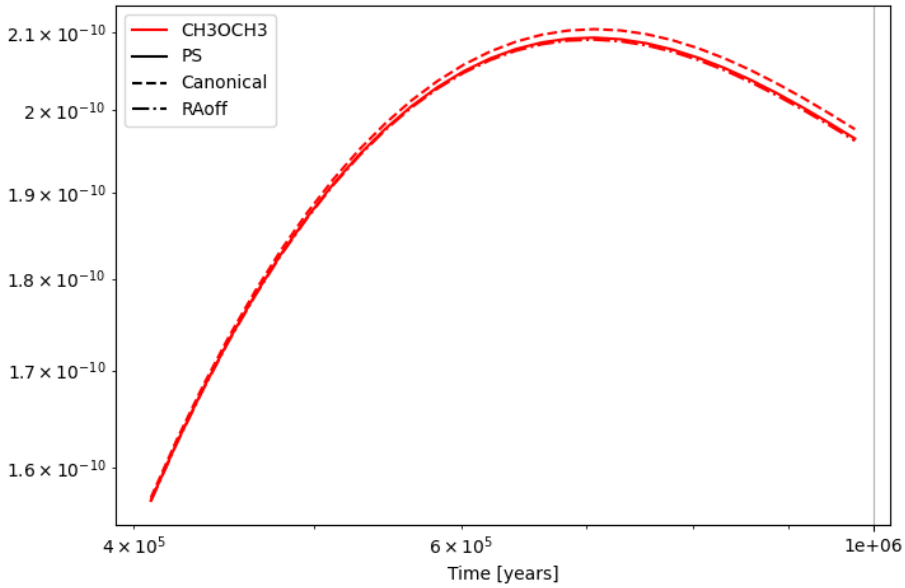

Figure 3.2: Gas-phase fractional abundances with respect to total hydrogen for dimethyl ether as a function of time using the Nautilus network under cold core conditions. Results are shown with the phase-space and canonical (thermal) theories developed for the rate of radiative association and for a model without the radiative association of dimethyl ether (RAoff). As noted above, the peak abundances here are in line with the observed abundance of dimethyl ether in TMC-1 and other prestellar cores.

of the phase-space rate leads to a peak-time fractional abundance of 2.093 $\times 10^{-10}$. These can be compared with a peak-time fractional abundance without the radiative association of 2.090 $\times 10^{-10}$. At 10 K, the phase-space calculation of the rate is about an order of magnitude slower than the canonical theory, but the difference in peak gas-phase fractional abundance of dimethyl ether between the theories considered in the paper is on the order of 10^{-12}, though the peak abundance is on the order 10^{-10} with or without the radiative association. Observational estimates of the fractional abundance of dimethyl ether in TMC-1, a standard cold core, range from 1.5 $\times 10^{-10}$ (Soma et al., 2018) to 2.5 $\times 10^{-10}$ (Agúndez et al., 2021) on the cyanopolyyne peak, meaning that the models considered here all fall within the range of the observations, although this agreement has little to do with the radiative association rate coefficients.

Instead, the two reactions that can account for the observed abundance of dimethyl ether are the reactive (chemical) desorption processes

$$CH_3(s) + CH_3O(s) \rightarrow CH_3OCH_3(g), \tag{3.14}$$

and

$$H(s) + CH_3OCH_2(s) \rightarrow CH_3OCH_3(g), \tag{3.15}$$

in which radicals on a grain surface combine and the exothermicity of the reactions subsequently allows desorption of the products from the grain into the gas phase at an assumed value of one percent.

Recently, Jin & Garrod (2020) have introduced an interesting potential mechanism, whereby a hydrogen atom reacts with a CH_2 radical on a grain surface, and the new CH_3 radical reacts instantaneously with a nearby CH_3O radical to form dimethyl ether, possibly significantly increasing the gas-phase abundance of dimethyl ether by chemical desorption. Similar other processess involving three bodies can play a role in the formation of other COMs. Radiative association may still play a role in the formation of COMs, especially since the catalog of such gas-phase reactions obtained by calculations between neutral radicals is currently incomplete. An alternative route for the production of CH_3OCH_3 could be the radiative association between CH_3^+ + CH_3OH giving $CH_3OHCH_3^+$ followed by the dissociative electron recombination of $CH_3OHCH_3^+$, although this dissociative recombination yields only the low fraction of 7% dimethyl ether (Hamberg et al., 2010). The reaction to form $CH_3OHCH_3^+$ competes with the transfer of H^- giving $H_2COH^+ + CH_4$ (Herbst, 1987). The calculated rate for the formation of $CH_3OHCH_3^+$ is not sufficient to explain the formation of

CH_3OCH_3 but great uncertainties exist on the precise value of this rate. Another interesting factor to consider is the recent work on radiolysis (Paulive et al., 2021). Radiolysis, the collective term for non-thermal processes by which molecules on and in grain mantles are ionized and excited by cosmic rays, can result in a temporary increase in the abundance of radicals on surfaces or in the gas-phase. This, then, can drive up production of COMs through other reaction pathways. As an understanding of the assorted mechanisms to form COMs under both cold and warm environments continues to grow, an increase in the the list of studied radiative association reactions between neutral species will prove valuable.

3.5 Addendum: Ethanol

The neutral radical CH_3O can collide with CH_3 in the opposite physical orientation; instead of forming a C−O−C backbone, these species might combine such that the carbon of CH_3O hits the carbon of CH_3 and forms a C−C−O backbone. The stable product of this reaction would be ethanol, CH_3CH_2OH, which would involve a hydrogen atom to shift from its initial position on the carbon of CH_3O to the oxygen. This rearrangement requires an input of energy of about 90 kcal mol^{-1} (Solly & Benson, 1969) to break the hydrogen-carbon bond, which is not trivial at the low temperatures of the cold, dark cloud considered here. Further, the three hydrogens surrounding the carbon atom on CH_3O make the carbon less sterically accessible than the exposed oxygen.

Nonetheless, assuming CH_3 and CH_3O begin randomly oriented with respect to one another, either face of the flat CH_3 radical may be approached by either the carbon or oxygen end of the CH_3O radical, and Sivaramakrishnan et al. (2011) find that

the approach by CH_3 to either end of the CH_3O is barrierless, though there is a transition state barrier. Therefore, to omit the possibility of the carbon-carbon bond production leaves the discussion of these two radicals and their interaction incomplete. We calculated the phase-space and thermal radiative association rate coefficients at various temperatures following §3.2 for

$$CH_3O + CH_3 \rightarrow CH_3CH_2OH + h\nu. \tag{3.16}$$

The parameters are calculated in §3.5.1, and the results are presented and discussed briefly in §3.5.2.

3.5.1 Molecular Dynamics

Here, we use Gaussian-09 (Frisch et al., 2009) to calculate the parameters relating to the radiative dissociation in Eq. 3.16. The M062X/aug-cc-pVtz level of theory is chosen to correlate with the CH_3OCH_3 calculations and the results are given in Table 3.4.

Table 3.4: Parameters for radiative association between CH_3O and CH_3 to form CH_3CH_2OH.

Species	**Parameter**
	Electronic Degeneracy
CH_3CH_2OH	1
	Total Energy at 0 K (kcal mol^{-1})
CH_3CH_2OH	53.214
	Well Depth (kcal mol^{-1})
Collision Complex	87.3
	Rotational Constant (cm^{-1})[a]
CH_3CH_2OH	0.467

Vibrational Modes (cm^{-1})	
CH_3CH_2OH	233.6882, 291.3085, 422.6133, 820.2267, 918.2885, 1054.3047, 1136.6769, 1183.0641, 1273.6257, 1305.9915, 1401.8367, 1457.6488, 1485.4467, 1503.3021, 1533.5303, 3024.0134, 3055.4323, 3057.1394, 3135.3467, 3136.1082, 3904.2754
$CH_3CH_2OH^{\#}$	2194.8690i[b], 228.1016, 440.8475, 623.6658, 857.8252, 907.8282, 963.5527, 1044.8103, 1153.4000, 1273.1488, 1369.1394, 1395.4150, 1446.3912, 1470.7071, 1493.0858, 2011.2438, 2247.9821, 3019.1125, 3053.4238, 3131.4990, 3160.9529
Radiative Intensity (km mol^{-1})	
CH_3CH_2OH	21.8267, 97.6595, 10.6391, 0.1337, 8.6948, 41.2492, 44.8087, 3.9257, 76.9302, 0.0102, 1.6998, 13.0621, 5.8951, 2.4865, 1.7432, 54.5795, 34.5150, 11.8987, 21.5888, 19.4617, 43.3712

[a] Ethanol is treated as a spherical top using the geometric mean.
[b] This imaginary frequency is used only in the calculation of the tunneling rate under the transition state barrier leading from the complex to the competitive exit channel. The transition state is labeled with the # sign.

3.5.2 Results and Discussion

Following §3.2, we calculated the phase-space rate coefficient for the radiative association between CH_3O and CH_3. The results of these calculations are given in Table 3.5.

These results are close to the results of CH_3OCH_3, which is to be expected (Tennis et al., 2021). That the CH_3CH_2OH rate coefficients exceed those for CH_3OCH_3 is likely due to the lack of a known roaming channel and the higher value of D_0. The latter allows the collision complex to dwell in a deeper energy well, which corresponds to a higher density of states ρ_ν, and thereby lessens the rate coeffiecient of re-dissociation, k_{-1}. See Eqs. 3.7 and 3.8.

Since the rate coefficient for radiative association leading to CH_3CH_2OH is comparable to the rate coefficient for radiative association leading to CH_3OCH_3, there is no reason

Table 3.5: Radiative association rate coefficients for CH_3O and CH_3 leading to CH_3CH_2OH.

Temperature (K)	**Phase-space k_{ra} (cm^3 s^{-1})**
10	6.09(-11)
20	4.85(-11)
30	4.09(-11)
40	3.53(-11)
70	1.64(-11)
100	9.54(-12)
150	3.99(-12)
200	2.21(-12)
250	1.85(-12)
300	1.59(-12)

Notes. a(b) indicates a x 10^b.

to imagine that the abundance of CH_3CH_2OH would be increased significantly by this mechanism in a chemical kinetic model where CH_3OCH_3 was not. Instead, Paulive et al. (2022) show that sputtering by cosmic rays can help the modeled abundance match the observed abundance of 1.1×10^{-10} (Agúndez et al., 2023) at the estimated age of TMC-1, 5×10^5 years.

Chapter 4

Detection and Modeling of CH_3NC in TMC-1

Two closely related isomeric pairs of cyanides, CH_3[CN/NC] and H_2C[CN/NC], are studied in cold, dark interstellar cloud conditions. In contrast to the diverse detections of methyl cyanide (CH_3CN) in space, methyl isocyanide (CH_3NC) has previously only been observed in warm and hot star-forming regions. Efforts to model these molecules with the three-phase gas-grain code `Nautilus` *in TMC-1 conditions overproduce both CH_3CN and CH_3NC, though the ratio of ∼5.9% is consistent across observations and models of these species. This may point to missing destruction routes in the model. The models capture the larger abundance of H_2CCN well. Dissociative recombination is found to be the primary production route for these molecules, and reactions with abundant ions are found to be the primary destruction routes. H + CH_3NC is investigated with transition state theory as a potential destruction route, but found to be too slow in cold cloud conditions to account for the discrepancy in modeled and observed abundances of CH_3NC.*[1]

[1]Originally published as part of Tennis et al. (2023). Observations by C. Xue. Quantum chemical calculations by D. Talbi, except for those in §4.5 by J. D. Tennis. Models and discussion by J. D. Tennis.

4.1 Introduction

One of the very first molecules to be detected in interstellar space was hydrogen cyanide (HCN), followed the next year by hydrogen isocyanide (HNC) (Snyder & Buhl, 1971, 1972). Since then, cyanides and isocyanides have been detected in diverse interstellar environments (McGuire, 2022, and references therein), and the ratio of isocyanides to their cyanide isomers has been the topic of much investigation (e.g. Irvine & Schloerb, 1984; Graninger et al., 2015; Willis et al., 2020; Xue et al., 2020). A cyanide is any molecule with a terminal -CN group, and an isocyanide is any molecule with a terminal -NC group. As Remijan et al. (2005) points out, however, the interstellar medium is too cold for unimolecular interconversion between cyanides and isocyanides, so the ratio reflects differences in the formation and destruction processes for each rather than the ratio of thermodynamic stabilities.

For the HCN/HNC case, for example, Graninger et al. (2014) find that reaction kinetics explain the observed ratio in the giant molecular cloud Orion Molecular Cloud-1 (OMC-1). The HNC:HCN ratio is 1:80 at the core of OMC-1 and grows to unity at the coldest, outermost edges (Schilke et al., 1992) because in this latter temperature regime dissociative recombination, the gas-phase reaction between a positive ion and an electron to form two or more neutral fragments, produces nearly equal amounts of the two isomers, as shown:

$$\mathrm{HCNH^+ + e^- \rightarrow HCN/HNC + H.} \tag{4.1}$$

The ratio is lower at the core of OMC-1 than at its edge due to the reaction

$$\mathrm{H + HNC \rightarrow H + HCN,} \tag{4.2}$$

which destroys HNC in favor of HCN. Reaction 4.2 has an energy barrier which makes this reaction more efficient at higher temperatures, and therefore allows the abundance of the product HCN to be higher at higher temperatures as compared to the reactant HNC (Graninger et al., 2014).

CH_3CN has been seen in almost every type of interstellar environment (Cernicharo et al., 1988; Purcell et al., 2006; Ginard et al., 2012; Gratier et al., 2013), but its isomer CH_3NC, 9486 cm^{-1} higher in energy (Remijan et al., 2005), has only been detected in molecular hot cores and photodissociation regions (Willis et al., 2020; Gratier et al., 2013). CH_3NC is difficult to detect because it is less abundant, as we show. CH_3CN and CH_3NC are also mainly produced by the dissociative recombination mechanism. We investigate the barrier height of the analogous

$$H + CH_3NC \rightarrow HCN + CH_3 \tag{4.3}$$

reaction to assess the viability of these isomers as a tracer of kinetic gas temperatures, and test the effects of this reaction on their abundances in kinetic models.

Here, we detail efforts to model the abundance of CH_3NC, CH_3CN, H_2CCN, and H_2CNC in cold, dark cloud conditions in Section 4.2. We discuss those results in Section 4.3 before reaching our conclusions in Section 4.4.

4.2 Astrochemical Model

In this work, we use `Nautilus` (version 1.1) (Ruaud et al., 2016) to model the abundances of chemical species in the cold, dark cloud conditions appropriate to TMC-1, including a visual extinction A_v of 10, a temperature of 10 K, and a cosmic-ray ioni-

sation rate ζ of 1.3×10^{-17} (see, for example, Wakelam & Herbst (2008b)); following Hincelin et al. (2011) and Loomis et al. (2021) the age of TMC-1 is taken to be $\sim 5 \times 10^5$ years.

`Nautilus` is a three-phase rate equation model, our version of which includes the rates of 7981 gas-phase reactions and 8034 grain reactions involving 549 gas-phase and 1017 grain-surface and bulk species to compute abundances of species over time, beginning with atoms for all elements except hydrogen, which is dominated by H_2. We added two new species, CH_3NC and CH_2CHNC, as well as the precursor radicals and cations that lead to their formation.

A list of the reactions added is available in Appendix A.2. This table includes the H+CH_3NC reaction, the other gas-phase reactions relevant to CH_3NC, H_2CCN, H_2CNC, and the surface neutral-neutral reactions these species. The standard adsorption, desorption, and mixing of molecules exchanging between the topmost surface layers of ice and the bulk layers below are also included in the reaction network, though the table does not note these. Also omitted from the table are the grain-surface photodestruction reactions. These reactions represent our effort to include CH_3NC in `Nautilus` accurately, with precursor radicals and other potential products from these radicals such as C_2H_3[CN/NC] and C_2H_5[CN/NC], as shown in Table A.4. The dominant production and destruction reactions for CH_3CN, CH_3NC, H_2CCN, and H_2CNC are gas-phase in our models.

The resulting CH_3NC abundance with respect to hydrogen under TMC-1 conditions at $\sim 5 \times 10^5$ years is 2.48×10^{-10}, which is about 5% of the CH_3CN abundance, 5.05×10^{-9}. The resulting H_2CCN abundance is 4.92×10^{-9}, and the resulting H_2CNC abundance is 3.64×10^{-9}.

4.2.1 Radiative Association

Because CH_3CNH^+ and CH_3NCH^+ precede the main production mechanism for the species of interest, it is helpful to consider their production. These ions come from the four related gas-phase radiative association reactions of HCN or HNC with CH_3^+:

$$HCN + CH_3^+ \rightarrow CH_3NCH^+ + h\nu, \tag{4.4}$$

$$HNC + CH_3^+ \rightarrow CH_3CNH^+ + h\nu, \tag{4.5}$$

$$HCN + CH_3^+ \rightarrow CH_3CNH^+ + h\nu, \tag{4.6}$$

and

$$HNC + CH_3^+ \rightarrow CH_3NCH^+ + h\nu. \tag{4.7}$$

The abundance of reactant HCN in TMC-1 in our model is 5.0×10^{-8} with respect to hydrogen at $\sim 5 \times 10^5$ years, in agreement with the observations of Irvine & Schloerb (1984), who find an abundance of 5.0×10^{-8} to 5.0×10^{-9}. The abundance of reactant HNC in our models is 4.8×10^{-8} with respect to hydrogen at the same time, in line with a near-unity HNC:HCN ratio (Irvine & Schloerb, 1984; Loison et al., 2014). The abundance of CH_3^+ in our model is 1.5×10^{-11}. This set of reactions was studied by Defrees et al. (1985), who found that its two products, CH_3CNH^+ and CH_3NCH^+, are formed in a ratio of 85:15 due to unimolecular isomerization. Later, Anicich et al. (1995) examined the experimental literature on these reactions and determined a total radiative association rate coefficient of 2×10^{-10} cm^3s^{-1} for Reactions 4.4 and 4.6.

Although the rate coefficients of $1.7 \times 10^{-10}(T/300K)^{-3}$ for Reactions 4.4 and 4.5,

and $3.0 \times 10^{-11}(T/300K)^{-3}$ for Reactions 4.6 and 4.7 from Anicich et al. (1995) and Defrees et al. (1985) are used throughout this work, we tested the effects of lowering the rate coefficients, as shown in Figures 4.1 and 4.2.

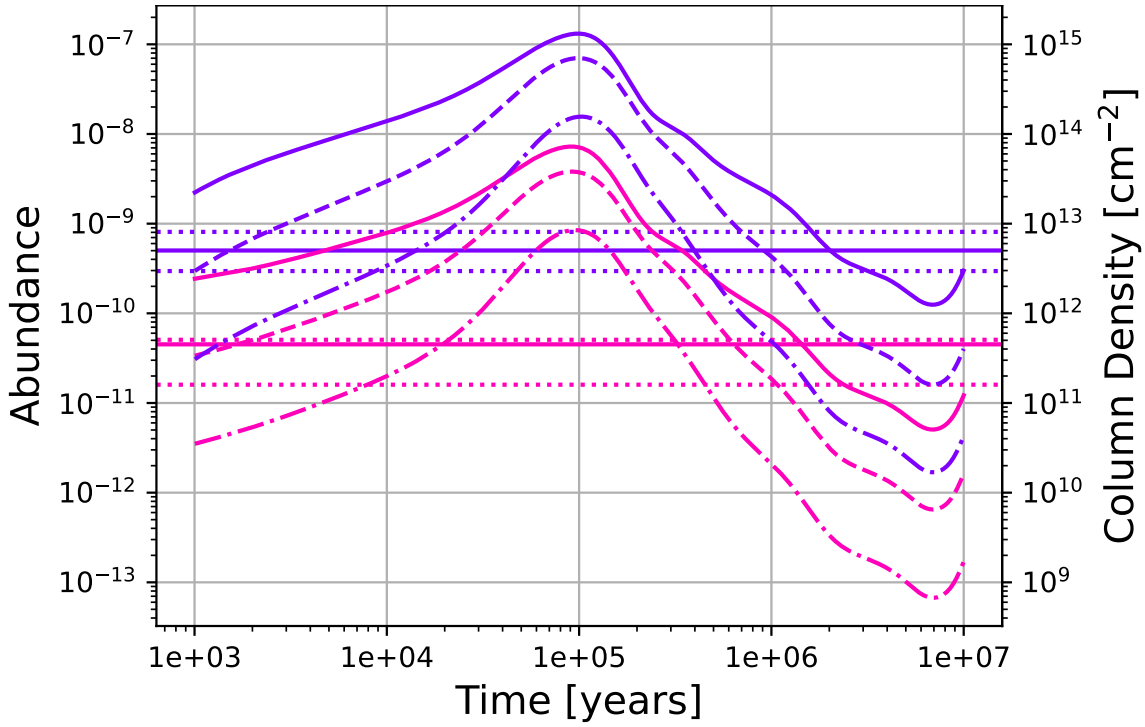

Figure 4.1: Modeled abundances/column densities of CH_3CN and CH_3NC over time. The solid curves represent the abundances modeled with standard reaction rate coefficients, the dashed curves represent the abundances modeled with rate coefficients corresponding to Reactions 4.4 - 4.7 lowered by one order of magnitude, and the dash-dotted curves represent the abundances modeled with these rate coefficients lowered by two orders of magnitude. The solid horizontal lines represent observed abundances/column densities and the dotted lines represent the uncertainties on these values. Purple represents CH_3CN and pink represents CH_3NC.

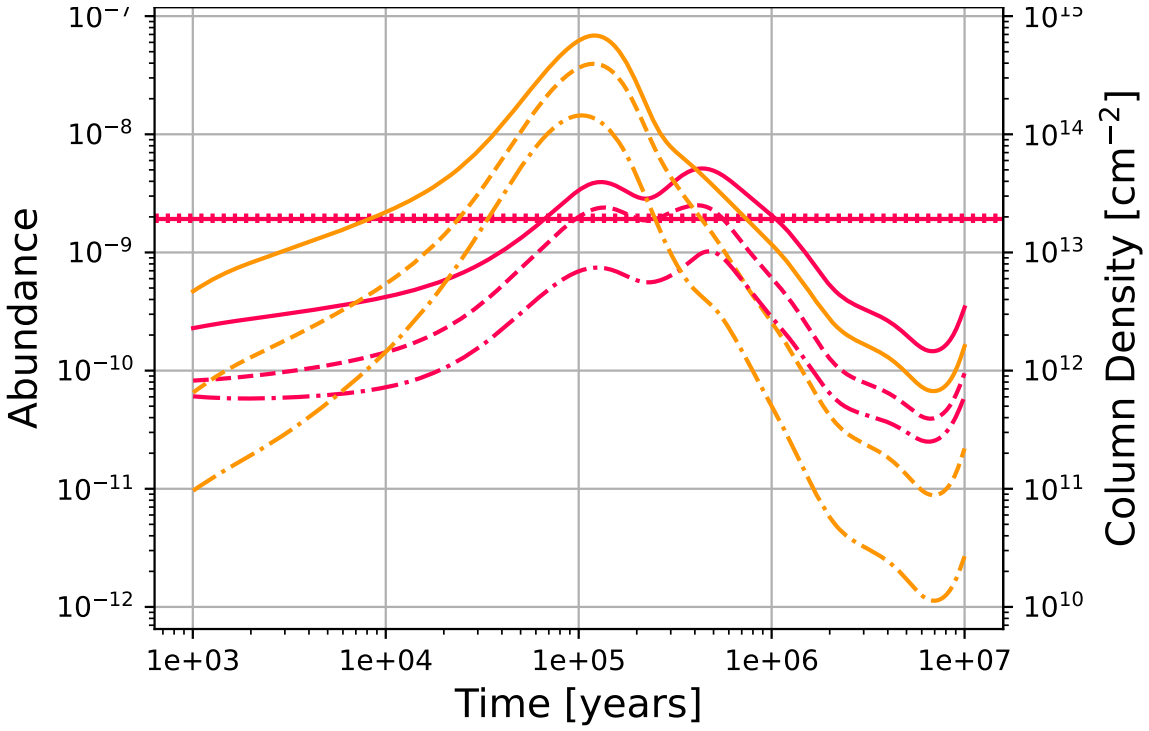

Figure 4.2: Modeled abundances/column densities of H_2CCN and H_2CNC over time. The solid curves represent the abundances modeled with standard reaction rate coefficients, the dashed curves represent the abundances modeled with rate coefficients corresponding to Reactions 4.4 - 4.7 lowered by one order of magnitude, and the dash-dotted curves represent the abundances modeled with these rate coefficients lowered by two orders of magnitude. The solid horizontal lines represent observed abundances/column densities and the dotted lines represent the uncertainties on these values. Red represents H_2CCN and orange represents H_2CNC.

At $\sim 5\times10^5$ years (Hincelin et al., 2011; Loomis et al., 2021), Figure 4.1 shows that the observed abundances of CH_3CN and CH_3NC match the modeled abundance when the rate coefficients for this set of reactions (Reactions 4.4 - 4.7) in TMC-1 conditions are between one and two orders of magnitude lower than previously modeled. Figure 4.2, similarly, shows that the modeled abundance of H_2CCN more closely matches the observed abundance of H_2CCN when the rate coefficients for this set of reactions is between one and two orders of magnitude lower than previously modeled. Further, detailed study of Reactions 4.4 - 4.7 is necessary to further constrain the true rate

coefficients. All models of various precursor production efficiencies indicate the same CH_3NC:CH_3CN ratio. The modeled abundance ratio of H_2CNC:H_2CCN falls from 74% to 34% with the tested decrease in rate coefficients for Reactions 4.4 - 4.7, but the modeled H_2CNC:H_2CCN ratio is in all cases higher than the observed H_2CNC:H_2CCN ratio of <2%.

4.2.2 Dissociative Recombination

The molecules CH_3CN and CH_3NC are both predominantly formed by dissociative recombination of their protonated forms:

$$CH_3CNH^+ + e^- \rightarrow CH_3CN + H \tag{4.8}$$

and

$$CH_3NCH^+ + e^- \rightarrow CH_3NC + H \tag{4.9}$$

though about 15% of the modeled CH_3NC is formed from dissociative recombination of CH_3CNH^+ (Defrees et al., 1985, see later discussion of branching ratios), as the model also includes

$$CH_3CNH^+ + e^- \rightarrow CH_3NC + H \tag{4.10}$$

and

$$CH_3NCH^+ + e^- \rightarrow CH_3CN + H. \tag{4.11}$$

Like radiative association, dissociative recombination is a gas-phase process. Our modeled abundance of electrons is 1.2×10^{-8} at $\sim 5 \times 10^5$ years, in agreement with common estimates of the electron abundance of TMC-1 such as those of Lee et al. (1996).

As with CH_3CN and CH_3NC, dissociative recombination reactions are also a key production route for the H_2CCN and H_2CNC radicals with one extra hydrogen-carbon bond breaking:

$$CH_3CNH^+ + e^- \rightarrow H_2CCN + 2H, \tag{4.12}$$

$$CH_3NCH^+ + e^- \rightarrow H_2CNC + 2H, \tag{4.13}$$

$$CH_3CNH^+ + e^- \rightarrow H_2CNC + 2H, \tag{4.14}$$

and

$$CH_3NCH^+ + e^- \rightarrow H_2CCN + 2H. \tag{4.15}$$

Another set of possibilities for dissociative recombination involves the cleaving of heavy atoms in the backbone, as in:

$$CH_3CNH^+ + e^- \rightarrow HNC + CH_3, \tag{4.16}$$

$$CH_3NCH^+ + e^- \rightarrow HCN + CH_3, \tag{4.17}$$

$$CH_3CNH^+ + e^- \rightarrow HCN + CH_3, \tag{4.18}$$

and

$$CH_3NCH^+ + e^- \rightarrow HNC + CH_3. \tag{4.19}$$

The isocyanide-to-cyanide ratios for the pairs of molecules considered here are set in part by the dissociative recombination reactions above. (Another major factor in setting this ratio is destruction; see Section 4.2.3). To determine the rate coefficients of Reactions 4.8 - 4.19, we rely on the insights gained from the research in Table 4.1.

Table 4.1: Findings of previous theoretical and experimental work used to determine appropriate rate coefficients for Reactions 4.8 - 4.19

Citation	**Contribution(s)**
Defrees et al. (1985)	15% of CH_3CNH^+ collision complexes isomerise to CH_3NCH^+. Here, we assume 15% is the total of all reactions that require isomerization from a specific precursor, CH_3CNH^+ or CH_3NCH^+.
Plessis et al. (2010)	The branching ratio of a given product channel is not always correlated to its heat of formation. Rather than an energy-based weighting, we test multiple branching ratios for Reactions 4.8-4.19.
Vigren et al. (2008)	(1) One bond between heavy atoms of deuterated CH_3CNH^+ breaks in 35% of the dissociative recombinations (as in Reactions 4.16 - 4.19), whereas the C-C-N backbone is preserved 65% of the time (as in Reactions 4.8 - 4.15). (2) The total of the dissociative recombination rate coefficients (Reactions 4.8 - 4.19) is $\alpha = 8.13 \times 10^{-7}(T/300\,\mathrm{K})^{-0.69}\mathrm{cm}^3\,\mathrm{s}^{-1}$.
Loison et al. (2014)	If the C-C-N or C-N-C backbone is preserved, two hydrogen atoms dissociate 38% of the time (as in Reactions 4.12 - 4.15), and the remaining 62% of the time one hydrogen atom dissociates (as in Reactions 4.8 - 4.11).

To examine the relative abundances of the molecules of interest, we ran three models, "low isomerization," "standard isomerization," and "high isomerization." The model with "standard isomerization" uses exactly the information in Table 4.1, while "low isomerization" only allows for half of the rearrangements of the "standard" model. For example, the rate coefficient for Reaction 4.10, which requires isomerization, is cut in half. The "high isomerization" model doubles the reaction rate coefficient for reactions that require isomerization. The results of these models are given in Table 4.2 and Figure 4.3.

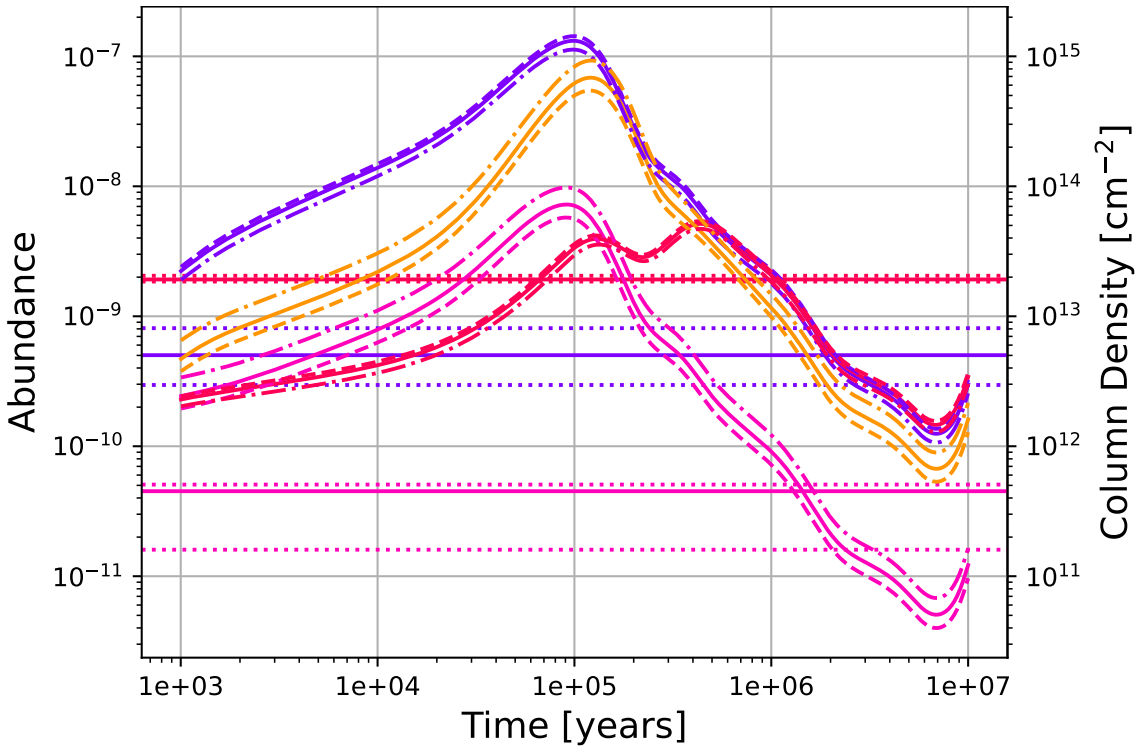

Figure 4.3: Abundances/column densities of species of interest from models of TMC-1 with differing branching ratios for dissociative recombination of CH_3CNH^+ and CH_3NCH^+. The solid horizontal lines represent observed abundances/column densities and the dotted horizontal lines represent uncertainties on these values. The solid curve represents the model with "standard isomerization." The dashed curves come from "low isomerization" models and the dash-dotted curves come from "high isomerization" models; see text for further model details. Purple represents CH_3CN, pink represents CH_3NC, red represents H_2CCN, and orange represents H_2CNC.

Table 4.2: The abundances at $\sim 5 \times 10^5$ years. of molecules of interest for branching ratios on the dissociatve recombination pathways for CH_3CNH^+ and CH_3NCH^+. See text for description of models.

Molecule	Low Iso. Abundance	Standard Iso. Abundance	High Iso. Abundance
CH_3CN	5.50(−9)	5.05(−9)	4.35(−9)
CH_3NC	1.91(−10)	2.48(−10)	3.29(−10)
H_2CCN	5.16(−9)	4.92(−9)	4.51(−9)
H_2CNC	3.17(−9)	3.64(−9)	4.46(−9)
HCN	6.27(−8)	6.23(−8)	6.16(−8)
HNC	4.79(−8)	4.83(−8)	4.91(−8)

Notes. $a(b)$ refers to an abundance with respect to hydrogen of $a \times 10^b$.

Increasing the branching ratio for a species does increase the abundance of that species as expected. The amount of the species of interest that comes from dissociative recombination does not change significantly in any of the models; it is the dominant production mechanism for CH_3CN, CH_3NC, H_2CCN, and H_2CNC, in all of our models and the case of 15% isomerization remains our standard. This is supported by the CH_3NC:CH_3CN ratio, which is observed to be 5.9% and which is 3% for the "Low isomerization" case, 5% for the "Standard isomerization" case, and 8% for the "High isomerization" case. The HNC:HCN ratio is observed (Loison et al., 2014) to be close to or slightly less than one, which all three of these cases support.

4.2.3 Destruction Methods

One destructive reaction of particular interest is the destruction of CH_3NC by reaction with an H atom in the gas phase. Since hydrogen is highly abundant, an efficient reaction between these would likely be the dominant destruction process of CH_3NC. The abundance of H atoms is 3.1×10^{-5} in our models, on the same order of magnitude as the initial abundance of H atoms since most hydrogen is assumed to be in H_2, which

does not react with CH_3NC. Additionally, this reaction could set the CH_3CN:CH_3NC ratio in a manner analogous to Reaction 4.2 for HCN:HNC. Willis et al. (2020) notes that varying the barrier height of this reaction alone changes the abundance of CH_3NC at late times dramatically in their models. As explained in Tennis et al. (2023), the barrier height for the H+CH_3NC reaction is found to be 2.191 kcal/mol (1102 K), much too high to be a significant destruction pathway in TMC-1 or to set the CH_3CN:CH_3NC ratio, though it may play a role in warmer regions.

Using transition state theory and the parameters found with the methods described in Tennis et al. (2023) to calculate the H + CH_3NC reaction rate coefficient in Table A.4, we included this reaction in our `Nautilus` model of TMC-1; this method is explained in Woon et al. (2021). In our model this reaction cannot explain the destruction of CH_3NC. Instead, CH_3NC is primarily destroyed by reaction with abundant ions. The rates of reaction between CH_3NC and the common interstellar ions H_3^+, C^+, HCO^+, H_3O^+, $HOCO^+$, and H^+ were calculated following the method described by Woon & Herbst (2009b); H_3^+ and C^+ were found to be the most effective in destroying CH_3NC in total reactive flux. The same method was used to calculate reaction rates between CH_3CN, H_2CCN, and H_2CNC and common interstellar ions and these reactions, too, were found to be the dominant destruction mechanism for these species in our models.

4.2.4 Temperature Effects

TMC-1 has extremely low rotational and excitation temperatures (T_{ex}), generally in the range 5–10 K. Models of TMC-1 typically assume T_{gas}=T_{dust}=10 K (Hincelin et al., 2011; McGuire et al., 2020). The 10 K model produced here is the closest to physical conditions in TMC-1, but for comparison to other regions in the ISM we con-

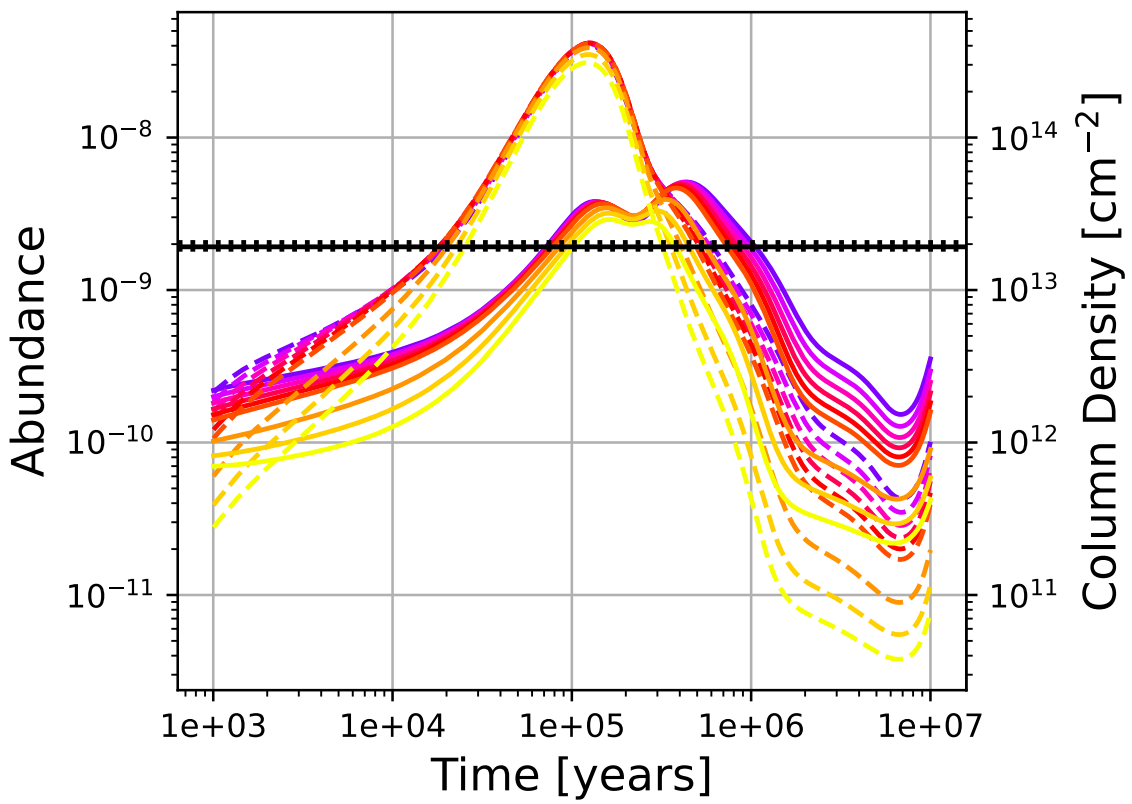

Figure 4.4: A comparison of the abundances of H_2CCN (solid) and H_2CNC (dashed) from models with temperatures of 10 K to 30 K, moving from purple to yellow as temperature increases. The solid black line represents the observed abundance/column density of H_2CCN, and the dotted black lines represent the uncertainty on this value.

sidered warmer models as well. Since the main production route for CH_3CN, CH_3NC, H_2CCN, and H_2CNC is dissociative recombination, which is a weakly temperature-dependent process (going as $T^{-0.5}$), the destruction routes should be more increased by temperature than production routes, and indeed, the models show a slight decrease in the abundances of the molecules at the highest temperature studied (30 K). At this temperature, the molecules and their destructive collision partners collide more often and bring down the population of CH_3CN, CH_3NC, H_2CCN, and H_2CNC, though the effect is small, as can be seen in Figure 4.4 and Figure 4.5.

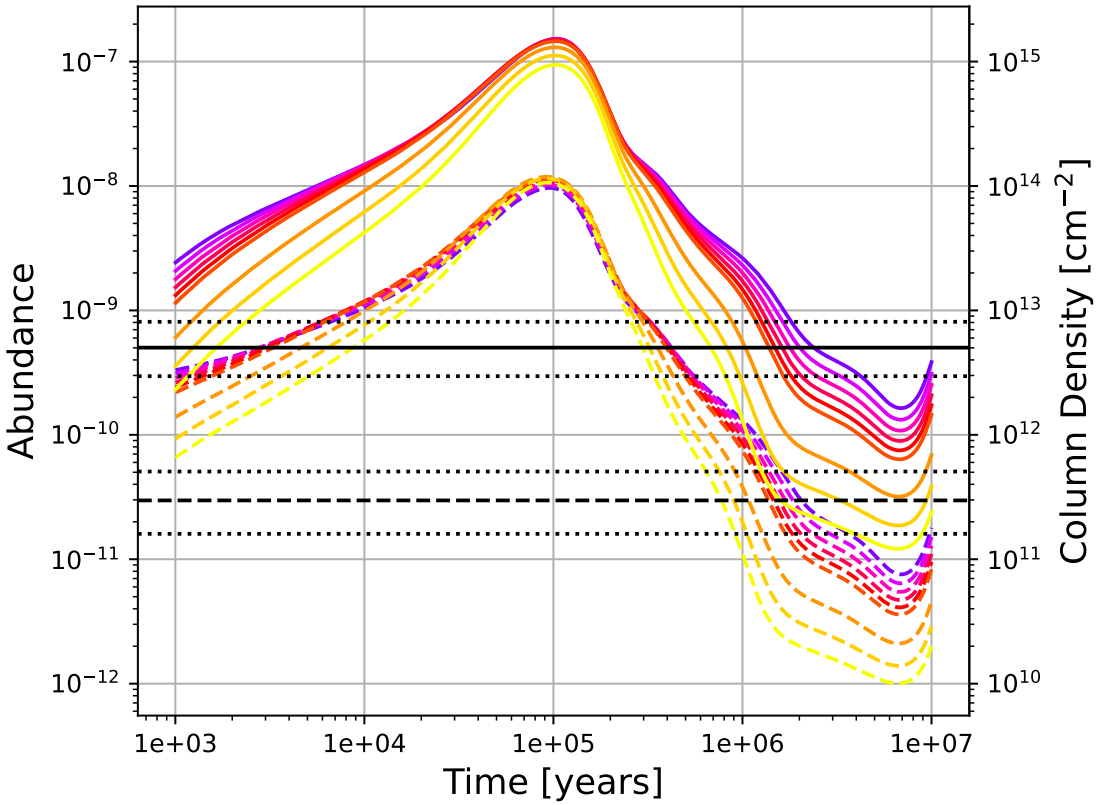

Figure 4.5: A comparison of the abundances of CH_3CN (solid) and CH_3NC (dashed) from models with temperatures of 10 K to 30 K, moving from purple to yellow as temperature increases. Observed abundances/column densities are represented in black, and the dotted black lines represent uncertainties on these values.

4.3 Discussion

Other cyanides are found under TMC-1 conditions and are helpful in constraining the chemistry of the models. For example, the HNC/HCN ratio is known to be around unity to within a factor of two (Loison et al., 2014) which our models confirm; we find abundances under TMC-1 conditions of 6.2×10^{-8} and 4.8×10^{-8} with respect to hydrogen for HCN and HNC, respectively, at $\sim 5 \times 10^5$ years.

The overproduction of CH_3CN and CH_3NC, and to a lesser extent of H_2CCN and H_2CNC, in our models compared with their observed abundances could indicate the existence of an effective destruction mechanism in TMC-1 for these species not included in our models, or that the present rate of the production mechanism is overestimated. Our modeled CH_3NC:CH_3CN abundance ratio, 5%, closely reproduces the observed column density ratio, $5.9^{+11.2}_{-3.9}$%, within error bounds. Calcutt et al. (2018) find an opposite result in modeling the solar-type protostars IRAS 16293-2422 A and B, for which modeled isocyanide-to-cyanide ratios are higher than that which is observed. In both models, an effective destruction mechanism that differentiates between CH_3CN and CH_3NC would help close the gap between modeled and observed abundances. One particularly interesting set of reactions along these lines is that studied by Nguyen et al. (2019), who find that on grain surfaces, CH_3NC has a significantly higher barrier to successive hydrogenation into CH_3NHCH_3 than CH_3CN does to $CH_3CH_2NH_2$. An additional mechanism for study might be dissociative electron attachment, whereby an electron attaches to a neutral molecule, forming an anion that dissociates into two or more fragments. Luxford & Nag (2021) find that the dissociative electron attachment pathways for CH_3CN and CH_3NC, while largely similar, diverge such that CH_3CN more readily splits into an H atom and H_2CCN^- than CH_3NC does an H atom and H_2CNC^-. These reaction pathways remain to be

studied in chemical kinetic models to the best of our knowledge.

4.4 Conclusions

Though the backbone is only one one carbon longer than HCN and HNC, the observed ratio of CH_3NC:CH_3CN is about 6%, compared to the near parity found between HCN and HNC. The modeled ratio of H_2CNC:H_2CCN is highly time dependent. Though many reaction pathways were investigated (see Table A.4), the dominant production route for CH_3CN, CH_3NC, H_2CCN, and H_2CNC in our models is the dissociative recombination of CH_3CNH^+ and CH_3NCH^+, and the dominant destruction route for these four molecules in our models is reaction with abundant ions such as H^+, H_3^+, and C^+. Why isocyanide-to-cyanide ratios are so different remains to be seen, and investigations as to the observed abundance of H_2CNC (as yet undetected) would be helpful in constraining gas-phase chemistry in TMC-1, which remains a fascinating area for inquiry.

4.5 Addendum: Destruction Mechanisms

The overproduction by our `Nautilus` models as compared to observations of CH_3CN and CH_3NC and, to a lesser extent, H_2CCN, could be due to missing destruction routes for these molecules. We outlined some of these in §4.3, and we explore them in more detail below. We find in general that the highlighted destruction routes are unable to account for the overproduction of CH_3CN, CH_3NC, H_2CCN, and H_2CNC, adding credence to the theory that the radiative association/dissociative recombination production mechanism may be overestimated.

4.5.1 Electron Attachment

An interesting possibility is the destruction of CH_3CN and CH_3NC through reaction with electrons, as suggested by Luxford & Nag (2021). Since electrons, like hydrogen atoms, are present in TMC-1 at relatively high abundances (about 10^{-8} with respect to hydrogen), an exothermic reaction with electrons would likely be an effective destruction mechanism. As Luxford & Nag (2021) show, however, the process of dissociative electron attachment, whereby the energy from the collision of an electron with CH_3CN or CH_3NC splits the reactant molecule apart, is slightly endothermic and therefore all but impossible in the cold interstellar medium. This is to say, the addition of the electron to the molecule is not strong enough to account for the breaking of the bond required to destroy the CH_3CN^- or CH_3NC^-.

Instead, excess energy of the collision complex formed by the attachment of a free electron with a molecule could be radiated away. This radiative electron attachment process would be highly analogous to radiative association between molecules, explored extensively in Chapter 3. The overall rate for radiative electron attachment, k_{att}, is given by

$$k_{\rm att}(j) = \frac{k_1(j)k_{\rm r}(j)}{k_{-1}(j) + k_{\rm r}(j)} \tag{4.20}$$

where j indicates that, since the reaction involves a free electron, selection rules apply, k_1 is the rate of formation of collision complex between the electron and the molecule, k_r is the radiative rate, and k_{-1} is the dissociation rate for the complex, analogous to Eq. 3.1.

Herbst & Osamura (2008) give separate methods for estimating and calculating the

radiative electron attachment rates. To estimate the rate, we use

$$k_1 = 4.982x10^{-7}G[T(K)/300]^{-0.5} \qquad cm^3s^{-1} \qquad (4.21a)$$

$$k_\mathrm{r} = 10^2 \qquad s^{-1} \qquad (4.21b)$$

$$k_{-1} = c/\rho \qquad s^{-1} \qquad (4.21c)$$

where G is the electronic degeneracy, T is temperature in Kelvin, c is the speed of light, and ρ is the density of vibrational states at an energy equal to that of the electron affinity. For a more precise rate, we use

$$k_1 = \frac{Gh^2}{2\pi\mu k_\mathrm{b}T}\sqrt{(2k_\mathrm{b}/\mu)} \qquad cm^3s^{-1} \qquad (4.22a)$$

$$k_\mathrm{r} = \frac{E_\mathrm{vib}}{s}\sum_{i=1}^{s}\frac{A^{(i)}_{1\rightarrow 0}}{h\nu_i} \qquad s^{-1} \qquad (4.22b)$$

in which $\mathrm{k_1}$ is the cross section for collision multiplied by the collisional speed and $\mathrm{k_r}$ is the emission rate for the complex with the assumption that a single photon coming from a system of harmonic oscillators will stabilize the complex (Herbst, 1982). Here, h is Planck's constant, $\mathrm{k_b}$ is the Boltzmann constant, μ is the reduced mass of the system, $\mathrm{E_{vib}}$ is the energy of the system which is assumed to be equal to the electron affinity, $A^{(i)}_{1\rightarrow 0}$ is the Einstein A coefficient for the fundamental transition of mode i, and ν_i is the vibrational frequency of that mode. Table 4.3 gives the parameters for these calculations.

Table 4.3: The parameters used for the calculation of radiative electron attachment rates.

Species	Parameter Value	Reference
	Electron Affinity [eV]	
CH_3CN	0.224	a,b
CH_3NC	0.254	b,c
	Vibrational Modes [cm^{-1}]	
CH_3CN^-	2888, 2268, 1347, 881, 2942, 2942, 1396, 1396, 1008, 1008, 345, 345	a,b
CH_3NC^-	253.26, 253.88, 918.54, 1132.77 1133.79, 1438.29, 1464.16, 1465.55, 2240.34, 2992.05, 3063.34, 3063.59	b,c
	Radiative Intensities [km/mol]	
CH_3CN^-	87.312, 14.419, 473.384, 36.898, 1031.785, 1031.785, 1218.595, 1218.595, 83.576, 83.576, 2.007, 2.007	a,b
CH_3NC^-	86.9502, 87.2342, 6.4229, 33.7724 34.3015, 476.8644, 419.8473, 426.9931, 50.5595, 122.7606, 521.4853, 525.1904	b,c

[a] Johnson (1999)
[b] Energy calculated at B3LYP/aug-cc-pVTZ
[c] This work

The resultant rate for radiative electron attachment to CH_3CN with approximations at 10 K is 4.952×10^{-15} cm^3s^{-1}; the overall rate coefficient is $k_{att} = 9.041 \times 10^{-16}$ $(T/300\ K)^{-0.5}$ cm^3s^{-1}. Without the approximations, the rate at 10 K is 3.505×10^{-14} cm^3s^{-1} and the overall rate coefficient is $k_{att} = 6.399 \times 10^{-15}(T/300K)^{-0.5}$ cm^3s^{-1}. The rate coefficients are too small for radiative electron attachment to be an influential destruction route for CH_3CN, primarily because the electron affinity of the species of interest here is much smaller than those in Herbst & Osamura (2008), which leads to much higher dissociation rates (k_{-1}; analogous to Eq. 3.7).

The electron affinities of those carbon chains are about one order of magnitude higher than that of CH_3CN; as a matter of interest, if CH_3CN had an electron affinity exactly one order of magnitude higher, the radiative electron attachment rate coefficient would be six orders of magnitude higher due to the reduction in k_{-1}.

The parameters from Table 4.3 have, to the best of our knowledge, not been calculated for CH_3NC before now. Skurski et al. (2001) find that HNC has an electron affinity about five times that of HCN but, using the `Gaussian-09` package described in §3.5 and a level of theory to match that of the CH_3CN calculations, we find that the difference in CH_3CN and CH_3NC electron affinities is much smaller. As such, radiative electron attachment does not proceed significantly faster for CH_3NC than CH_3CN. The resultant rate for radiative electron attachment to CH_3CN with approximations at 10 K is 9.219×10^{-15} cm^3s^{-1} with an overall rate coefficient of $k_{att} = 1.683 \times 10^{-15}$ $(T/300\ K)^{-0.5}$ cm^3s^{-1} and without the approximations, the rate at 10 K is 4.012 $\times10^{-14}$ cm^3s^{-1} with an overall rate coefficient of $k_{att} = 7.324 \times 10^{-15}(T/300K)^{-0.5}$ cm^3s^{-1}.

4.5.2 Successive Hydrogenation on Grains

Thus far, we have considered gas-phase destruction and production routes for CH_3CN and CH_3NC because the primary production route seems to be gas-phase (see §4.2.2). But, grain-surface chemistry is often vital to understanding the abundance of complex organic molecules in the interstellar medium. Nguyen et al. (2019) point out that the differential barriers to hydrogenation on grain surfaces between CH_3CN and CH_3NC could lead to a preferential destruction of CH_3NC, since the barrier to hydrogenation is lower for this species. The reaction sequences here are

$$CH_3CN(s) + H(s) \rightarrow CH_3CHN(s) \qquad E_a = 4680\text{K} \tag{4.23a}$$

$$CH_3CHN(s) + H(s) \rightarrow CH_3CHNH(s) \tag{4.23b}$$

$$CH_3CHNH(s) + H(s) \rightarrow CH_3CHNH_2(s) \tag{4.23c}$$

$$CH_3CHNH_2(s) + H(s) \rightarrow CH_3CH_2NH_2(s) \tag{4.23d}$$

and

$$CH_3NC(s) + H(s) \rightarrow CH_3NCH(s) \qquad E_a = 1912\text{K} \tag{4.24a}$$

$$CH_3NCH(s) + H(s) \rightarrow CH_3NCH_2(s) \tag{4.24b}$$

$$CH_3NCH_2(s) + H(s) \rightarrow CH_3NHCH_2(s) \tag{4.24c}$$

$$CH_3NHCH_2(s) + H(s) \rightarrow CH_3NHCH_3(s). \tag{4.24d}$$

Nguyen et al. (2019) also find that, for both CH_3CN and CH_3NC, the addition of each new hydrogen has an activation energy barrier, but that the second, third, and fourth activation energy barriers are lower than the first one. A molecule of CH_3CN that is hydrogenated to CH_3CNH, could fairly easily proceed all the way to $CH_3CH_2NH_2$,

assuming that there is a sufficient amount of hydrogen on the grain surface and that hydrogen is sufficiently light to move on the surface of the grain easily.

In our models, neither the hydrogenation of CH_3CN nor CH_3NC affects the abundance of these species in the gas phase or on the surface. We also tested the effects of varying the desorption energy of CH_3CN by $\pm$ 2000 K from the standard desorption energy of 5686 K (Wakelam et al., 2017), to determine whether having more or less CH_3CN on the grain might allow for Equations 4.23a - 4.24d to have more of an effect, but there was still no change in the abundance of gas-phase CH_3CN.

Chapter 5

Conclusions and Future Directions

We have explored the effects of a variety of chemical processes to examine whether they could enhance chemical complexity in the cold, dark interstellar medium (ISM) as typified by the Taurus Molecular Cloud (TMC-1). Using a variety of theories and `Nautilus` models, we attempted to better capture the observed abundances of several molecules including HC_2O, $HCOOCH_3$, CH_3OCH_3, CH_3CN, CH_3NC, and H_2CCN.

5.1 Chapter Two

5.1.1 Major Conclusions

In this paper, we tested the effects of including radiolysis reactions in the `Nautilus` network. We found that including radiolysis at the standard TMC-1 cosmic ray ionization rate ζ of 10^{-17} increased the gas-phase abundances of COMs by creating suprathermal, highly reactive surface and bulk phase species. When these species react, products lift off of the grain. We also found that increasing ζ by orders of magnitude tends to increase the abundances of the species HOCO, NO_2, HC_2O, $HCOOCH_3$ at early times (before $\sim 10^3$ years) but begins to decrease the abundances of these molecules at later times (after $\sim 10^6$ years) as they interact with ionized species.

5.1.2 Future Directions

These results, while exciting, are preliminary. Further work remains to be done in at least three areas: examining the effects of cosmic rays on (1) the chemistry of the solid phases, (2) the processes responsible for lifting the solid phase products into the gas phase and (3) the chemistry of the gas-phase species.

Regarding the first of these, a nonzero electron escape probability P_e for Eq. (R1), for example, could affect the abundances of ions in the solid phases of the chemical kinetic models. The current approaches to radiolysis chemistry should also be expanded to include all of the grain-surface and bulk-mantle species in chemical networks, some of which was done by Paulive et al. (2021). Open questions also remain about the reactivity of species within the bulk, which may be different from the reactivity of grain-surface species.

To the second point, these results rely heavily on reactive desorption to increase gas-phase abundances. Paulive et al. (2022) details the inclusion of sputtering, whereby the energy of the incident ion directly causes desorption into the gas-phase, into chemical kinetic models. Two approaches to combining this work with photoexcitation and photodissociation effects can be found in Mullikin et al. (2021) and Carder et al. (2023). Further studies of nonthermal desorption mechanisms including desorption induced by electronic transitions and Auger stimulated ion desorption could also be included. Electron stimulated desorption, another nonthermal desorption mechanism, has been inferred to occur in interstellar environments by the experiments of Féraud et al. (2019), but no chemical kinetic modeling has been done on any of these three to the best of our knowledge.

Finally, gas-phase radiolysis chemistry should be expanded beyond the work of Herbst

& Klemperer (1973) on H_2.

5.2 Chapter Three

5.2.1 Major Conclusions

Here, we examined the radiative association reaction between CH_3O and CH_3 in some detail with a microcanonical phase-space approach and with a canonical approach. We found that the rate coefficient for this reaction was high compared to other radiative association reactions, helped along by a deep energetic well from the combination of radicals and by the large size of the product molecule with its infrared brightness and therefore its tendency toward stabilization. For all the speed of this reaction, however, its reliance on relatively low-abundance reactants means that it cannot explain the high abundance of CH_3OCH_3 in the cold ISM, or in TMC-1 in particular.

5.2.2 Future Directions

Radiative association between neutral radicals remains a viable and interesting way to build chemical complexity in the cold ISM. An example of a smaller molecule built by this radiative association is CH_2, which is formed predominantly by

$$C + H_2 \rightarrow CH_2 + h\nu \tag{5.1}$$

in our chemical kinetic models. This reaction has a relatively slow rate coefficient $k_{\rm ra}$ of 10^{-17} $\rm cm^3 s^{-1}$, since it does not have a deep radical-recombination potential well or many vibrational modes. It does benefit from very abundant reactants, however.

Any case with abundant precursor species, deep potential wells, and large molecules would be an ideal case to focus on in future radiative association studies.

Such an expansion of the reactions considered would improve the chemical kinetic network. There may also be improvements to the calculations. The novel `Fortran90` code written to calculate the phase-space rate coefficients in this work would benefit from parallelization, especially if it is to be used in future calculations at higher temperatures ($\geq$ 150 K), as these calculations can take days to run with the present form of the code.

5.3 Chapter Four

5.3.1 Major Conclusions

This chapter explored the related isomeric pairs CH_3CN and CH_3NC, H_2CCN and H_2CNC to determine their production and destruction routes in TMC-1. We found that the production of these species proceeds by radiative association followed by dissociative recombination, as shown below.

$$HCN/HNC + CH_3^+ \rightarrow CH_3CNH^+/CH_3NCH^+ \tag{5.2}$$

followed by

$$CH_3CHN^+/CH_3NCH^+ + e^- \rightarrow HCN/HNC + CH_3 \tag{5.3a}$$

$$\rightarrow H_2CCN/H_2CNC + 2H \tag{5.3b}$$

$$\rightarrow CH_3CN/CH_3NC + H \tag{5.3c}$$

We found that CH_3CN, CH_3NC, H_2CCN, and H_2CNC are predominantly destroyed by reaction with common interstellar ions, especially H_3^+ and C^+.

The observed isocyanide-to-cyanide ratios for these pairs are 5.9% for the closed-shell species and <2% for the radicals. While the closed-shell ratio is well captured by our model, the radical ratio is not.

5.3.2 Future Directions

As indicated by the addendum to Chapter 4 (§4.5), the most interesting future direction for modeling CH_3CN, CH_3NC, H_2CCN, and H_2CNC remains determining the reason for their overproduction to varying degrees. The divergence in the relatively small degree of overproduction of H_2CCN as compared to H_2CNC could point to eccentricities in their production or destruction routes. The overproduction of both CH_3CN and CH_3NC by about 1.5 orders of magnitude may indicate the overestimation of their production or a missing destruction route. Some suggestions about their production, destruction, abundance ratios, and relationships to visual extinction are given below.

Production Routes

The two steps in the production of CH_3CN, CH_3NC, H_2CCN, and H_2CNC could each be investigated more fully. If they are found to be less efficient than is currently modeled, this could help bring the modeled abundance of these species down to observed levels as shown in §4.2.1. The first step, radiative association between HCN/HNC and CH_3^+, could be slowed by lowering the available abundance of the

reactant CH_3^+. One mechanism to lower the modeled abundance of CH_3^+ is

$$CH_3^+ + H \rightarrow CH_4^+ + h\nu. \tag{5.4}$$

The bimolecular exit channel for this reaction, leading to CH_2^+ and H_2, is endothermic. Although the reaction of CH_3^+ with H_2 is well-studied and important in chemical kinetic models (Gerlich & Horning, 1992), the reaction of CH_3^+ and H is unstudied to the best of our knowledge. The ion CH_3^+ is implicated in many of the reactions in our chemical kinetic network, and lowering the abundance of this species could have many other consequences as well.

Alternatively, the radiative association reaction between HCN or HNC and CH_3^+ could have a competitive bimolecular exit channel, such as any of these:

$$HCN/HNC + CH_3^+ \rightarrow HCNH^+ + CH_2 \tag{5.5a}$$

$$\rightarrow H_2CN^+ + CH_2 \tag{5.5b}$$

$$\rightarrow H_2NC^+ + CH_2 \tag{5.5c}$$

$$\rightarrow CH_4 + CN^+ \tag{5.5d}$$

which could be included in the calculation of the overall rate coefficient as k_2 in Eq. 3.1. These reactions remain to be studied in detail to the best of our knowledge, though the collision complexes have been analyzed by Defrees et al. (1985). The proton affinities of HCN, HNC, and CH_2 may be compared, and the assumption can be made that the reactions 5.5a - 5.5c will proceed if CH_2 has a lower proton affinity than HCN and HNC (Garrod & Herbst, 2023). The proton affinity of CH_2 is 710.6 KJ mol^{-1}, while the experimental proton affinities of HCN and HNC are 712.9 and 772.3 kJ mol^{-1} when the incoming hydrogen adds to the same heavy atom as that to

which the other hydrogen is already attached (as in 5.5b and 5.5c) (Johnson, 1999). These values are too close to claim that a forward reaction will definitely take place, but it is worth producing a potential energy surface in order to calculate the rate in our opinion.

Destruction Routes

The photodestruction of CH_3CN

$$CH_3CN + h\nu \rightarrow CH_3CN^+ + e^- \tag{5.6}$$

$$CH_3CN^+ \rightarrow CH_3^+ + CN \tag{5.7}$$

is already in our reaction network, but currently the photodestruction of CH_3NC

$$CH_3NC + h\nu \rightarrow CH_3NC^+ + e^- \tag{5.8}$$

$$CH_3NC^+ \rightarrow CH_3^+ + CN \tag{5.9}$$

is simply assumed to proceed at the same rate. Note that Reactions 5.7 and 5.9 may lead to other fragments, which our model does take into account.

Both molecules were studied in the same VUV (Vacuum UltraViolet) conditions (Schwell et al., 2008; Bellili et al., 2019), with the result that slightly more CH_3CN could be photoionizied, leading to fragmentation, than CH_3NC when studying only

the range of light with wavelengths longer than 91.2 nm relevant to the interstellar medium. Heays et al. (2017) have shown that the absorption cross section $\sigma(\lambda)$ of a molecule can be integrated with the interstellar radiation field, I(λ), to get the rate coefficient of photoionization or photodissociation, k:

$$k = \int_{91.2}^{\infty} \sigma(\lambda) I \lambda d\lambda \tag{5.10}$$

where

$$I(\lambda) = 3.2028 \times 10^{13}\lambda^{-3} - 5.1542 \times 10^{15}\lambda^{-4} + 2.0546 \times 10^{17}\lambda^{-5}; \lambda < 200\text{nm} \tag{5.11a}$$

$$I(\lambda) = 3.67 \times 10^{4}\lambda^{0.7}; \lambda > 200\text{nm} \tag{5.11b}$$

from Draine (1978) and van Dishoeck & Black (1982). This method of destruction could help explain the isocyanide-to-cyanide ratios in a variety of interstellar environments because of its dependence on the local radiation field and the evidence from experimentation that CH_3CN and CH_3NC behave somewhat differently upon VUV radiation.

Isocyanide-to-Cyanide Ratios

The observed ratio of CH_3NC:CH_3CN is 5.9% in TMC-1 (Tennis et al., 2023). It is interesting to note that this ratio is close to the modeled ratio of 4.9% at the assumed age of TMC-1, 5×10^5 years, but that the modeled ratio is exactly 5.9% when the age of TMC-1 is taken instead to be 5.5×10^5 years. The H_2CNC:H_2CCN ratio also falls at this later time, though only to 68% and not nearly to the observed value of <2%. Careful observational analysis by Loomis et al. (2021) used cyanopolyyne chains to

arrive at the 5×10^5 year age of TMC-1, but also noted that the four distinct velocity components could be different in their chemical complexities or even their ages. We may be at the beginning of our understanding of TMC-1 as a multifaceted body, rather than at the end of our understanding the characteristics of a single cloud.

As noted above, a production route or destruction route that differentiates between CH_3CN and CH_3NC, or between H_2CCN and H_2CNC, could help explain their isocyanide-to-cyanide ratios. A competitive channel in the production that preferentially interferes with HNC reaction (such as Eq. 5.5c above) could produce less H_2CNC and thereby bring the H_2CNC:H_2CCN ratio down, for example. A destruction route like photoionization followed by dissociation (Eqs. 5.6 - 5.9) could preferentially destroy CH_3CN and bring the CH_3NC:CH_3CN ratio up.

Another method for matching the CH_3NC:CH_3CN ratio could be to re-examine the dissociative recombination branching ratios of Eqs. 4.8 - 4.19. Although the investigation in §4.2.2 considered a range of possibilities, the ratio of radicals (H_2CCN and H_2CNC) to closed-shell molecules (CH_3CN and CH_3NC) produced was held to the previously investigated ratio 38:62. Further, the experimental work of Vigren et al. (2008) finds a small molecule (HCN and HNC) to large molecule (CH_3CN, CH_3NC, H_2CCN, and H_2CNC) ratio of 35:65. If either of these ratio were altered, either the radicals or the closed-shell molecules might be found to match the observations more closely.

Isocyanide-to-Cyanide Ratio Relationship to Visual Extinction

The relationship between visual extinction A_v and the CH_3NC:CH_3CN ratio is worth investigating. It may point to the dominance of photodesruction routes in some re-

gions the ISM, as mentioned above. Alternatively, Basalgète et al. (2021) find that more intense UV radiation may increase the gas-phase abundance of CH_3CN by photodesorption, whereby photons lift molecules off of the grain rather than fragmenting them. The photodesorption of CH_3NC remains unstudied to the best of our knowledge.

Figure 5.1 gives the CH_3NC:CH_3CN ratio plotted against the visual extinction of the environment for all the locations CH_3NC has been detected to the best of our knowledge. Data for Figure 5.1 come from Gratier et al. (2013), Tennis et al. (2023), Megías et al. (2023), Remijan et al. (2005), and Calcutt (2018). The A_v of the Horsehead Nebula's Photon-Dominated Region (PDR) comes from Gratier et al. (2013); in all other cases, the visual extinctions are calculated by relation to the gas density using the formula from Bohlin et al. (1978).

Figure 5.1 shows a slight inverse relationship between visual extinction and CH_3NC:CH_3CN ratio. With so few detections of CH_3NC, this relationship must be considered tentative, though it is supported by Willis et al. (2020), who found in their models that varying the visual extinction (indirectly, by relation to the cosmic ray ionization rate, ζ) could help reproduce observed the observed ratio CH_3NC:CH_3CN in the high-mass star-forming region Sagittarius B2(N). To the best of our knowledge, no study to date has taken on the task of understanding the mechanism by which this relationship functions, but it is clear that A_v and the ratio CH_3NC:CH_3CN are intriguingly linked, and that the operational mechanism for this relationship would be of use in exploring the chemistry of interstellar environments.

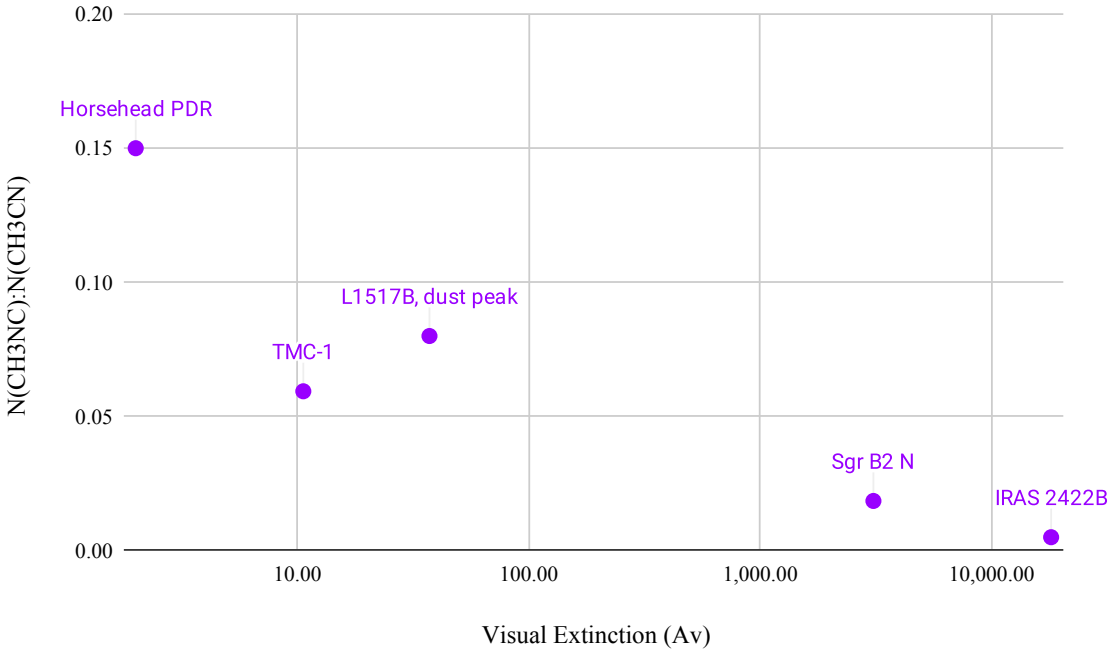

Figure 5.1: A log-normal plot of the CH_3NC:CH_3CN ratio against the visual extinction of the environment for all the locations CH_3NC has been detected.

5.4 Final Conclusions

It is something of a cliché to report that "the interstellar medium is an irreproduceable chemical laboratory," not to mention a possible slight offense to those who do work in experimental astrochemistry. Nonetheless, it remains the case that the chemical species, and especially the reaction mechanisms available to study there are wildly different from those we have at home. This thesis focused on just a handful of species in just one environment, TMC-1, and yet it entailed some nontrivial variety in chemistry (much to our delight). We found that cosmic rays can enhance H_2CO and $HCOOCH_3$ abundances in our chemical models and bring them much closer in line with observed abundances - until the cosmic ray fluence becomes so high that these H^+ and C^+ react quickly with much of the H_2CO and $HCOOCH_3$. We found

that radiative association between neutral radicals CH_3O and CH_3 could not explain the abundance of CH_3OCH_3, even when it happens on almost every collision of these radicals. We found that CH_3CN, CH_3NC, H_2CCN, and H_2CNC are subject to some unknown reactions, though whether it is a competitive channel in the production or an unknown destruction mechanism remains unclear. As further studies progress, there is no doubt that understanding and wonder at the small-scale physics of the far-off and sometimes incredible ISM will both continue to grow.

Bibliography

Abplanalp M. J., Gozem S., Krylov A. I., Shingledecker C. N., Herbst E., Kaiser R. I., 2016, PNAS, 113, 7727

Agúndez M., Marcelino N., Cernicharo J., Roueff E., Tafalla M., 2019, Astronomy & Astrophysics, 625, A147

Agúndez M., Marcelino N., Tercero B., Cabezas C., de Vicente P., Cernicharo J., 2021, Astronomy & Astrophysics, 649, L4

Agúndez M., et al., 2023, Astronomy & Astrophysics, 673, A34

Agúndez M., Cernicharo J., Guélin M., 2015, Astronomy & Astrophysics, 577, L5

Anicich V. G., Sen A. D., McEwan M. J., Smith S. C., 1994, Journal of Chemical Physics, 100, 5696

Anicich V. G., Sen A. D., Huntress Wesley T. J., McEwan M. J., 1995, Journal of Chemical Physics, 102, 3256

Ao Y., et al., 2013, Astronomy & Astrophysics, 550, A135

Atkinson R., et al., 2004, Atmospheric Chemistry and Physics, 4, 1461

Baade W., Zwicky F., 1934, PNAS, 20, 259

Bacmann A., Taquet V., Faure A., Kahane C., Ceccarelli C., 2012, Astronomy & Astrophysics, 541, L12

Balucani N., Ceccarelli C., Taquet V., 2015, Monthly Notices of the Royal Astronomical Society: Letters, 449, L16

Basalgète R., Ocaña A. J., Féraud G., Romanzin C., Philippe L., Michaut X., Fillion J.-H., Bertin M., 2021, The Astrophysical Journal, 922, 213

Baulch D. L., et al., 1992, Journal of Physical and Chemical Reference Data, 21, 411

Bellili A., Gouid Z., Gazeau M. C., Bénilan Y., Fray N., Guillemin J. C., Hochlaf M., Schwell M., 2019, Physical Chemistry Chemical Physics (Incorporating Faraday Transactions), 21, 26017

Bennett C. J., Kaiser R. I., 2005, The Astrophysical Journal, 635, 1362

Bergantini A., Góbi S., Abplanalp M. J., Kaiser R. I., 2018, The Astrophysical Journal, 852, 70

Bergner J. B., Öberg K. I., Rajappan M., 2017, The Astrophysical Journal, 845, 29

Bertin M., et al., 2013, The Astrophysical Journal, 779, 120

Bethe H., 1932, Zeitschrift fur Physik, 76, 293

Blasi P., 2013, Astronomy & Astrophysics Reviews, 21, 70

Bohlin R. C., Savage B. D., Drake J. F., 1978, The Astrophysical Journal, 224, 132

Bohr N., 1913, Philosophical Magazine, 25, 10

Burkhardt A. M., et al., 2021, The Astrophysical Journal Letters, 913, L18

Calcutt H., 2018, Astronomy & Astrophysics, 616

Calcutt H., et al., 2018, Astronomy & Astrophysics, 617, A95

Carder J. T., Paulive A., Herbst E., 2023, Monthly Notices of the Royal Astronomical Society, 519, 4622

Caselli P., Walmsley C. M., Terzieva R., Herbst E., 1998, The Astrophysical Journal, 499, 234

Ceccarelli C., Hily-Blant P., Montmerle T., Dubus G., Gallant Y., Fiasson A., 2011, The Astrophysical Journal, 740, L4

Cernicharo J., Kahane C., Guelin M., Gomez-Gonzalez J., 1988, Astronomy & Astrophysics, 189, L1

Cernicharo J., Marcelino N., Roueff E., Gerin M., Jiménez-Escobar A., Muñoz Caro G. M., 2012a, The Astrophysical Journal Letters, 759, L43

Cernicharo J., Marcelino N., Roueff E., Gerin M., Jiménez-Escobar A., Muñoz Caro G. M., 2012b, The Astrophysical Journal Letters, 759, L43

Chang Q., Herbst E., 2014, The Astrophysical Journal, 787, 135

Chang Q., Herbst E., 2016, The Astrophysical Journal, 819, 145

Chen L.-F., Li D., Quan D., Zhang X., Chang Q., Li X., Xiao L., 2022, The Astrophysical Journal, 928, 175

Churchwell E., Winnewisser G., Walmsley C. M., 1978, Astronomy & Astrophysics, 67, 139

Cleeves L. I., Bergin E. A., Öberg K. I., Andrews S., Wilner D., Loomis R., 2017, The Astrophysical Journal Letters, 843, L3

Compton A. H., Turner R. N., 1937, Physical Review, 52, 799

Cordiner M. A., Charnley S. B., Kisiel Z., McGuire B. A., Kuan Y.-J., 2017, The Astrophysical Journal, 850, 187

Cummings A. C., et al., 2016, The Astrophysical Journal, 831, 18

Dalgarno A., Griffing G. W., 1958, Proceedings of the Royal Society of London. Series A. Mathematical and Physical Sciences, 248, 415

Defrees D. J., McLean A. D., Herbst E., 1985, The Astrophysical Journal, 293, 236

Dewhurst H. A., et al., 1952, Discuss. Faraday Soc., 12, 312

Dobashi K., Shimoikura T., Nakamura F., Kameno S., Mizuno I., Taniguchi K., 2018, The Astrophysical Journal, 864, 82

Draine B. T., 1978, Astrophysical Journal Supplement, 36, 595

Edgar B. C., Miles W. T., Green A. E. S., 1973, Journal of Geophysical Research, 78, 6595

Elkomoss S. G., Magee J. L., 1962, The Journal of Chemical Physics, 36, 256

Féraud G., et al., 2019, ACS Earth and Space Chemistry, 3, 1135

Feuchtgruber H., Helmich F. P., van Dishoeck E. F., Wright C. M., 2000, The Astrophysical Journal Letters, 535, L111

Frisch M. J., et al., 2009, Gaussian 09 Revision A.02

Fueki K., Magee J. L., 1963, Discuss. Faraday Soc., 36, 19

Garrod R. T., Herbst E., 2023, Faraday Discussions

Garrod R. T., Wakelam V., Herbst E., 2007, Astronomy & Astrophysics, 467, 1103

Garrod R. T., Widicus Weaver S. L., Herbst E., 2008, The Astrophysical Journal, 682, 283

Garrod R. T., Belloche A., Müller H. S. P., Menten K. M., 2017, Astronomy & Astrophysics, 601, A48

Gerakines P. A., Moore M. H., Hudson R. L., 2001, Journal of Geophysical Research, 106, 33381

Gerakines P. A., Moore M. H., Hudson R. L., 2004, Icarus, 170, 202

Gerlich D., Horning S., 1992, Chemical Reviews, 92, 1509

Ginard D., et al., 2012, Astronomy & Astrophysics, 543, A27

Gockel A., Wulf T., 1908, Physikalische Zeitschrift, 9, 907

Goldsmith P. F., Langer W. D., 1978, The Astrophysical Journal, 222, 881

Graedel T. E., Langer W. D., Frerking M. A., 1982, The Astrophysical Journal Supplement, 48, 321

Graninger D. M., Herbst E., Öberg K. I., Vasyunin A. I., 2014, The Astrophysical Journal, 787, 74

Graninger D., Öberg K. I., Qi C., Kastner J., 2015, The Astrophysical Journal Letters, 807, L15

Gratier P., Pety J., Guzmán V., Gerin M., Goicoechea J. R., Roueff E., Faure A., 2013, Astronomy & Astrophysics, 557, A101

Grenier I. A., Black J. H., Strong A. W., 2015, Annual Review of Astronomy & Astrophysics, 53, 199

Hamberg M., et al., 2010, Astronomy & Astrophysics, 514, A83

Hasegawa T. I., Herbst E., 1993, Monthly Notices of the Royal Astronomical Society, 261, 83

Hasegawa T. I., Herbst E., Leung C. M., 1992, The Astrophysical Journal Supplement, 82, 167

Heays A. N., Bosman A. D., van Dishoeck E. F., 2017, Astronomy & Astrophysics, 602, A105

Heiles C., 1967, Astronomical Journal, 72, 1040

Herbst E., 1979, Journal of Chemical Physics, 70, 2201

Herbst E., 1980, The Astrophysical Journal, 237, 462

Herbst E., 1982, Chemical Physics, 65, 185

Herbst E., 1985, Astronomy & Astrophysics, 153, 151

Herbst E., 1987, The Astrophysical Journal, 313, 867

Herbst E., Klemperer W., 1973, The Astrophysical Journal, 185, 505

Herbst E., Millar T. J., 2008, The Chemistry of Cold Interstellar Cloud Cores. Imperial College Press

Herbst E., Osamura Y., 2008, The Astrophysical Journal, 679, 1670

Herbst E., Schubert J. G., Certain P. R., 1977, The Astrophysical Journal, 213, 696

Hincelin U., Wakelam V., Hersant F., Guilloteau S., Loison J. C., Honvault P., Troe J., 2011, Astronomy & Astrophysics, 530, A61

Holtom P. D., Bennett C. J., Osamura Y., Mason N. J., Kaiser R. I., 2005, The Astrophysical Journal, 626, 940

Hudson R. L., 2017, Phys. Chem. Chem. Phys.

Hudson R. L., Moore M. H., 2001, Journal of Geophysical Research, 106, 33275

Hudson R. L., Moore M. H., Dworkin J. P., Martin M. P., Pozun Z. D., 2008, Astrobiology, 8, 771

Husain D., Kirsch L. J., 1971, Trans. Faraday Soc., 67, 2025

Ip W.-H., Axford W. I., 1985, Astronomy & Astrophysics, 149, 7

Irvine W. M., Schloerb F. P., 1984, The Astrophysical Journal, 282, 516

Ivlev A. V., Röcker T. B., Vasyunin A., Caselli P., 2015a, The Astrophysical Journal, 805, 59

Ivlev A. V., Padovani M., Galli D., Caselli P., 2015b, The Astrophysical Journal, 812, 135

Jaber A. A., Ceccarelli C., Kahane C., Caux E., 2014, The Astrophysical Journal, 791, 29

Jenkins E. B., 2009, The Astrophysical Journal, 700, 1299

Jin M., Garrod R. T., 2020, The Astrophysical Journal Supplement Series, 249, 26

Johnson R. E., 1990, Energetic Charged-Particle Interactions with Atmospheres and Surfaces. No. 19 in Physics and Chemistry in Space, Springer-Verlag, Berlin

Johnson III R. D., 1999, NIST Computational Chemistry Comparison and Benchmark Database NIST Standard Reference Database Number 101, http://cccbdb.nist.gov/

Johnson R., 2011, in , Physics and Chemistry at Low Temperatures. Pan Stanford Publishing, pp 297–339, https://doi.org/10.1201/b11403-11

Johnson R. D., 2016, Technical Report 18, NIST Computational Chemistry Comparison and Benchmark Database. NIST

Keller-Rudek H., Moortgat G. K., Sander R., Sörensen R., 2013, Earth System Science Data, 5, 365

Klots C. E., 1971, J. Phys. Chem., 75, 1526

Lafosse A., Bertin M., Domaracka A., Pliszka D., Illenberger E., Azria R., 2006, Phys. Chem. Chem. Phys., 8, 5564

Landau L., Lifshitz E., 1976, Mechanics, 3 edn. Course of Theoretical Physics Vol. 1, Butterworth-Heinemann, Oxford

Lee H. H., Bettens R. P. A., Herbst E., 1996, Astronomy & Astrophysics Supplements, 119, 111

Lemaitre G., Vallarta M. S., 1933, Physical Review, 43, 87

Li Q., Osborne M. C., Smith I. W. M., 2000, International Journal of Chemical Kinetics, 32, 85

Liao Q., Herbst E., 1995, The Astrophysical Journal, 444, 694

Lias S. G., 2018, in Linstrom P. J., Mallard W. G., eds, , NIST Chemistry WebBook, NIST Standard Reference Database Number 69. National Institute of Standards and Technology, Gaithersburg, MD

Light J. C., 1967, Disc. Faraday Society, 44, 14

Little L. T., MacDonald G. H., Riley P. W., Matheson D. N., 1978, Monthly Notices of the Royal Astronomical Society, 183, 45P

Loison J.-C., Wakelam V., Hickson K. M., 2014, Monthly Notices of the Royal Astronomical Society, 443, 398

Loomis R. A., et al., 2021, Nature Astronomy, 5, 188

Luxford T. F. M., Nag P., 2021, European Physical Journal D, 75, 270

Marcus R. A., Rice O. K., 1951, J. Phys. Chem., 55, 894

Mason N. J., Nair B., Jheeta S., Szymańska E., 2014, Faraday Discussions, 168, 235

Matsumi Y., Inagaki Y., Kawasaki M., 1994, The Journal of Physical Chemistry, 98, 3777

Mayer S. W., Schieler L., Johnston H. S., 1967, Symposium (International) on Combustion, 11, 837

McGuire B. A., 2022, Astrophysical Journal Supplement, 259, 30

McGuire B. A., Burkhardt A. M., Shingledecker C. N., Kalenskii S. V., Eric Herbst Remijan A. J., McCarthy M. C., 2017a, The Astrophysical Journal Letters, 843, L28

McGuire B. A., et al., 2017b, The Astrophysical Journal Letters, 851, L46

McGuire B. A., Burkhardt A. M., Kalenskii S., Shingledecker C. N., Remijan A. J., Herbst E., McCarthy M. C., 2018, Science, 359, 202

McGuire B. A., et al., 2020, The Astrophysical Journal Letters, 900, L10

Megías A., Jiménez-Serra I., Martín-Pintado J., Vasyunin A. I., Spezzano S., Caselli P., Cosentino G., Viti S., 2023, Monthly Notices of the Royal Astronomical Society, 519, 1601

Miller W. H., 1979, JACS, 101, 6810

Morris M., Turner B. E., Palmer P., Zuckerman B., 1976, The Astrophysical Journal, 205, 82

Mullikin E., et al., 2021, The Astrophysical Journal, 910, 72

Neufeld D. A., Wolfire M. G., Schilke P., 2005, The Astrophysical Journal, 628, 260

Nguyen T., et al., 2019, Astronomy & Astrophysics, 628, A15

Öberg K. I., Bottinelli S., Jørgensen J. K., van Dishoeck E. F., 2010, The Astrophysical Journal, 716, 825

Parker E. N., 1958, Phys. Rev., 110, 1445

Paul D., et al., 2022, The Astrophysical Journal, 939, 122

Paulive A., Shingledecker C. N., Herbst E., 2021, Monthly Notices of the Royal Astronomical Society, 500, 3414

Paulive A., Carder J. T., Herbst E., 2022, Monthly Notices of the Royal Astronomical Society, 516, 4097

Peterson L. R., Green A. E. S., 1968, J. Phys. B, 1, 1131

Plessis S., Carrasco N., Pernot P., 2010, Journal of Chemical Physics, 133, 134110

Poggi G., Francisco J. S., 2004, The Journal of Chemical Physics, 120, 5073

Prasad S. S., Tarafdar S. P., 1983, The Astrophysical Journal, 267, 603

Purcell C. R., et al., 2006, Monthly Notices of the Royal Astronomical Society, 367, 553

Remijan A. J., Hollis J. M., Lovas F. J., Plusquellic D. F., Jewell P. R., 2005, The Astrophysical Journal, 632, 333

Ribeiro F. d. A., Almeida G. C., Garcia-Basabe Y., Wolff W., Boechat-Roberty H. M., Rocco M. L. M., 2015, Phys. Chem. Chem. Phys. (Incorporating Faraday Transactions), 17, 27473

Rimmer P. B., Herbst E., Morata O., Roueff E., 2012, Astronomy & Astrophysics, 537, A7

Rothard H., Domaracka A., Boduch P., Palumbo M. E., Strazzulla G., da Silveira E. F., Dartois E., 2017, J. Phys. B, 50, 062001

Ruaud M., Wakelam V., Hersant F., 2016, MNRAS, 459, 3756

Schilke P., Walmsley C. M., Pineau Des Forets G., Roueff E., Flower D. R., Guilloteau S., 1992, Astronomy & Astrophysics, 256, 595

Schwell M., Jochims H.-W., Baumgärtel H., Leach S., 2008, Chemical Physics, 344, 164

Shannon R. J., Cossou C., Loison J.-C., Caubet P., Balucani N., Seakins P. W., Wakelam V., Hickson K. M., 2014, RSC Advances, 4, 26342

Shingledecker C. N., Herbst E., 2018, Phys. Chem. Chem. Phys., 20, 5359

Shingledecker C. N., Bergner J. B., Le Gal R., Öberg K. I., Hincelin U., Herbst E., 2016, The Astrophysical Journal, 830, 151

Shingledecker C. N., Gal R. L., Herbst E., 2017, Phys. Chem. Chem. Phys., 19, 11043

Shingledecker C. N., Tennis J., Le Gal R., Herbst E., 2018, The Astrophysical Journal, 861, 20

Sivaramakrishnan R., Michael J. V., Wagner A. F., Dawes R., Jasper A., Harding L., Georgievskii Y., Klippenstein S. J., 2011, Combustion and Flame, 158, 618

Skurski P., Gutowski M., Simons J., 2001, Journal of Chemical Physics, 114, 7443

Snyder L. E., Buhl D., 1971, The Astrophysical Journal Letters, 163, L47

Snyder L. E., Buhl D., 1972, Annals of the New York Academy of Sciences, 194, 17

Solly R. K., Benson S. W., 1969, International Journal of Chemical Kinetics, 1, 427

Soma T., Sakai N., Watanabe Y., Yamamoto S., 2018, The Astrophysical Journal, 854, 116

Spinks J., Woods R., 1990, An introduction to radiation chemistry. Wiley, https://books.google.com/books?id=TQLwAAAAMAAJ

Spitzer Jr. L., Tomasko M. G., 1968, The Astrophysical Journal, 152, 971

Taquet V., Wirström E. S., Charnley S. B., Faure A., López-Sepulcre A., Persson C. M., 2017, Astronomy & Astrophysics, 607, A20

Tennis J., Loison J.-C., Herbst E., 2021, The Astrophysical Journal, 922, 133

Tennis J. D., Xue C., Talbi D., Changala P. B., Sita M. L., McGuire B., Herbst E., 2023, Monthly Notices of the Royal Astronomical Society

Tsang W., Hampson R. F., 1986, Journal of Physical and Chemical Reference Data, 15, 1087

Vastel C., Ceccarelli C., Lefloch B., Bachiller R., 2014, The Astrophysical Journal Letters, 795, L2

Vasyunin A. I., Herbst E., 2013a, The Astrophysical Journal, 769, 34

Vasyunin A. I., Herbst E., 2013b, The Astrophyical Journal, 769, 34

Vigren E., et al., 2008, Physical Chemistry Chemical Physics (Incorporating Faraday Transactions), 10, 4014

Wakelam V., Herbst E., 2008a, The Astrophysical Journal, 680, 371

Wakelam V., Herbst E., 2008b, The Astrophysical Journal, 680, 371

Wakelam V., et al., 2012, The Astrophysical Journal Supplement, 199, 21

Wakelam V., Loison J. C., Mereau R., Ruaud M., 2017, Molecular Astrophysics, 6, 22

Walter M., Wolfendale A. W., 2012, European Physical Journal H, 37, 323

Willis E. R., Garrod R. T., 2017, The Astrophysical Journal, 840, 61

Willis E. R., Garrod R. T., Belloche A., Müller H. S. P., Barger C. J., Bonfand M., Menten K. M., 2020, Astronomy & Astrophysics, 636, 1

Woon D. E., Herbst E., 2009a, The Astrophysical Journal Supplement, 185, 273

Woon D. E., Herbst E., 2009b, The Astrophysical Journal Supplement, 185, 273

Woon D. E., Maffucci D. M., Herbst E., 2021, Icarus, 354, 114051

Xue C., et al., 2020, The Astrophysical Journal Letters, 900, L9

Yu H.-G., Francisco J. S., 2009, J. Phys. Chem. A, 113, 3844

Yu H.-G., Muckerman J. T., Francisco J. S., 2005, J. Phys. Chem. A, 109, 5230

Yu H.-G., Muckerman J. T., Francisco J. S., 2007, The Journal of Chemical Physics, 127, 094302

Yusef-Zadeh F., et al., 2013a, The Astrophysical Journal, 762, 33

Yusef-Zadeh F., Cotton W., Viti S., Wardle M., Royster M., 2013b, The Astrophysical Journal Letters, 764, L19

Ziegler J. F., Biersack J. P., 1985, in Bromley D. A., ed., , Treatise on Heavy-Ion Science, by Bromley, D. Allan, ISBN 978-1-4615-8105-5.. Springer-Verlag US, p. 93

van Dishoeck E. F., Black J. H., 1982, The Astrophysical Journal, 258, 533

Appendices

Appendix A

Tables of Reactions Added to `Nautilus`

A.1 Reactions Added to `Nautilus` to Model Cosmic Ray Interactions.

A.1.1 New radiolysis reactions; see Chapter 2.

Continued on the next page.

8	$O_3 \rightsquigarrow O_2^* + O^*$	1.000	3.704	I
9	$O_3 \rightsquigarrow O_2 + O$	1.000	4.059	II
10	$O_3 \rightsquigarrow O_3^*$	1.000	4.059	III
	CO			
11	$CO \rightsquigarrow C^* + O^*$	1.000	3.704	I
12	$CO \rightsquigarrow C + O$	1.000	1.269	II
13	$CO \rightsquigarrow CO^*$	1.000	1.269	III
	CO_2			
14	$CO_2 \rightsquigarrow CO^* + O^*$	1.000	3.704	I
15	$CO_2 \rightsquigarrow CO + O$	1.000	1.249	II
16	$CO_2 \rightsquigarrow CO_2^*$	1.000	1.249	III
	NO			

Table A.1: New solid-phase radiolysis processes

Number	**Process**	f_{br}	G**-value**	**Type**
	H_2O			
1	$H_2O \rightsquigarrow O^* + H_2^*$	0.500	3.704	1I
2	$H_2O \rightsquigarrow OH^* + H^*$	0.500	3.704	I
3	$H_2O \rightsquigarrow OH + H$	1.000	1.747	II
4	$H_2O \rightsquigarrow H_2O$	1.000	1.747	III
	O_2			
5	$O_2 \rightsquigarrow O^* + O^*$	1.000	3.704	I
6	$O_2 \rightsquigarrow O + O$	1.000	2.138	II
7	$O_2 \rightsquigarrow O_2^*$	1.000	2.138	III
	O_3			

17	$NO \rightsquigarrow N^* + O^*$	1.000	3.704	I
18	$NO \rightsquigarrow N + O$	1.000	1.922	II
19	$NO \rightsquigarrow NO^*$	1.000	1.922	III
	NO_2			
20	$NO \rightsquigarrow NO^* + O^*$	1.000	3.704	I
21	$NO \rightsquigarrow NO + O$	1.000	1.207	II
22	$NO \rightsquigarrow NO_2^*$	1.000	1.207	III
	O_2H			
23	$O_2H \rightsquigarrow OH^* + O^*$	1.000	3.704	I
24	$O_2H \rightsquigarrow OH + O$	1.000	3.714	II
25	$O_2H \rightsquigarrow O_2H^*$	1.000	3.714	III
	H_2O_2			
26	$H_2O_2 \rightsquigarrow OH^* + OH^*$	0.500	3.704	I

Table A.1: New solid-phase radiolysis processes

Number	**Process**	f_{br}	G**-value**	**Type**
	H_2O			
1	$H_2O \rightsquigarrow O^* + H_2^*$	0.500	3.704	1I
2	$H_2O \rightsquigarrow OH^* + H^*$	0.500	3.704	I
3	$H_2O \rightsquigarrow OH + H$	1.000	1.747	II
4	$H_2O \rightsquigarrow H_2O$	1.000	1.747	III
	O_2			
5	$O_2 \rightsquigarrow O^* + O^*$	1.000	3.704	I
6	$O_2 \rightsquigarrow O + O$	1.000	2.138	II
7	$O_2 \rightsquigarrow O_2^*$	1.000	2.138	III
	O_3			

27	$H_2O_2 \rightsquigarrow O^* + H_2O^*$	0.500	3.704	I
28	$H_2O_2 \rightsquigarrow OH + OH^*$	1.000	2.296	II
	NH_3			
29	$NH_3 \rightsquigarrow H^* + NH_2^*$	0.500	3.704	I
30	$NH_3 \rightsquigarrow H_2^* + NH^*$	0.500	3.704	I
31	$NH_3 \rightsquigarrow H + NH_2$	1.000	2.721	II
32	$NH_3 \rightsquigarrow NH_3^*$	1.000	2.721	III
	CH_4			
33	$CH_4 \rightsquigarrow H^* + CH_3^*$	0.500	3.704	I
34	$CH_4 \rightsquigarrow H_2 + CH_2^*$	0.500	3.704	I[a]
35	$CH_4 \rightsquigarrow H + CH_3$	1.000	1.505	II
36	$CH_4 \rightsquigarrow CH_4^*$	1.000	1.505	III
	H_2CO			

Table A.1: New solid-phase radiolysis processes

Number	**Process**	f_{br}	G**-value**	**Type**
	H_2O			
1	$H_2O \rightsquigarrow O^* + H_2^*$	0.500	3.704	1I
2	$H_2O \rightsquigarrow OH^* + H^*$	0.500	3.704	I
3	$H_2O \rightsquigarrow OH + H$	1.000	1.747	II
4	$H_2O \rightsquigarrow H_2O$	1.000	1.747	III
	O_2			
5	$O_2 \rightsquigarrow O^* + O^*$	1.000	3.704	I
6	$O_2 \rightsquigarrow O + O$	1.000	2.138	II
7	$O_2 \rightsquigarrow O_2^*$	1.000	2.138	III
	O_3			

37	$H_2CO \rightsquigarrow H^* + HCO^*$	1.000	3.704	I
38	$H_2CO \rightsquigarrow H + HCO$	1.000	2.910	II
39	$H_2CO \rightsquigarrow H_2CO^*$	1.000	2.910	I
	CH_3OH			
40	$CH_3OH \rightsquigarrow H^* + CH_3O^*$	0.333	3.704	I
41	$CH_3OH \rightsquigarrow H^* + CH_2OH^*$	0.333	3.704	I
42	$CH_3OH \rightsquigarrow OH^* + CH_3^*$	0.333	3.704	I
43	$CH_3OH \rightsquigarrow H + CH_3O$	0.333	1.571	II
44	$CH_3OH \rightsquigarrow H + CH_2OH$	0.333	1.571	II
45	$CH_3OH \rightsquigarrow OH + CH_3$	0.333	1.571	II
46	$CH_3OH \rightsquigarrow CH_3OH^*$	1.000	1.571	III
	CH_3COCH_3			
47	$CH_3COCH_3 \rightsquigarrow CH_3^* + CH_3CO^*$	1.000	3.704	I[b]

Table A.1: New solid-phase radiolysis processes

Number	**Process**	f_{br}	G**-value**	**Type**
	H_2O			
1	$H_2O \rightsquigarrow O^* + H_2^*$	0.500	3.704	1I
2	$H_2O \rightsquigarrow OH^* + H^*$	0.500	3.704	I
3	$H_2O \rightsquigarrow OH + H$	1.000	1.747	II
4	$H_2O \rightsquigarrow H_2O$	1.000	1.747	III
	O_2			
5	$O_2 \rightsquigarrow O^* + O^*$	1.000	3.704	I
6	$O_2 \rightsquigarrow O + O$	1.000	2.138	II
7	$O_2 \rightsquigarrow O_2^*$	1.000	2.138	III
	O_3			

48	$CH_3COCH_3 \rightsquigarrow CH_3 + CH_3CO$	1.000	4.020	II
49	$CH_3COCH_3 \rightsquigarrow CH_3COCH_3^*$	1.000	4.020	III

[a] Bergantini et al. (2018)

[b] Hudson (2017)

Table A.1: New solid-phase radiolysis processes

Number	Process	f_{br}	G-value	Type
	H_2O			
1	$H_2O \rightsquigarrow O^* + H_2^*$	0.500	3.704	1I
2	$H_2O \rightsquigarrow OH^* + H^*$	0.500	3.704	I
3	$H_2O \rightsquigarrow OH + H$	1.000	1.747	II
4	$H_2O \rightsquigarrow H_2O$	1.000	1.747	III
	O_2			
5	$O_2 \rightsquigarrow O^* + O^*$	1.000	3.704	I
6	$O_2 \rightsquigarrow O + O$	1.000	2.138	II
7	$O_2 \rightsquigarrow O_2^*$	1.000	2.138	III
	O_3			

A.1.2 Class 2 Reactions

Table A.2: New Class 2 reactions involving suprathermal species.

Number	Reaction	f_{br}	Source
	C^*		
50	$C^* + H_2O \rightarrow CH + OH$	1.0	Mayer et al. (1967)
51	$C^* + CO \rightarrow CCO$	1.0	Husain & Kirsch (1971)
52	$C^* + CH_3OH \rightarrow CH_3CHO$	0.5	Shannon et al. (2014)
53	$C^* + CH_3OH \rightarrow CH_3 + HCO$	0.5	Shannon et al. (2014)
	O^*		

54	$O^* + CH_4 \rightarrow CH_3OH$	0.65	Bergner et al. (2017)
55	$O^* + CH_4 \rightarrow H_2CO + H_2$	0.35	Bergner et al. (2017)
56	$O^* + CH_3OH \rightarrow CH_3 + HCO$	1.0	Matsumi et al. (1994)
57	$O^* + NO \rightarrow NO_2$	1.0	Atkinson et al. (2004)
	CH_2^*		
58	$CH_2^* + CH_3OH \rightarrow CH_3CH_2OH$	0.5	Bergantini et al. (2018)
59	$CH_2^* + CH_3OH \rightarrow CH_3OCH_3$	0.5	Bergantini et al. (2018)

A.1.3 New HOCO Reactions

Table A.3: New gas-phase HOCO destruction reactions

Number	Reaction	α	β	γ	Source
		Neutral-Neutral[a]			
		s^{-1}	K		
60	$HOCO + Cl \rightarrow HCl + CO_2$	4.800×10^{-11}	0.000	0.000	Li et al. (2000)
61	$HOCO + O_2 \rightarrow O_2H + CO_2$	1.900×10^{-12}	0.000	0.000	Poggi & Francisco (2004)
62	$HOCO + NO \rightarrow HNO + CO_2$	2.450×10^{-12}	0.000	0.000	Poggi & Francisco (2004)
63	$HOCO + O \rightarrow OH + CO_2$	1.440×10^{-11}	0.000	0.000	Yu et al. (2007)
64	$HOCO + OH \rightarrow H_2O + CO_2$	1.030×10^{-11}	0.000	0.000	Yu et al. (2005)
65	$HOCO + CH_3 \rightarrow H_2O + H2C_2O$	5.800×10^{-11}	0.000	0.000	Yu & Francisco (2009)
		Ion-Neutral[b]			
		f_{br}	$cm^3\ s^{-1}$		
66	$HOCO + H^+ \rightarrow HOCO^+ + H$	1.000	5.049×10^{-9}	9.438	See Text
67	$HOCO + H_3^+ \rightarrow HOCO^+ + H + H_2$	1.000	2.978×10^{-9}	9.438	See Text
68	$HOCO + He^+ \rightarrow HOCO^+ + He$	1.000	3.609×10^{-9}	9.438	See Text
69	$HOCO + C^+ \rightarrow HOCO^+ + C$	1.000	1.623×10^{-9}	9.438	See Text

(a) See Eq. (2.23)

(b) See Woon & Herbst (2009a)

A.2 Reactions added to `Nautilus` for Chapter 4

Table A.4 below gives the gas-phase and then the grain-surface reactions added to our model for CH_3CN. Adsorption, desorption, bulk mixing, and grain-surface photodestruction reactions are also included for each new species of interest and precursor but are not listed.

Table A.4: Reactions added to `Nautilus`.

Gas-Phase Reaction	Rate [cm^3s^{-1}]	Reference
$H + CH_3NC \rightarrow HCN + CH_3$	$3.42x10^{-14}\ (T/300K)^{-2.19}e^{-1102K/T}$	[a]
$CH_3CNH^+ + e^- \rightarrow H + CH_3NC$	$4.55x10^{-8}\ (T/300K)^{-0.69}$	[a]
$CH_3NCH^+ + e^- \rightarrow H + H + H_2CNC$	$1.71x10^{-7}\ (T/300K)^{-0.69}$	[a]
$CH_3NCH^+ + e^- \rightarrow H + H + H_2CCN$	$3.02x10^{-8}\ (T/300K)^{-0.69}$	[a]
$CH_3NCH^+ + e^- \rightarrow H + CH_3CN$	$4.98x10^{-8}\ (T/300K)^{-0.69}$	[a]
$CH_3NCH^+ + e^- \rightarrow H + CH_3NC$	$2.78x10^{-7}\ (T/300K)^{-0.69}$	[a]
$CH_3NCH^+ + e^- \rightarrow HNC + CH_3$	$2.42x10^{-7}\ (T/300K)^{-0.69}$	[a]
$CH_3NCH^+ + e^- \rightarrow HCN + CH_3$	$4.27x10^{-8}\ (T/300K)^{-0.69}$	[a]
$CH_2NC^+ + e^- \rightarrow CH + HCN$	$2.00x10^{-7}\ (T/300K)^{-0.5}$	[b]
$CH_2NC^+ + e^- \rightarrow CN + CH_2$	$2.00x10^{-7}\ (T/300K)^{-0.5}$	[b]
$CH_2NC^+ + e^- \rightarrow H + H + CCN$	$2.00x10^{-7}\ (T/300K)^{-0.5}$	[b]
$CH_3NC^+ + e^- \rightarrow H + H_2 + CCN$	$2.00x10^{-7}\ (T/300K)^{-0.5}$	[b]
$CH_3NC^+ + e^- \rightarrow CH_2 + HCN$	$1.00x10^{-7}\ (T/300K)^{-0.5}$	[b]
$CH_3NC^+ + e^- \rightarrow CN + CH_3$	$1.00x10^{-7}\ (T/300K)^{-0.5}$	[b]
$CH_3NC^+ + e^- \rightarrow H + H_2CNC$	$2.00x10^{-7}\ (T/300K)^{-0.5}$	[b]
$H_2CCN + He^+ \rightarrow He + CH_2^+ + CN$	$2.57x10^{-9}[0.62+2.77(300K/T)^{0.5}]$	[a,c]
$H_2CCN + H_3^+ \rightarrow H_2 + CH_3CN^+$	$4.90x10^{-9}[0.62+2.77(300K/T)^{0.5}]$	[a,c]
$H_2CCN + C^+ \rightarrow C + CH_2CN^+$	$1.61x10^{-9}[0.62+2.77(300K/T)^{0.5}]$	[a,c]
$H_2CCN + HCO^+ \rightarrow CO + CH_3CN^+$	$1.19x10^{-9}[0.62+2.77(300K/T)^{0.5}]$	[a,c]
$H_2CCN + H_3O^+ \rightarrow H_2O + CH_3CN^+$	$1.36x10^{-9}[0.62+2.77(300K/T)^{0.5}]$	[a,c]
$H_2CCN + HOCO^+ \rightarrow CO_2 + CH_3CN^+$	$1.06x10^{-9}[0.62+2.77(300K/T)^{0.5}]$	[a,c]
$H_2CCN + H^+ \rightarrow H + CH_2CN^+$	$4.94x10^{-9}[0.62+2.77(300K/T)^{0.5}]$	[a,c]
$H_2CNC + He^+ \rightarrow He + CH_2^+ + CN$	$2.57x10^{-9}[0.62+2.77(300K/T)^{0.5}]$	[b]
$H_2CNC + H_3^+ \rightarrow H_2 + CH_3NC^+$	$4.90x10^{-9}[0.62+2.77(300K/T)^{0.5}]$	[b]
$H_2CNC + C^+ \rightarrow C + CH_2NC^+$	$1.61x10^{-9}[0.62+2.77(300K/T)^{0.5}]$	[b]
$H_2CNC + HCO^+ \rightarrow CO + CH_3NC^+$	$1.19x10^{-9}[0.62+2.77(300K/T)^{0.5}]$	[b]
$H_2CNC + H_3O^+ \rightarrow H_2O + CH_3NC^+$	$1.36x10^{-9}[0.62+2.77(300K/T)^{0.5}]$	[b]

$H_2CNC + HOCO^+ \rightarrow CO_2 + CH_3NC^+$	$1.06x10^{-9}[0.62+2.77(300K/T)^{0.5}]$	b
$H_2CNC + H^+ \rightarrow H + CH_2NC^+$	$4.94x10^{-9}[0.62+2.77(300K/T)^{0.5}]$	b
$CH_3CN + He^+ \rightarrow He + CN^+ + CH_3$	$1.27x10^{-9}[0.62+3.14(300K/T)^{0.5}]$	a,c
$CH_3CN + He^+ \rightarrow He + CH_3^+ + CN$	$1.27x10^{-9}[0.62+3.14(300K/T)^{0.5}]$	a,c
$CH_3CN + H_3^+ \rightarrow H_2 + CH_3CNH^+$	$4.84x10^{-9}[0.62+3.14(300K/T)^{0.5}]$	a,c
$CH_3CN + C^+ \rightarrow CN + C_2H_3^+$	$7.94x10^{-10}[0.62+3.14(300K/T)^{0.5}]$	a,c
$CH_3CN + C^+ \rightarrow H + HC_2NCH^+$	$7.94x10^{-10}[0.62+3.14(300K/T)^{0.5}]$	a,c
$CH_3CN + HCO^+ \rightarrow CO + CH_3CNH^+$	$1.17x10^{-9}[0.62+3.14(300K/T)^{0.5}]$	a,c
$CH_3CN + H_3O^+ \rightarrow H_2O + CH_3CNH^+$	$1.34x10^{-9}[0.62+3.14(300K/T)^{0.5}]$	a,c
$CH_3CN + HOCO^+ \rightarrow CO_2 + CH_3CNH^+$	$1.05x10^{-9}[0.62+3.14(300K/T)^{0.5}]$	a,c
$CH_3CN + H^+ \rightarrow H_2 + CH_2CN^+$	$2.44x10^{-9}[0.62+3.14(300K/T)^{0.5}]$	a,c
$CH_3CN + H^+ \rightarrow H + CH_3CN^+$	$2.44x10^{-9}[0.62+3.14(300K/T)^{0.5}]$	a,c
$CH_3NC + He^+ \rightarrow He + CH_3^+ + CN$	$1.27x10^{-9}[0.62+3.00(300K/T)^{0.5}]$	a,c
$CH_3NC + He^+ \rightarrow He + CH_3 + CN^+$	$1.27x10^{-9}[0.62+3.00(300K/T)^{0.5}]$	a,c
$CH_3NC + H_3^+ \rightarrow H_2 + CH_3NCH^+$	$4.84x10^{-9}[0.62+3.00(300K/T)^{0.5}]$	a,c
$CH_3NC + C^+ \rightarrow CN + C_2H_3^+$	$7.93x10^{-10}[0.62+3.00(300K/T)^{0.5}]$	a,c
$CH_3NC + C^+ \rightarrow H + HC_2NCH^+$	$7.93x10^{-10}[0.62+3.00(300K/T)^{0.5}]$	a,c
$CH_3NC + HCO^+ \rightarrow CO + CH_3NCH^+$	$1.17x10^{-9}[0.62+3.00(300K/T)^{0.5}]$	a,c
$CH_3NC + H_3O^+ \rightarrow H_2O + CH_3NCH^+$	$1.34x10^{-9}[0.62+3.00(300K/T)^{0.5}]$	a,c
$CH_3NC + HOCO^+ \rightarrow CO_2 + CH_3NCH^+$	$1.04x10^{-9}[0.62+3.00(300K/T)^{0.5}]$	a,c
$CH_3NC + H^+ \rightarrow H_2 + CH_2NC^+$	$2.44x10^{-9}[0.62+3.00(300K/T)^{0.5}]$	a,c
$CH_3NC + H^+ \rightarrow H + CH_3NC^+$	$2.44x10^{-9}[0.62+3.00(300K/T)^{0.5}]$	a,c
$CH_3NC + H \rightarrow CH_3 + HCN$	$e^{-1200K/T}$	b
$CO + CH_3NC^+ \rightarrow H_2CNC + HCO^+$	$8.03x10^{-10}$ $[1+0.024(300K/T)^{0.5}+0.006(300K/T)^{-1}]$	b
$CO + CH_3NC^+ \rightarrow H_2CCN + HCO^+$	$8.03x10^{-10}$ $[1+0.024(300K/T)^{0.5}+0.006(300K/T)^{-1}]$	b
$CO + CH_3CN^+ \rightarrow H_2CNC + HCO^+$	$8.03x10^{-10}$ $[1+0.024(300K/T)^{0.5}+0.006(300K/T)^{-1}]$	b
$CN + CH_3 \rightarrow CH_3NC + Photon$	$2.86x10^{-17}$	a,b
$HNC + CH_3^+ \rightarrow CH_3NCH^+ + Photon$	$9.00x10^{-9}$ $(T/300K)^{-0.5}$	d
$CH_3 + CN^- \rightarrow CH_3NC + e^-$	$1.00x10^{-9}$	b
$CH_2OH + C_2H_4CN \rightarrow C_2H_5CN + H_2CO$	$1.00x10^{-11}$	e
$CH_2OH + C_2H_4NC \rightarrow C_2H_5NC + H_2CO$	$1.00x10^{-11}$	e

$CH_2OH + CH_3CHCN \rightarrow C_2H_5CN + H_2CO$	1.00x10^{-11}	^{e}
$CH_2OH + CH_3CHNC \rightarrow C_2H_5NC + H_2CO$	1.00x10^{-11}	^{e}
$CH_3O + C_2H_4CN \rightarrow C_2H_5CN + H_2CO$	1.00x10^{-11}	^{e}
$CH_3O + C_2H_4NC \rightarrow C_2H_5NC + H_2CO$	1.00x10^{-11}	^{e}
$CH_3O + CH_3CHCN \rightarrow C_2H_5CN + H_2CO$	1.00x10^{-11}	^{e}
$CH_3O + CH_3CHNC \rightarrow C_2H_5NC + H_2CO$	1.00x10^{-11}	^{e}
$HCO + C_2H_4CN \rightarrow C_2H_5CN + CO$	1.00x10^{-11}	^{e}
$HCO + C_2H_4NC \rightarrow C_2H_5NC + CO$	1.00x10^{-11}	^{e}
$HCO + CH_3CHCN \rightarrow C_2H_5CN + CO$	1.00x10^{-11}	^{e}
$HCO + CH_3CHNC \rightarrow C_2H_5NC + CO$	1.00x10^{-11}	^{e}
$CH_3CN + e^- \rightarrow CH_3 + CN^-$	6.399x10^{-15}(T/300 K)$^{-0.5}$ cm^{3}s^{-1}	^{g,h}
$CH_3NC + CRP \rightarrow CN + CH_3$	4.76x10^3 ζ	^{b}
$CH_3NC + CRP \rightarrow CH_3NC^+ + e^-$	2.24x10^3 ζ	^{b}
$CH_3NC + Photon \rightarrow CN + CH_3$	2.50x10$^{-9}e^{-2.58A_v}$	^{b}
$CH_3NC + Photon \rightarrow CH_3NC^+ + e^-$	6.20x10$^{-10}e^{-3.11A_v}$	^{b}
$H_2CNC + Photon \rightarrow CH_2NC^+ + e^-$	2.65x10$^{-10}e^{-3.11A_v}$	^{b}

Grain-Surface Reaction	Activation Energy [K]	Reference
$CH_2OH + C_2H_4CN \rightarrow C_2H_5CN + H_2CO$	0	^{e}
$CH_2OH + C_2H_4NC \rightarrow C_2H_5NC + H_2CO$	0	^{e}
$CH_2OH + C_2H_5CN \rightarrow CH_3OH + C_2H_4CN$	6490	^{e}
$CH_2OH + C_2H_5NC \rightarrow CH_3OH + C_2H_4NC$	6490	^{e}
$CH_2OH + C_2H_5CN \rightarrow CH_3OH + CH_3CHCN$	5990	^{e}
$CH_2OH + C_2H_5NC \rightarrow CH_3OH + CH_3CHNC$	5990	^{e}
$CH_2OH + H_2CCN \rightarrow CH_3CN + H_2CO$	0	^{e}
$CH_2OH + H_2CNC \rightarrow CH_3NC + H_2CO$	0	^{e}
$CH_2OH + CH_3CN \rightarrow CH_3OH + H_2CCN$	6200	^{e}
$CH_2OH + CH_3NC \rightarrow CH_3OH + H_2CNC$	6200	^{e}
$CH_2OH + CH_3CHCN \rightarrow H_2CO + C_2H_5CN$	0	^{e}
$CH_2OH + CH_3CHNC \rightarrow H_2CO + C_2H_5NC$	0	^{e}

$CH_3 + H_2CCN \rightarrow C_2H_5CN$	0	[e]
$CH_3 + H_2CNC \rightarrow C_2H_5NC$	0	[e]
$CH_3O + C_2H_4CN \rightarrow C_2H_5CN + H_2CO$	0	[e]
$CH_3O + C_2H_4NC \rightarrow C_2H_5NC + H_2CO$	0	[e]
$CH_3O + C_2H_5CN \rightarrow C_2H_4CN + CH_3OH$	2340	[e]
$CH_3O + C_2H_5NC \rightarrow C_2H_4NC + CH_3OH$	2340	[e]
$CH_3O + C_2H_5CN \rightarrow CH_3CHCN + CH_3OH$	1950	[e]
$CH_3O + C_2H_5NC \rightarrow CH_3CHNC + CH_3OH$	1950	[e]
$CH_3O + H_2CCN \rightarrow CH_3CN + H_2CO$	0	[e]
$CH_3O + H_2CNC \rightarrow CH_3NC + H_2CO$	0	[e]
$CH_3O + CH_3CN \rightarrow CH_3OH + H_2CCN$	2070	[e]
$CH_3O + CH_3NC \rightarrow CH_3OH + H_2CNC$	2070	[e]
$CH_3O + CH_3CHCN \rightarrow C_2H_5CN + H_2CO$	0	[e]
$CH_3O + CH_3CHNC \rightarrow C_2H_5NC + H_2CO$	0	[e]
$H + C_2H_2CN \rightarrow CH_2CHCN$	0	[e]
$H + C_2H_2NC \rightarrow C_2H_3NC$	0	[e]
$H + CH_2CHCN \rightarrow C_2H_4CN$	1320	[e]
$H + C_2H_3NC \rightarrow C_2H_4NC$	1320	[e]
$H + CH_2CHCN \rightarrow CH_3CHCN$	619	[e]
$H + C_2H_3NC \rightarrow CH_3CHNC$	619	[e]
$H + C_2H_4CN \rightarrow C_2H_5CN$	0	[e]
$H + C_2H_4NC \rightarrow C_2H_5NC$	0	[e]
$H + CH_3CHCN \rightarrow C_2H_5CN$	0	[e]
$H + CH_3CHNC \rightarrow C_2H_5NC$	0	[e]
$H + H_2CNC \rightarrow CH_3NC$	0	[b]
$H + CH_3CN \rightarrow HCN + CH_3$	1200	[e]
$H + CH_3NC \rightarrow HCN + CH_3$	1200	[e]
$H + HC_3N \rightarrow C_2H_2CN$	1710	[e]
$H + HCCNC \rightarrow C_2H_2NC$	1710	[e]
$H + HCN \rightarrow H + HNC$	0	[e]
$H + HNC \rightarrow H + HCN$	1200	[e]

$H_2CCN + CH_2 \rightarrow C_2H_4CN$	0	[e]
$H_2CNC + CH_2 \rightarrow C_2H_4NC$	0	[e]
$HCO + C_2H_4CN \rightarrow C_2H_5CN + CO$	0	[e]
$HCO + C_2H_4NC \rightarrow C_2H_5NC + CO$	0	[e]
$HCO + H_2CCN \rightarrow CH_3CN + CO$	0	[e]
$HCO + H_2CNC \rightarrow CH_3NC + CO$	0	[e]
$HCO + CH_3CHCN \rightarrow C_2H_5CN + CO$	0	[e]
$HCO + CH_3CHNC \rightarrow C_2H_5NC + CO$	0	[e]
$HOCO + C_2H_4CN \rightarrow C_2H_5CN + CO_2$	0	[e]
$HOCO + C_2H_4NC \rightarrow C_2H_5NC + CO_2$	0	[e]
$HOCO + H_2CCN \rightarrow CH_3CN + CO_2$	0	[e]
$HOCO + H_2CNC \rightarrow CH_3NC + CO_2$	0	[e]
$HOCO + CH_3CHCN \rightarrow C_2H_5CN + CO_2$	0	[e]
$HOCO + CH_3CHNC \rightarrow C_2H_5NC + CO_2$	0	[e]
$NH + C_2H_5CN \rightarrow NH_2 + C_2H_4CN$	7200	[e]
$NH + C_2H_5NC \rightarrow NH_2 + C_2H_4NC$	7200	[e]
$NH + C_2H_5CN \rightarrow NH_2 + CH_3CHCN$	7000	[e]
$NH + C_2H_5NC \rightarrow NH_2 + CH_3CHNC$	7000	[e]
$NH + CH_3CN \rightarrow NH_2 + H_2CCN$	7000	[e]
$NH + CH_3NC \rightarrow NH_2 + H_2CNC$	7000	[e]
$NH_2 + C_2H_5CN \rightarrow NH_3 + C_2H_4CN$	3280	[e]
$NH_2 + C_2H_5NC \rightarrow NH_3 + C_2H_4NC$	3280	[e]
$NH_2 + C_2H_5CN \rightarrow NH_3 + CH_3CHCN$	2480	[e]
$NH_2 + C_2H_5NC \rightarrow NH_3 + CH_3CHNC$	2480	[e]
$NH_2 + CH_3CN \rightarrow NH_3 + H_2CCN$	2680	[e]
$NH_2 + CH_3NC \rightarrow NH_3 + H_2CNC$	2680	[e]
$O + HNC \rightarrow CO + NH$	1100	[e]
$O + HCN \rightarrow CO + NH$	1100	[b]
$OH + C_2H_5CN \rightarrow H_2O + C_2H_4CN$	1200	[e]
$OH + C_2H_5NC \rightarrow H_2O + C_2H_4NC$	1200	[e]
$OH + C_2H_5CN \rightarrow H_2O + CH_3CHCN$	1000	[e]

$OH + C_2H_5NC \rightarrow H_2O + CH_3CHNC$	1000	^{e}
$OH + CH_2CHCN \rightarrow H_2O + C_2H_2CN$	4000	^{e}
$OH + C_2H_3NC \rightarrow H_2O + C_2H_2NC$	4000	^{e}
$OH + CH_3CN \rightarrow H_2O + H_2CCN$	500	^{e}
$OH + CH_3NC \rightarrow H_2O + H_2NC$	500	^{e}
$CH_3CN(s) + H(s) \rightarrow CH_3CHN(s)$	4680	^{i}
$CH_3CHN(s) + H(s) \rightarrow CH_3CHNH(s)$	0	^{i}
$CH_3CHNH(s) + H(s) \rightarrow CH_3CHNH_2$	0	^{i}
$CH_3CHNH_2(s) + H(s) \rightarrow CH_3CH_2NH_2(s)$	0	^{i}
$CH_3NC + H \rightarrow CH_3NCH$	1912	^{i}
$CH_3NCH + H \rightarrow CH_3NCH_2$	0	^{i}
$CH_3NCH_2 + H \rightarrow CH_3NHCH_2$	0	^{i}
$CH_3NHCH_2 + H \rightarrow CH_3NHCH_3$	0	^{i}

[a] Tennis et al. (2023)

[b] From analogous cyanide reaction

[c] Method from Woon & Herbst (2009b)

[d] Anicich et al. (1994)

[e] Willis et al. (2020)

[f] Predicted products of photodestruction

[g] This work

[h] Method from Herbst & Osamura (2008)

*In reaction rate formulae: ζ is the H_2 cosmic-ray ionization rate; A_v is the visual extinction